DESIGN AND ANALYSIS OF MICROELECTROMECHANICAL RESONATORS WITH ULTRA-LOW DISSIPATION

A Dissertation
Presented to
The Academic Faculty

by

Logan D. Sorenson

In Partial Fulfillment
of the Requirements for the Degree
Doctor of Philosophy in the
School of Electrical and Computer Engineering

Georgia Institute of Technology
December 2013

Copyright © 2013 by Logan D. Sorenson

DESIGN AND ANALYSIS OF MICROELECTROMECHANICAL RESONATORS WITH ULTRA-LOW DISSIPATION

Approved by:

Farrokh Ayazi, Advisor
School of Electrical and Computer Engineering
Georgia Institute of Technology

Mark Allen
School of Electrical and Computer Engineering
Georgia Institute of Technology

Oliver Brand
School of Electrical and Computer Engineering
Georgia Institute of Technology

William Hunt
School of Electrical and Computer Engineering
Georgia Institute of Technology

Paul Kohl
School of Chemical and Biomolecular Engineering
Georgia Institute of Technology

Date Approved: July 29th, 2013

To my wife, Phuong,

for her everlasting love, patience, and understanding during the course of our academic endeavors…

our life-long adventure together is just beginning.

ACKNOWLEDGEMENTS

It was my great fortune upon landing at Georgia Tech that I came across Dr. Farrokh Ayazi's website. Having developed an interest in the nature of things at very small scales due in part to the buzz surrounding nanotechnology and coming from a VLSI background, I knew I wished to concentrate my Ph.D. studies on micro- and nanoscale physical devices, but not much more than that. Dr. Ayazi's website displayed some beautifully-crafted microelectromechanical devices which was enough to convince me to contact him to find out if he had any openings in his Integrated MEMS (IMEMS) lab. I am greatly thankful to have had Dr. Ayazi as an advisor and mentor over the past years, as his commitment toward advancing the state-of-the-art while demanding the highest quality work is unparalleled except for a select few in the field. I would like to thank him for sharing his guidance and vision with me, through which I have developed my own standards for carrying out my work with the utmost dedication and attention to detail.

I would like to thank my committee members, Dr. Mark Allen, Dr. Oliver Brand, Dr. Bill Hunt, and Dr. Paul Kohl, for their feedback and insights during the proposal and dissertation process, especially considering their extremely busy schedules. I thank Dr. Allen for laying the foundations of the MEMS community at Georgia Tech. I would especially like to thank Dr. Brand and Dr. Hunt for their extremely useful MEMS and Acoustics courses, which proved to be beneficial sources of the fundamentals needed to pursue research in this area. I thank Dr. Kohl for being a patron of the IMEMS group over the years resulting in many collaborations and for his willingness to always help out. I would like to thank the rest of the faculty and staff at Georgia Tech, many of whom I grew to know through my coursework or other activities, for their diligence and commitment to forging an excellent place to conduct advanced research. These include Dr. Thomas

Gaylord and Dr. Azad Naeemi, who were kind enough let me audit their classes merely because I had an interest in the subject. I am grateful to Dr. Thomas Brewer, Dr. William Marshall Leach, and the other ECE 3042 TAs for introducing me to the Georgia Tech ECE culture during my first semester here. Dr. Leach's untimely passing came as a shock to us all, and he will greatly be missed. I hope that his legacy at Georgia Tech will carry on for the generations to come. Thanks to Dr. David Anderson for showing what it is to be a successful family man and professor with amazing time management skills. I am also greatly thankful for the Institute for Electronics and Nanotechnology cleanroom staff, including Gary Spinner, Vinh Nguyen, Charlie Suh, Eric Woods, and many others, without whose patience and dedication much of this work would not even be possible. I also extend my thanks to our research sponsors and project partners over the years, especially Harmeet Bhugra and his team at Integrated Device Technology, Inc., Dave Rozelle, Doug Meyer, Dennis Bevan et al. at Northrop Grumman, and the good folks at Qualtré.

On the IMEMS side, I cannot express enough thanks and gratitude to my fellow and former labmates. You have become my extended family over the years. I would like to thank my predecessors, Dr. Siavash Pourkamali, Dr. Reza Abdolvand, Dr. Gavin K. Ho, who laid the foundations for a majority of the work on which my dissertation relies. I would like to thank Dr. Wanling Pan, Dr. Faisal Zaman, Dr. Mina Rais-Zadeh, Dr. Houri Johari, Dr. Hossein Miri-Lavassani, Varun Keesara, and Mark Zurcher for providing excellent examples of what it means to be a researcher in the IMEMS group. I am especially grateful for my contemporary labmates who were essential in supporting me during this long and often difficult experience. Thanks to Dr. Giorgio Casinovi for introducing me to the finite element analysis technique and being an amazing resource for mathematical modeling. Thanks to Dr. Mauricio Pardo, Dr. Milap Dalal, and Dr. Jenna Fu for the deep friendship, many late night dinners, conversations about research and life, and all around good experiences. Thanks also to Xin Gao, Roozbeh Tabrizian, Diego Serrano, Wang-Kyung Sung, Arashk N.-Shirazi, Yaesuk Jeong, and Peng Shao for the fruitful collaborations and

friendship. May you graduate soon. Thanks to our amazing admins over the years, who make the world go around: Nydia Akins, Janet Arnold, Angel Greenwood, Gay Burchfield, Lisa Gardner, Daphne Bronner, and Angelika Braig. Thanks to the new and future IMEM-Sians, especially Dr. Vahid Tavassoli, for continuing the tradition of producing top-quality research and building upon our group's reputation in the field.

I would like to thank my family and friends, especially those here at Georgia Tech in Dr. Anderson, Dr. Brand, Dr. Howard, Dr. Hasler, Dr. Cressler, and Dr. Ghovanloo's groups who made my time especially enjoyable and engaged in many discussions to provide balance to my research, and those in other places who had to endure my long absence while remaining true friends. I am grateful for my family members' support: my dearly-departed grandparents, my aunts and uncles and cousins, my brothers Jens and Owen, my sister-in-law Rain and my three beautiful and lively nieces Zoe, Elle, and Sophia, my wife's family, especially her parents Huong and Cuong and her brother Bao, and my mother and father, Joanne and Olaf, whose guidance and wisdom kept me firmly grounded in maintaining progress toward my goals. Finally, I am dearly indebted to my lovely wife, Phuong, for the patience, strength, and grace she has shown during the course of our Ph.D. work, for though we faced involuntary physical separation with her at Virginia Tech and myself at Georgia Tech, we never lost faith in each other and worked toward the goal of beginning our lives together. All my efforts are for you.

TABLE OF CONTENTS

LIST OF TABLES

LIST OF FIGURES

LIST OF SYMBOLS OR ABBREVIATIONS

3D	Three-Dimensional.
α	Linear Coefficient of Thermal Expansion (CTE) $[1/K, 1/^{\circ}C]$.
α_{ij}	CTE (Tensor Form) $[1/K, 1/^{\circ}C]$.
BAW	Bulk Acoustic Wave.
BW	Bandwidth.
BZ	Brillouin Zone.
c_{IJ}	Stiffness Tensor in Voigt Notation $[Pa, N/m^2]$.
c_{ijkl}	Stiffness Tensor $[Pa, N/m^2]$.
C_{P}	Specific Heat Capacity at Constant Pressure (Mass Form) $[J/kg \cdot K]$.
CR-LAB	Coupled-Ring Linear Acoustic Bandgap.
D	Damping Constant $[N \cdot s/m]$.
D_{eff}	Effective Damping Constant $[N \cdot s/m]$.
Δ_E	Relaxation Strength of Young's Modulus [1].
Δf, $\Delta f_{\text{-3dB}}$	Bandwidth, -3dB Bandwidth (typical).
DOF	Degree of Freedom.
DRIE	Deep Reactive Ion Etch.
d_{th}	Thermal Path (TED) $[m]$.
E	Young's Modulus $[Pa, N/m^2]$.
ϵ_{ij}	ij^{th} Component of Strain $[m]$.
$E_{\mathrm{sys.}}$	Total Energy of the System $[J]$.
$\dot{E}_{\mathrm{sys.}}$	Rate of Change of System Energy $[W, J/s]$.
η	η Surface Parameter $[m]$.
η_{ijkl}	Viscosity Tensor $[Pa \cdot s, N \cdot s/m^2]$.
f	Frequency $[Hz, 1/s]$.
FBAR	Film Bulk Acoustic Resonator.

F_{body}	Body Force $[N/m^3]$.
FE	Finite Element.
F_n	Noise Force $[N]$.
$\bar{F}_n^2$	Mean-Square Noise Force $[N^2/Hz]$.
FWHM	Full Width Half Maximum Bandwidth.
GPS	Global Positioning System.
HARPSS$^{\text{TM}}$	High Aspect Ratio combined Poly- and Single-crystal Silicon.
IC	Integrated Circuit.
IL	Insertion Loss.
IMEMS	Georgia Tech Integrated MEMS Group.
J_{a}	Acoustic Flux $[W/m^2, J/s \cdot m^2]$.
$\dot{J}_{\text{a}}$	Change of Acoustic Flux per Second $[W/s \cdot m^2, J/s^2 \cdot m^2]$.
K	Lumped Spring Constant $[N/m]$.
κ	Thermal Conductivity $[W/K \cdot m]$.
κ_{ij}	Thermal Conductivity (Tensor Form) $[W/K \cdot m]$.
K_{bulk}	Bulk Modulus $[N/m^2]$.
$K_{\text{an.}}$	Anisotropic Bulk Modulus $[N/m^2]$.
K_{eff}	Effective Spring Constant $[N/m]$.
LAB	Linear Acoustic Bandgap.
λ	Wavelength $[m]$.
λ_a	Acoustic Wavelength $[m]$.
m	Mode Index.
M	Lumped Mass $[kg]$.
M_{eff}	Effective Mass Constant $[kg]$.
MEMS	Microelectromechanical Systems.
μHSR	Micro-Hemispherical Shell Resonator.
μm	Micrometer, micron [1E-6 m].

NEMS	Nanoelectromechanical Systems.
nm	Nanometer [1E-9 m].
ν	Poisson's Ratio [1].
ω	Angular Frequency $[rad/s]$.
PC	Phononic Crystal.
φ	Polar Angle in Spherical Coordinates $[rad, ^\circ]$.
PML	Perfectly-Matched Layer.
Q	Quality Factor [1].
Q_e	Electrical Quality Factor [1].
Q_m	Mechanical Quality Factor [1].
r	Radial Coordinate in Spherical Coordinates $[m]$.
RFID	Radio Frequency Identification.
ρ	Mass Density $[kg/m^3]$.
SAW	Surface Acoustic Wave.
SCS	Single-Crystalline Silicon.
SEM	Scanning Electron Microscope.
SiBAR	Silicon Bulk Acoustic Wave Resonator.
σ_{ij}	ij^{th} Component of Stress $[m]$.
SNR	Signal-to-Noise Ratio $[dB]$.
SOI	Silicon-on-Insulator.
τ	Free-Oscillation Decay Time Constant $[s]$.
τ_{th}	Thermal Relaxation Time Constant (TED) $[s]$.
TED	Thermoelastic Dissipation.
T	Temperature (Absolute or Relative) $[K, ^\circ C]$.
T_0	Absolute Reference Temperature $[K, ^\circ C]$.
θ	Azimuthal Angle in Spherical Coordinates $[rad, ^\circ]$.
T_i	Surface Traction in the i^{th} Direction $[N/m^2]$.

t	Time $[s]$.
TPoS	Thin-film Piezoelectric-on-Silicon.
u	Displacement Field Component $[m]$.
u_i	Displacement in the i^{th} Direction $[m]$.
$u_{\max}$	Spatial Maximum of Displacement Field Norm $[m]$.
v	Displacement Field Component $[m]$.
v_a	Acoustic Velocity $[m/s]$.
v_i	Partical Velocity in the i^{th} Direction $[m/s]$.
w	Displacement Field Component $[m]$.
x	'x' Coordinate in Cartesian Coordinates $[m]$.
ξ	ξ Surface Parameter $[m]$.
y	'y' Coordinate in Cartesian Coordinates $[m]$.
z	'z' Coordinate in Cartesian Coordinates, Radial Offset Coordinate in Spherical Coordinates $[m]$.

SUMMARY

This dissertation investigates dissipation in microelectromechanical (MEMS) resonators via detailed analysis and modeling of the energy loss mechanisms and provides a framework toward creating resonant devices with ultra-low dissipation. Fundamental mechanisms underlying acoustic energy loss are explored, the results of which are applied to understanding the losses in resonant MEMS devices. Losses in the materials, which set the ultimate limits of the achievable quality factor of the devices, are examined. Other sources of loss, which are determined by the design of the resonator, are investigated and applied to example resonant MEMS structures. The most critical of these designable loss mechanisms are thermoelastic dissipation (TED) and support (or anchor) loss of acoustic energy through the attachment of the MEMS device to its external environment. The dissipation estimation framework enables prediction of the quality factor of a MEMS resonator, which were accurate within a factor of close to 2 for high-frequency bulk acoustic wave MEMS resonators, and represents a signficant step forward by closing one of the largest outstanding problems in MEMS devices: how to predict the quality factor for a given device.

Dissipation mitigation approaches developed herein address the most critical dominant loss mechanisms identified using the framework outlined above. These approaches include design of 1D phononic crystals (PCs) and novel 3D MEMS structures to trap and isolate vibration energy away from the resonator anchors, optimization of resonator geometry to suppress thermoelastic dissipation, and analysis of required levels of surface polish to reduce surface dissipation. Phononic crystals can be used to manipulate the properties of materials. In the case of the 1D PC linear acoustic bandgap (LAB) structures developed here, this manipulation arises from the formation of frequency stop bands, or bandgaps,

which convert silicon from a material capable of supporting acoustic waves to a material which rejects acoustic propagation at frequencies in the bandgap. The careful design of these LAB structures is demonstrated to be able to enhance the quality factor and insertion loss of MEMS resonators without significant detrimental effects on the overall device performance.

CHAPTER I

INTRODUCTION

Electron waves, due to their nature as collections of nearly-free particles, suffer from energy loss at a far greater rate than their acoustic equivalents. This is because electrons in a gas-like state are bound to scatter with greater frequency due to the long-distance interaction of charged particles and quickly reach thermal equilibrium, whereas phonons (acoustic quasi-particles), a large number of which in synchronous make up an *acoustic wave*, can easily slip by each other. This simple physical fact has motivated the development of acoustic wave technologies, in which the high *quality factor* (or Q, a measure of energy dissipation) of an acoustic device is exploited to enhance performance of combined electromechanical systems. Advances in micromachining technology over the past few decades have taken great strides in miniaturizing such devices and systems, for which combined fabrication of integrated transducers, usually capacitive or piezoelectric, is now commonplace. This has led to the Microelectromechanical Systems (MEMS) and the emerging Nanoelectromechanical Systems (NEMS) fields. Meanwhile, transistors, resistors, capacitors, and even inductors (to some extent) have long succumbed to the quest for integration on chip that has driven the semiconductor industry for the past half-century. However, several necessary components for most modern systems have eluded integration so far: low-jitter oscillators and high-rejection filters. In addition, miniaturized sensors, which act as the gateway for information exchange between the physical and digital worlds, are in ever-increasing demand because of the growing importance of real-time environmental monitoring for applications including personal health, food safety, navigation, and many others.

High-performance oscillators are traditionally made from quartz crystals. Quartz is exceptionally resistant to frequency drift, as long as its temperature and dimensions are

held constant. This is usually achieved by sealing a large quartz crystal inside a metal can and actively heating it to maintain a constant temperature. Unfortunately, this technique is not compatible with modern semiconductor manufacturing, relegating the crystal oscillator to an external package from the rest of the circuitry it is associated with. The wiring connecting the oscillator to its companion integrated circuit (IC) contributes significant performance losses and sensitivity to interference, and maintaining the oscillator crystal at a stable temperature draws high power. Similar arguments can be made against surface acoustic wave (SAW) devices, which make up the bulk of state-of-the-art bandpass filters. Fortunately, MEMS techniques for constructing oscillators, filters, and sensors, utilizing fabrication methods developed for semiconductor manufacturing, are emerging, which may soon enable them to join their fellow components in sharing a single chip or package.

The scope of this research is to study energy dissipation and mitigation in tunable MEMS-based resonators (henceforth, MEMS resonators), which can be used to set the frequency in oscillator designs, serve as the frequency selective component in filters, and act as high-performance resonant sensors. MEMS resonators have been shown to consume small powers, allowing them to be used in low-power portable devices. Furthermore, these resonators can be integrated on a single die along with the other circuitry of the device during manufacturing. Multiple frequencies on a single chip are possible by using designs for which the dominant frequency-setting dimension is defined lithographically. If MEMS resonators can match the performance of traditional quartz and SAW components, there are opportunities for disruptive impact in many low-power applications, from mobile phones to wireless internet to handheld GPS units to Radio Frequency Identification (RFID) tags to wireless sensor networks. In particular, energy dissipation mechanisms and their impact on resonator quality factor, mitigation approaches, and tuning, trimming, and compensation mechanisms for MEMS resonators and resonant sensors are areas of outstanding concern for state-of-the-art research.

1.1 Origin and History of the Problem

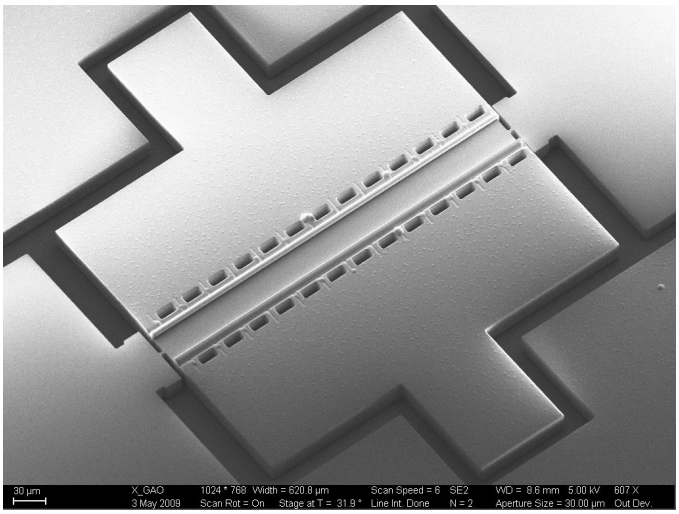

Figure 1: SEM view of a 100 MHz SiBAR developed at Georgia Tech [70].

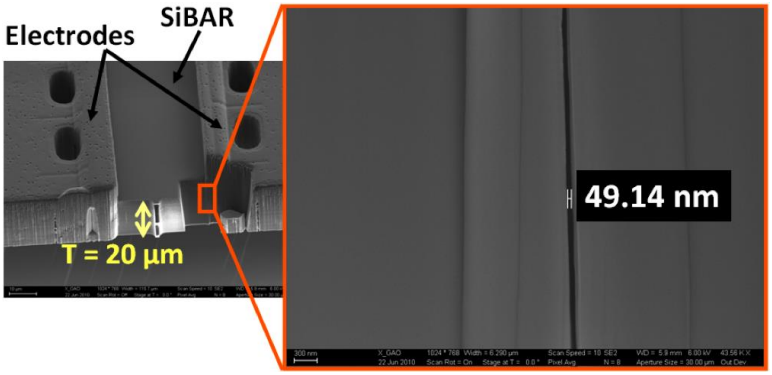

Figure 2: SEM view of a 50 nm capacitive gap of a 100 MHz SiBAR [71].

This work originates with the study of sound waves, such as those conducted by Lord Rayleigh and others in the late 1800s. Ultimately, the physics of sound waves can be considered to be a generalization of Newton's laws of motion to distributed matter. Investigation in the field of acoustics was spurred on by the development of crystalline and condensed matter physics in the early 1900s and continues to today. Fundamental works concerning the energy dissipation of acoustic waves in perfect crystals were contributed by Akhieser [6], Landau and Rumer [43], as well as Zener [97] in the 1930s. The first two studies concentrated on dissipation through phonon-phonon interactions in solids, while

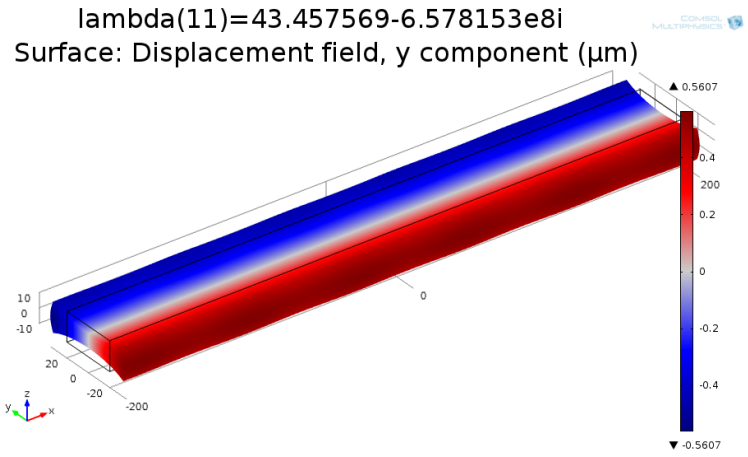

Figure 3: Mode shape of 100 MHz SiBAR (support tethers removed) showing displacement in the transverse width direction which sets the frequency of resonance.

the latter study by Zener gave the foundation for study of thermoelastic dissipation (TED), which is similar in many aspects to the Akhieser-type dissipation. The consequences of Landau and Rumer's work were relatively unknown in the MEMS community until recently [87], since it is relevant to frequencies in the gigahertz range.

In the mid-1900s and onward, much attention became focused on the anharmonic properties of crystals, as these properties account for the dissipation in the material through which the acoustic wave propagates. Some of this work was experimental, such as McSkimin's work with silicon and other materials [50, 51]. Other work focused on theoretical aspects, such as lattice dynamics [18, 57, 58, 78, 101]. In these studies, dissipation mechanisms such as phonon-electron interaction and scattering due to defects and surface roughness began to be considered.

It was around this time that the discovery of curious temperature behavior in quartz crystals led to great interest in piezoelectrically-actuated oscillators [19, 88]. Since an oscillator is essentially a "time sensor", counting the number of oscillations in a certain period will give an estimate of the time elapsed. However, if the oscillator becomes irregular in its cycles, i.e., the frequency of oscillation drifts, this time estimate will become inaccurate. Due to the nature of the interatomic potentials binding a solid crystal together, an increase in temperature will generally lead to an expansion of the crystal lattice, which necessarily

leads to a change in the macroscopic stiffness described through the modulus of elasticity of the material. Typically, the sign of this change results in the material becoming softer with an increase in temperature, causing the oscillator to run slower than nominal. If this occurs, the oscillator will cause fewer counts in a given period, causing that time period to be measured shorter in duration than it is in reality. However, in certain crystal cuts of quartz, the sign of the elastic modulus change is positive with temperature. Then the thermal expansion of the crystal is offset by an increase in the effective elastic modulus, such that the round-trip times (i.e., the oscillator period) of the acoustic waves remain constant. This temperature stability is highly-desired feature of oscillator systems, and has led to quartz's domination of the oscillator market. Only recently are technologies emerging which can compete with quartz in these areas.

The most popular competing acoustic technologies are Surface Acoustic Wave (SAW) devices [41, 94] and (thin) Film Bulk Acoustic Resonators (FBARs) [39, 68]. FBARs and SAWs have been the devices of choice for gigahertz filter applications in modern telecommunications systems due to their high coupling coefficients. Because of the thin film thicknesses used in these devices (on the order of microns), FBARs can be considered as a type of MEMS device. However, a drawback associated with FBARs is the large area required for efficient coupling. Also, they are difficult to compensate for process and temperature variations.

In the early 2000s, the Georgia Tech Integrated MEMS (IMEMS) group became interested in silicon-based bulk acoustic wave (BAW) resonators with true MEMS-scale dimensions. Initially, single-crystalline silicon (SCS) resonators were developed, taking advantage of the efficiency of nanogap transduction with the High Aspect Ratio combined Poly- and Single-crystal Silicon (HARPSS^{TM}) process [8, 63]. These became known as SiBARs (Figures 1, 2, and 3), short for Silicon Bulk Acoustic wave Resonators [64]. While these devices showed promise of low energy dissipation via high quality factors, their insertion loss (an important quantity which determines the amount of gain needed from an amplifier

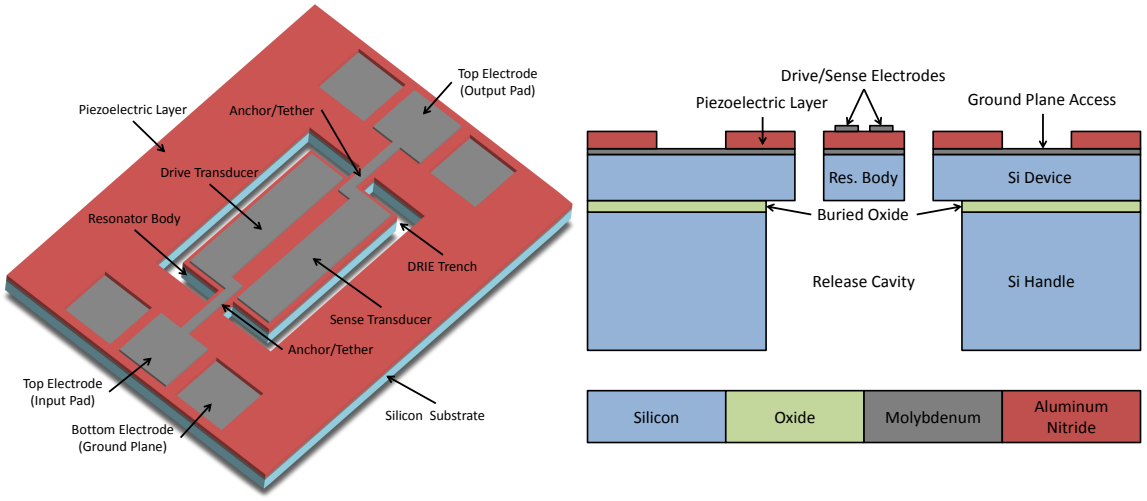

Figure 4: Thin-film Piezoelectric-on-Substrate (TPoS) resonator schematic (left) and cross-section (right). The TPoS technology was developed at Georgia Tech, and is now being commercialized by Integrated Device Technology (IDT), Inc.

to sustain the oscillations) suffered from the requirement of high polarization voltages to attain efficient capacitive transduction. As a solution to this issue, high-coupling piezoelectric thin films were deposited on the surface of the SiBARs, creating the Thin-film Piezoelectric-on-Silicon (TPoS) technology, shown in Figures 4 and 5 [32, 35]. Using a high-quality piezoelectric layer allowed improved insertion loss (IL) at the expense of some quality factor, although this trade-off can be somewhat mitigated by carefully setting the relative thicknesses of the silicon and piezoelectric layers. The SiBAR and TPoS technologies form the foundations of a large portion of the present work, in which it is sought to evaluate energy dissipation trade-offs to attain high performance without sacrificing the quality factor of the device.

Recently, the IMEMS group has developed 3D micro-Hemispherical Shell Resonators (μHSRs) which are intended to be highly-axisymmetric and low-dissipation resonators for gyroscope and other low-frequency sensor applications (Figure 6). These devices represent a voyage into unknown territories in terms of their dissipation mechanisms and, combined

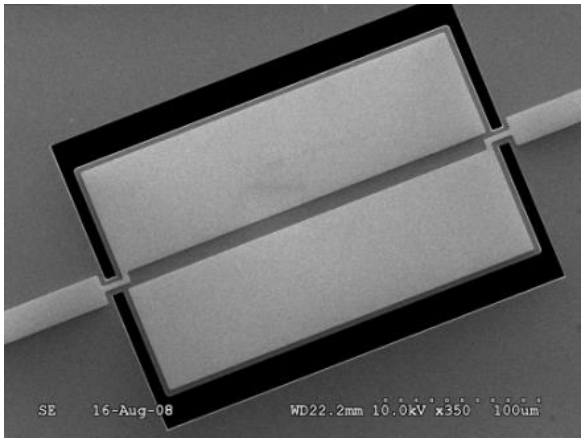

Figure 5: SEM view of TPoS resonator. Light gray regions are molybdenum (Mo) electrodes. Medium gray is the aluminum nitride (AlN) layer. The black areas are the trenches cut by silicon DRIE Bosch process.

with high-frequency SiBAR and TPoS technologies, form an ideal test bed for the Q analysis framework developed herein.

1.2 Distributed Equations of Motion and Reduction to Second-Order System

The underpinnings of this work rely on understanding the distributed vibration patterns of a MEMS resonator (i.e., the vibration mode shape). By treating the particles of the resonator as a continuous field of displacements, one may describe the position of any particular particle at any given instant of time of the resonator body in terms of the sum of its position vector at rest and a displacement vector from its rest position. Pure translation and rotation can be ignored in most cases (with appropriate consideration for accelerometers and gyroscopes), meaning only the pure deformations of the resonator are of interest. Hence, the vibration of the resonator can be described in its most general form by the distributed equation of motion [42]

$$\rho \frac{\partial^2 u_i}{\partial t^2} - \frac{\partial \sigma_{ij}}{\partial x_j} = F_{\text{body}}. \tag{1}$$

in which t represents time, x_j is the coordinate in the j^{th} direction, u_i is the i^{th} component of displacement, σ_{ij} is the ij^{th} component of the stress tensor, ρ is the mass density of the

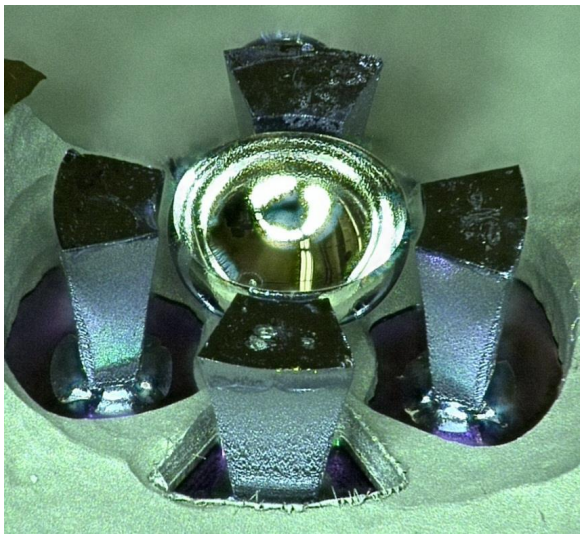

Figure 6: Optical micrograph of a platinum-coated oxide micro-hemispherical shell resonator (μHSR) studied in this work.

material, and F_{body} represents forces which occur internally to the body such as gravity or thermal stresses due to non-constant temperature over the resonator. Considering the viscosity of the material and dissipation that effectively manifests itself as viscous-like damping, the above equation can be augmented to

$$\rho \frac{\partial^2 u_i}{\partial t^2} - \frac{\partial}{\partial x_j}\left(c_{ijkl}\epsilon_{kl} + \eta_{ijkl}\frac{\partial \epsilon_{kl}}{\partial t}\right) = F_{\text{body}}, \tag{2}$$

where the constitutive relation between stress and strain tensors $\sigma_{ij} = c_{ijkl}\epsilon_{kl}$ has been used, with c_{ijkl} as the material stiffness tensor and η_{ijkl} representing the viscosity tensor which accounts for resistance to linear changes of the strain with time. Viscous damping originates with the flow of atoms inside the material due to the tendency to move away from higher concentrations via diffusion, and hence is more significant in amorphous materials such as silicon dioxide, where the disorder in the material results in non-optimal flow and needs to relax to the final state, rather than in crystalline materials such as silicon where all atoms in a crystal plane can move essentially simultaneously (in a perfect crystal). In addition to the distribution of the body forces acting on the device, there are additional forces which are imposed by the boundary conditions (e.g., mechanical or electrostatic surface

tractions). Once the above equation of motion is solved for the distributed vibration pattern of the resonator (typically using numerical methods for complicated geometry, although analytical solutions may exist in special cases), one may reduce the particular mode to a second-order system where typically the spatial maximum amplitude (u_{max}) is used as the amplitude for convenience. Then one may define an effective modal stiffness, mass, and damping factor for that mode of the device. These parameters will satisfy the second-order differential equation

$$M_{\text{eff}}\frac{\partial^2 u_{\text{max}}}{\partial t^2} + D_{\text{eff}}\frac{\partial u_{\text{max}}}{\partial t} + K_{\text{eff}}u_{\text{max}} = F_{\text{external}} \tag{3}$$

In the above, the effective modal damping coefficient can be written in terms of Q as $D_{\text{eff}} = M_{\text{eff}}\omega_n/Q = K_{\text{eff}}/\omega_n Q$. The effective modal mass and stiffness are relatively straightforward to obtain and predominantly depend on the geometry and material of the device. However, the damping coefficient can be quite complicated to model accurately, as will become apparent throughout this dissertation. A main thesis of this work is that by developing deep understanding of the appropriate distributed dissipative terms for the given vibration mode, one may derive accurate bounds for the damping coefficient, or alternatively, the Q of the resonator. The insights required to do this will be discussed in much more detail in the following chapters.

1.3 The Meaning of Low Dissipation in MEMS Resonators

In (3), the distributed vibration mode of a MEMS resonator is represented in terms of a lumped-element equivalent spring-mass system. If D_{eff} is zero, the system is lossless, and the energy of the system oscillates perfectly between its kinetic and potential forms (i.e., the maximum displacement and velocity are 90° out-of-phase). When D_{eff} becomes non-zero (as in essentially any real-world system), the phase relationship between the displacement and velocity is perturbed, resulting in a net force on the system which removes mechanical energy from the oscillator. Eventually, if the dissipative system is left to oscillate freely,

the amplitude of the oscillation will decay to zero, leaving the system in its rest state. In the simplest case, the spring-mass system would be brought to rest by an external force which is out of phase with the displacement and opposite in direction to the velocity, much like how a child's swing can be gently stopped by applying small pushes when they are near to the ground, whereas applying the same push at the apex of their swing causes them to gain more energy and continue swinging. Alternatively, the dissipative forces can arise internally, by means of internal friction. There are three main types of internal friction important to MEMS resonators: those arising due to viscosity of the material from disorder of the atomic arrangement, those arising due to fundamental phonon and electron interaction processes, and those arising due to solid heat conduction because of perturbations to the temperature distribution of the resonator from the acoustic standing waves. Hence, a low dissipation MEMS resonator experiences small internal friction and is designed to minimize the influence of external forces which are out-of-phase with the acoustic resonance.

Dissipation influences many aspects of the performance of a resonant MEMS device. Table 1 lists some of the parameters influenced by the Q factor, which represents the inverse of energy dissipation. In most cases, with the notable exception of static MEMS devices such as accelerometers or microphones, a high Q is desired to enhance the performance. For sensor applications, a higher Q can result in greater sensitivity and improved signal-to-noise ratio (SNR). Gyroscopes are tricky beasts, in that they work best when they are mode-matched, meaning the center frequencies of the two spatially-orthogonal modes are matched within their bandwidth. However, if the Q increases, the bandwidth of each resonance mode is decreased, and tighter control is needed to maintain the mode-matched condition. Hence, Q control is absolutely essential in the case of a gyroscope.

1.4 Organization of the Dissertation

The remainder of this dissertation proceeds first with a discussion of energy dissipation and its relation to quality factor in MEMS resonators in Chapter 2. The same chapter reviews

Table 1: MEMS Device Performance Parameters Influenced by Q.

Parameter	Relation to Q
Damped Resonator Center Frequency	$f_c = f_n \sqrt{1 - \frac{1}{4Q^2}}$
Resonator Peak to Off-Resonance Amplitude	Q
Slope of Phase-Frequency Response at f_n	$-4\pi Q$
Resonator Bandwidth (BW)	$\mathrm{BW}_{3\mathrm{dB}} = \Delta f_{3\mathrm{dB}} = f_n/Q$
Resonator Motional Impedance	$R_m = \frac{K_{\mathrm{eff}}}{\omega_n Q \eta^2}$
Resonator Insertion Loss (IL)	$\mathrm{IL} = 20 \log \left(\mathrm{abs} \left(\frac{2Z_0 + R_{\mathrm{series}}}{R_m + 2Z_0 + R_{\mathrm{series}}} \right) \right)$
Free-Oscillation Decay Time (τ)	$\tau = \frac{2Q}{\omega_n}$
Filter Roll-off (Low-pass Filter)	Q/f_n
Oscillator Phase Noise (Leeson's effect)/Jitter	$L(\omega) = \frac{1}{2} S_{\substack{\mathrm{flicker} \\ +\mathrm{white}}}(\omega) \left[1 + \left(\frac{1}{2Q_L} \right)^2 \left(\frac{\omega_n}{\omega} \right)^2 \right]$
Mechanical Noise in 1 Hz BW On-Resonance	$\bar{u}^2_{\mathrm{max}}\vert_{\omega \to \omega_n} = 4k_B T Q / \omega_n K_{\mathrm{eff}}$
Mechanical Noise in 1 Hz BW Off-Resonance	$\bar{u}^2_{\mathrm{max}}\vert_{\omega \to \omega_n} = 4k_B T / \omega_n K_{\mathrm{eff}} Q$

important energy dissipation mechanisms in detail to develop a platform for analysis and prediction of Q. Next, these principles are applied to study dissipation in SiBAR and TPoS resonators in Chapter 3. Then Chapter 4 introduces Linear Acoustic Bandgap (LAB) structures and they are demonstrated to improve the performance of SiBAR and TPoS resonators by removing the support loss component of Q. 3D micro-Hemispherical Shell Resonators (μHSRs) are introduced in Chapter 5 and the important dissipation mechanisms are examined in the framework presented here. Due to the low stiffness of these structures, surface loss is expected to dominate and a supporting model is developed based on thermoelastic dissipation introduced by surface roughness, allowing estimation of the required surface smoothness to achieve the targeted Q value. The support loss and bulk modal TED is also examined for these resonators. Finally, the dissertation is brought to a close in Chapter 6 by reviewing the contributions of this work to the field of resonant MEMS devices and making suggestions to improve upon these models and account for energy dissipation arising due to other sources.

CHAPTER II

QUALITY FACTOR IN MEMS RESONATORS

As can be inferred from the previous chapter, perhaps the most important measure of energy dissipation in resonant acoustic devices is quality factor, or Q. This chapter[1] examines several of the most important energy dissipation mechanisms in MEMS resonators and how to relate them to the final Q of the device in a particular vibration mode of interest. However, since there are a large number of ways to dissipate energy, not all possible dissipation mechanisms which may be relevant to a particular MEMS device can be included. Also, many energy dissipation mechanisms require detailed and extensive analysis, such as those which depend on the microstructure of the materials comprising the MEMS device and require experimental knowledge which may not be available or depend on processing conditions such as defect, dislocation, and doping concentrations. Instead, it is hoped that the framework of studying energy dissipation developed here can be extended and adapted to situations of interest as the need arises. Hence, this chapter starts with intrinsic dissipation mechanisms which are inherent to the materials which compose the MEMS resonator, as these can be considered to apply to a wide variety of MEMS devices. After this, common extrinsic dissipation mechanisms are discussed, such as support loss relating to leakage of acoustic energy through the attachment of the MEMS resonator to its package and bulk modal thermoelastic dissipation (TED) arising from the standing acoustic wave pattern of the vibration mode.

[1] Portions of this chapter on quality factor are adapted from work which has gone into a conference publication [9]. They have been updated and revised to fit the context of this dissertation.

2.1 Relationship Between Energy Dissipation and Q

The most general definition of Q relates to the inverse of the fractional dissipation of energy in the system per second. That is,

$$Q = 2\pi f \left| \frac{E_{\text{sys.}}}{\dot{E}_{\text{sys.}}} \right|, \tag{4}$$

where f is the steady-state operating frequency, $E_{\text{sys.}}$ is the energy contained in the MEMS resonator (the sum of its kinetic and potential energies for a mechanical resonance), and $\dot{E}_{\text{sys.}}$ is the time derivative of the energy contained in the MEMS resonator if it were left in free-oscillation (i.e., $\dot{E}_{\text{sys.}}$ is the energy dissipation per second and is the amount of power a sustaining amplifier would have to provide to maintain a constant amplitude if the MEMS resonator were configured as an oscillator). This dissertation considers only passive MEMS resonators; since the change of energy of the MEMS resonator with time is always negative (or zero in special cases) for a passive device, the denominator of (4) is negative, but Q is a positive quantity and absolute value signs are needed. The free-oscillation ring-down decay time constant τ (how long it takes for the energy of oscillations to reach a factor of $e^{-2\pi}$ of their original value) is closely related to this definition and can be determined as

$$\tau = 2Q/\omega. \tag{5}$$

The physical intuition underlying τ is that a constant fraction of the energy is dissipated from the system per cycle of oscillation, resulting in exponential decay. A commonly-used alternative approximation of Q for low-dissipation devices relates the resonance frequency of a MEMS resonator to its FWHM or -3 dB bandwidth

$$Q = f_n/\Delta f_{\text{-3dB}}, \tag{6}$$

which is sometimes called the peak sharpness [46]. These two definitions indicate that high Q enables resonant devices to produce *high spectral purity* oscillations with a *long decay*

time. With few exceptions, higher Q enables performance improvements in many resonant MEMS devices. In other words, resonant MEMS devices are designed specifically to take advantage of the high Qs offered by acoustic or mechanical vibration.

2.2 The Main Types of Energy Dissipation in MEMS Resonators

A large body of research has explored different dissipation mechanisms in flexural and SAW devices; however, since high-frequency MEMS BAW resonators have only been realized due to recent advances in micromachining techniques (i.e., fabrication of sub-nanometer capacitive gaps, deposition of high quality piezoelectric thin films, etc.), dissipation mechanisms in micromachined BAW devices remain open to advanced study. In addition, 3D shell-type MEMS resonators have been attracting interest lately and present a different set of challenges in understanding their dissipation mechanisms, mostly as a consequence of the very thin shell layers which create unprecedentedly-high dependence on the surface loss mechanisms. These two extremes of high-frequency BAW and low-frequency shell devices form ideal test cases for a general platform for investigation of Q in MEMS resonators and design of devices with the lowest possible dissipation.

For an ideal, lossless resonant device, the Q should be infinite according to (4). However, in reality, several dissipation mechanisms limit the Q of resonant devices. These can be classified into *intrinsic* and *extrinsic* dissipation mechanisms. Intrinsic mechanisms are those which pertain to fundamental loss processes occurring in the material of a resonator. In other words, their contribution to Q can be determined by assuming the propagation of the acoustic wave in a solid body of the same material as the MEMS resonator with infinite extent. These are bulk acoustic waves (BAW), which may have longitudinal or transverse (shear) polarization of the particle displacements relative to the direction of acoustic propagation (or quasi-longitudinal and quasi-shear in the general case of anisotropic crystals). Examples of intrinsic energy dissipation are interaction of the acoustic wave with the thermal lattice vibrations (thermal phonons) or mobile charge carriers (in the form of electrons

or holes). On the other hand, extrinsic dissipation mechanisms result from non-idealities in design, such as finite dimensions of supports (i.e., support loss), air damping, and surface dissipation mechanisms. In between the intrinsic and extrinsic dissipation mechanisms, some dissipation mechanisms can be termed "quasi-intrinsic", meaning that they can be calculated in the infinite extent BAW model, but their contributions depend on how the material was fabricated and its quality in terms of purity, defects, dislocations, voids, etc. A key distinguishing feature of extrinsic and quasi-intrinsic dissipation mechanisms is that they can theoretically be eliminated, meaning they do not impose an upper limit on the achievable Q. Hence, a perfect, crystalline material will exhibit only fully-intrinsic dissipation mechanisms (which may be termed fundamental dissipation mechanisms), but this is an approximation to reality in most cases. The inverse relationship between energy dissipation and Q as defined in (4) leads to (7), which represents the overall device Q as the summation of individual Q factors due to various dissipation mechanisms:

$$Q = \left[\sum_i \frac{1}{Q_i} \right]^{-1}, \tag{7}$$

where Q_i represents the contribution of a particular dissipation mechanism. Studying (7), reduced damping by dissipation mechanism i translates to increased Q_i, and therefore an improvement in the overall Q. Further, if one (or a few) particular Q_i is much lower than the rest of the Q_i, the final Q will be close to the lowest Q_i. This loss mechanism can then be said to be the *dominant* loss mechanism in the device. Table 2 summarizes the major individual dissipation mechanisms present in resonant MEMS devices.

2.3 Intrinsic Dissipation Mechanisms

Intrinsic dissipation mechanisms for ideal, defect-free crystalline materials include phonon-phonon interactions, phonon-electron interactions, and acoustic thermoelastic dissipation (TED). In this section, the resonator is considered as an acoustic waveguide with an infinite

Table 2: Major dissipation mechanisms in MEMS devices and classification by material intrinsicality.

Dissipation Mechanism (Q_i)	Material Intrinsicality
Phonon-Phonon Interaction (Q_{PhPh})	Intrinsic
Phonon-Electron Interaction (Q_{PhEl})	Intrinsic
Acoustic Thermoelastic Dissipation (Q_{TED})	Intrinsic
Microscale and Intergranular TED	Quasi-Intrinsic
Impurity/Defect/Dislocation/Isotope/Vacancy Scattering	Quasi-Intrinsic
Grain Boundary Scattering	Quasi-Intrinsic
Loss from Copropagating EM Waves (Piezoelectric and Magnetic Materials)	Quasi-Intrinsic
Bulk Modal Thermoelastic Dissipation (Q_{BulkTED})	Extrinsic
Support Loss (Q_{Support})	Extrinsic
Air/Fluid Damping (Q_{Air})	Extrinsic
Surface and Interfacial Loss (Q_{Surface})	Extrinsic
Surface Thermoelastic Dissipation (Q_{SurfTED})	Extrinsic
Coupling into other Acoustic Modes (Surface Reflection)	Extrinsic
Dielectric Loss ($Q_{\mathrm{Diel.}}$)	Extrinsic
Electrical Loading/Resistive Losses ($Q_{\mathrm{Elec.}}$)	Extrinsic

dimensions. The acoustic absorption coefficient $\alpha(\omega)$ is defined as [42, 87]

$$\alpha(\omega) = \frac{1}{2}\left|\frac{\dot{\bar{J}}_{\mathrm{a}}}{\bar{J}_{\mathrm{a}}}\right|, \tag{8}$$

where $\bar{J}_{\mathrm{a}}$ is the mean acoustic flux over an acoustic wavelength and $\dot{\bar{J}}_{\mathrm{a}}$ is the change of the mean acoustic flux with time. Again, absolute values are needed to account for the sign of $\dot{\bar{J}}_{\mathrm{a}}$. Thus, $\alpha(\omega)$ describes the variation in wave amplitude with distance. Therefore, by definition, Q and $\alpha(\omega)$ are related by

$$Q = \frac{\omega}{2\alpha(\omega)v_a}, \tag{9}$$

where v_a is the acoustic wave velocity and ω is the angular frequency. Table 3 presents generalized intrinsic dissipation mechanisms and indicates their frequency dependency of α, as well as the resulting dependency for Q by (9). The first type is generally not of concern for MEMS devices operated at small amplitudes and will not be discussed further

in the context of this work. The importance of this table is that it allows identification of different mechanisms of dissipation experimentally by examining their behavior over a range of frequencies.

Table 3: Frequency dependence of general intrinsic dissipation types compiled from [37].

Dissipation Type	$\alpha(\omega)$	$Q(\omega)$
Macroscopic plastic flow	α = const.	$Q \propto \omega$
Hysteresis	$\alpha \propto \omega$	Q = const.
Viscous dissipation (relaxation)	$\alpha \propto \omega^2$	$Q \propto 1/\omega$
Scattering	$\alpha \propto \omega^4$	$Q \propto 1/\omega^3$

2.3.1 Dissipation from Interaction of Acoustic Phonons with Thermal Phonons (Q_{PhPh})

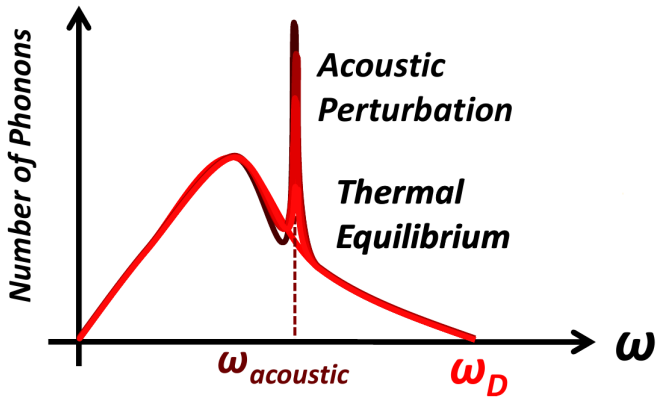

Figure 7: Schematic diagram of relaxation of an undriven acoustic wave to thermal equilibrium via interaction with thermal phonons. The acoustic wave can be viewed as a perturbation (dark red peak) to the phonon spectrum, which is ordinarily determined by a Planck distribution for a given temperature. Since the acoustic wave contains a large number of coherent phonons which are not in thermal equilibrium, given enough time there is sufficient probability for the acoustic phonons to scatter out of their coherent state by collision with thermal phonons via normal and umklapp processes. The characteristic time scale on which this process occurs is termed the phonon relaxation time and sets the rate of exponential decay of the acoustic wave.

Interaction of an acoustic wave propagating in the resonator with thermal lattice motions (thermal phonons) results in acoustic energy dissipation. Since the number of thermal

phonons depends on the temperature, acoustic attenuation from this mechanism is also a strong function of temperature. At low temperatures, where lattice vibrations are small, the resulting energy dissipation is negligible and other mechanisms besides phonon-phonon interactions typically dominate the energy dissipation of the acoustic wave. However, at higher temperatures, lattice vibrations increase, which translates into more interaction of the acoustic wave with thermal phonons and increased energy dissipation. In general, these interactions depend on the acoustic wave polarization (either longitudinal or shear wave) and propagation direction. In most cases, the acoustic attenuation of longitudinal waves differs from attenuation of shear waves propagating in the same direction and at the same frequency by about ten times, while the qualitative temperature dependence is similar [62]. Two main fundamental physical mechanisms have been discovered which result in acoustic attenuation due to the interactions of acoustic waves with thermal phonons:

1. In the mechanism introduced by Akhieser [6], the acoustic wave is regarded as a macroscopic strain field in the crystal (i.e., its wavelength is long compared with the thermal phonon mean-free path). Since the frequency-wavelength dispersion of thermal phonons depends on the strain state of the crystal lattice, the thermal equilibrium of the thermal phonons is disturbed and the total collection of thermal phonons must transfer their energy between branches [12]. The process of restoring thermal equilibrium to the phonon population is accompanied by energy dissipation as there is a finite probability for the acoustic phonons to transition into the unfilled equilibrium states.

2. An alternative mechanism was given by Landau and Rumer [43], where the acoustic wave is regarded as a parallel beam of low-energy phonons. Because of anharmonic terms in the internal energy of the crystal, interactions between different phonon modes are possible and the acoustic phonon scattering rate can be calculated using perturbation theory by considering a three-phonon scattering process (a

thermal phonon and an acoustic wave phonon combine into one scattered thermal phonon) [43]. Due to the nature of the Landau-Rumer mechanism as the interaction of individual phonons, it dominates when the acoustic wavelength is on the order of the thermal phonon mean-free path or shorter.

Hence, Q_{PhPh} can be broken into two main parts: Akhieser Q_{AKE} and Landau-Rumer $Q_{\text{L-R}}$. Details of these two Q regimes and the transition between them are provided in the next three sections.

2.3.2 Akhieser Regime (Q_{AKE})

If the acoustic wavelength λ_a is considerably larger than the mean free path of the phonons such that $\omega << 1/\tau_{\text{th}}$, the acoustic wave is assumed to be interacting with the whole ensemble of thermal phonons, and therefore locally changes the phonon frequencies and perturbs the phonon distribution function away from its equilibrium Planck form. This range $\omega << 1/\tau$ is known as the Akhieser regime. Akhieser dissipation is related to the creation of alternating strain regions in the propagation of acoustic waves through the material. This also means that the alternating strain regions are well-spread spatially, so that the acoustic wave influences the phonon dispersion within each strain region (Figure 8). However, as opposed to thermoelastic dissipation discussed later, this modification to the dispersion curve (and thermal phonon equilibrium) can occur for both compressive and rarefied strains (longitudinal waves) as well as alternating shear strains (shear or transverse waves). The main concern in this section is to obtain an expression for Q_{AKE} for insulating crystalline solids close to room temperature, which will be applied as an approximation for other cases.

The acoustic absorption coefficient can be found in the Akhieser regime as [58]

$$\alpha_{\text{AKE}}(\omega) = \frac{C_P T_0 \bar{\gamma^2}}{2 v_a^3} \frac{\omega^2 \tau_{\text{th}}}{1 + \omega^2 \tau_{\text{th}}^2}, \tag{10}$$

where T_0 is the absolute temperature, C_P is the specific heat capacity per unit mass, $\bar{\gamma^2}$ is an

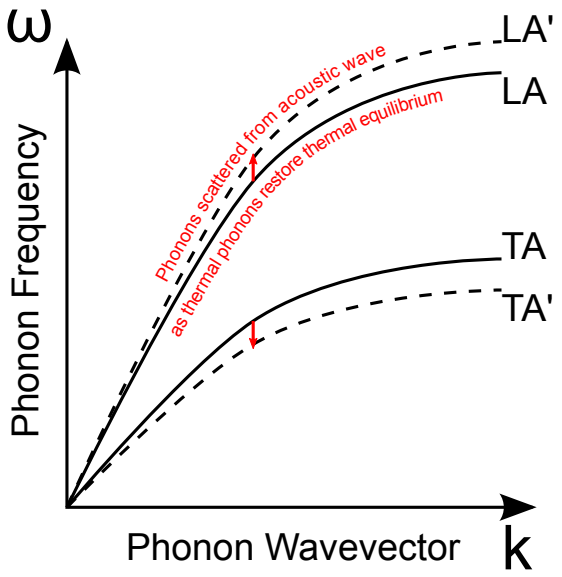

Figure 8: Schematic depiction of acoustic wave induced modifications to the phonon dispersion curves which induce Akhieser-type dissipation. The regions of alternating strain induced by the passage of an acoustic wave locally shift the phonon dispersion curves within that region, altering the thermal equilibrium distribution of phonons. The fractional frequency change of each phonon branch can be related to a strain in the j^{th} direction by the Grüneisen coefficient γ_k^j. There is a net shift of energy between phonon branches. The Akhieser dissipation is caused by the finite temporal relaxation of the old equilibrium distribution to the new equilibrium distribution, wherein the phonons making up the acoustic wave have a finite probability to be converted to a thermal phonon by normal and umklapp scattering processes. [58]

effective mean-square Grüneisen constant (the mean-square average of the fractional frequency changes of each phonon branch when strain is applied), τ_{th} is the average relaxation time of the thermal phonons, and v_D is the effective Debye velocity of the material. This latter quantity can be approximated as

$$3v_D^{-3} = v_{at1}^{-3} + v_{at2}^{-3} + v_{al}^{-3}, \tag{11}$$

and τ_{th} can be found from the thermal conductivity where

$$\kappa = \frac{1}{3}\rho C_P v_D^2 \tau_{\text{th}}. \tag{12}$$

An approximate value for γ can be found as

$$\gamma = 3\alpha\kappa/\rho C_P. \tag{13}$$

Combining the above, Q_{AKE} can be expressed as

$$Q_{\mathrm{AKE}}(\omega) = \frac{v_a^2}{C_P T_0 \bar{\gamma}^2}\left(\frac{1}{\omega\tau_{\mathrm{th}}} + \omega\tau_{\mathrm{th}}\right). \tag{14}$$

Minor modifications can be made as necessary to account for the character of the acoustic propagation (propagation and polarization directions), but the above expression will give an excellent order-of-magnitude approximation in most cases. From (14), it is seen that Q_{AKE} varies inversely with frequency for $\omega << 1/\tau_{\mathrm{th}}$ and increases proportionally to frequency for $\omega >> 1/\tau_{\mathrm{th}}$. Hence, there is a minimum frequency for Q_{AKE}, which can be expressed as

$$f_{\mathrm{min.}Q_{\mathrm{AKE}}} = \frac{1}{2\pi\tau_{\mathrm{th}}} = \frac{\rho C_P v_D^2}{6\pi\kappa} \tag{15}$$

2.3.3 Landau-Rumer Regime

When λ_a is less than the phonon mean free path, the acoustic quanta interact with individual lattice phonons. In the Landau-Rumer regime ($\omega >> 1/\tau_{\mathrm{th}}$), acoustic attenuation is mainly due to direct three-phonon interactions and is linearly proportional to ω [43, 58]:

$$\alpha_{\mathrm{L\text{-}R}t}(\omega) = \frac{\pi k_B^4 T_0^4 \gamma_t^2 v_{at}^2}{80\rho\hbar^3 v_{al}^8}\left(1 - \left(\frac{v_{at}}{v_{al}}\right)^2\right)\omega, \tag{16}$$

for transverse waves, and

$$\alpha_{\mathrm{L\text{-}R}l}(\omega) = \frac{\pi k_B^4 T_0^4 \gamma_l^2}{80\rho\hbar^3 v_{al}^6}\omega, \tag{17}$$

for longitudinal waves, where $\hbar$ is Planck's constant and k_B is Boltzmann's constant. The main difference stems from longitudinal acoustic waves being prevented from coupling

with transverse phonons according to the phonon dispersion relations. Since $\alpha_{\text{L-R}}$ is proportional to ω, according to (9), $Q_{\text{L-R}}$ is constant over ω:

$$Q_{\text{L-R}t}(\omega) = \frac{40\rho\hbar^3 v_{al}^8}{\pi k_B^4 T_0^4 \gamma_t^2 v_{at}^3 (1 - (v_{at}/v_{al})^2)}, \tag{18}$$

and

$$Q_{\text{L-R}l}(\omega) = \frac{40\rho\hbar^3 v_{al}^5}{\pi k_B^4 T_0^4 \gamma_l^2}. \tag{19}$$

It is interesting to note that this type of dissipation appears to be hysteretic according to the classifications found in Table 3, although Landau-Rumer dissipation cannot be ascribed to a hysteresis mechanism.

2.3.4 Transition from Akhieser Regime to Landau-Rumer Regime

Since the Landau-Rumer mechanism is limited to wavelengths shorter than the mean-free path of the thermal phonons, that means it is only active at frequencies above the thermal relaxation frequency, which is the same as the minimum frequency for Q_{AKE} given by (15). Below this frequency, the Akhieser mechanism is expected to dominate the phonon-phonon dissipation, and above it Landau-Rumer dissipation will dominate, setting a constant ultimate Q over the high frequencies. The significance of this effect is pronounced at frequencies above 750 MHz in Si, where the product of frequency and quality factor fQ increases with frequency (Figure 9). The transition frequency is a strong function of temperature, and it is almost always beneficial to reduce the temperature to decrease phonon-phonon dissipation.

2.3.5 Phonon-Electron Interactions

One of the intrinsic dissipation mechanisms which attenuates propagating acoustic waves in semiconductors and metals is the interaction of acoustic phonons with mobile charges.

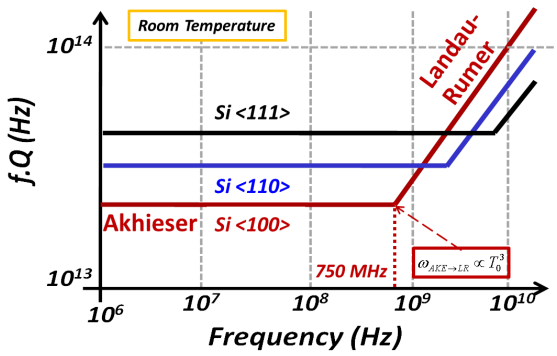

Figure 9: Comparison of fQ_{PhPh} for longitudinal acoustic waves propagating in various crystal directions of single-crystalline silicon (SCS).

Phonon-electron interactions can either be destructive—resulting in attenuation—or constructive, resulting in acoustic wave amplification [36]. Mobile charges can be generated by impurities introduced in semiconductors or by thermal excitation. Considering that the number of mobile charges is a weak function of temperature in doped semiconductors, the dependence of this dissipation mechanism on temperature is less than the dissipation due to interaction of the acoustic wave with thermal phonons. The coupling between acoustic wave and mobile charges can be categorized in two ways:

1. Since the electron energy in a conduction band depends upon the strain state of the lattice [62], standing waves created in the resonator result in a "deformation potential" which is directly proportional to the strain induced in lattice. This potential results in undesired flow of mobile charges in semiconductor and dissipates acoustic energy due to ohmic loss and is often the dominant dissipation mechanism in metal resonators.

2. In piezoelectric semiconductors such as AlN and GaN, coupling between an acoustic wave and mobile charges result from the piezoelectric characteristics of the material. The acoustic wave in the piezoelectric material creates alternating regions of dielectric polarization by the piezoelectric effect, resulting in drift of mobile charges and ohmic dissipation, as well as loss through the dielectric loss tangent.

Concentrating on the first category of phonon-electron interactions, which is most frequently encountered in practice, an expression for the Q is [12]

$$Q_{\mathrm{PhEl}} = \frac{15}{8}\frac{\rho v_a^2 e^2}{\epsilon_F m_e \sigma_e \omega}. \tag{20}$$

2.3.6 Acoustic Thermoelastic Dissipation (TED)

Thermoelastic dissipation (TED) is a fundamental energy loss process which bears concern in all microelectromechanical resonators. Similar to Akhieser dissipation, thermoelastic dissipation occurs in longitudinal acoustic waves which create regions of compressive and rarefied strain. However, for purely shear waves, no volumetric change occurs, so the temperature remains constant. Thus, TED does not impact shear waves (although practical shear wave devices can have some longitudinal components due to their finite dimensions, resulting in TED). The regions of compressive and tensile strain in the longitudinal wave become hotter and colder, respectively, due to thermodynamic principles, forming thermal gradients throughout the body of the device which lead to losses in the form of irreversible heat transfer from hot spots to cold spots. TED can be first addressed by considering the device operating frequency and geometric dimensions. It has been shown that a dimensionally-dependent minima of Q_{TED} separates isothermal and adiabatic regions of increasing Q_{TED} [47], [4]. By choosing the geometric parameters—and hence, operating frequency—judiciously, the device can be designed to operate in either region of high Q_{TED}. For typical MEMS devices, in isothermal operation, the vibration period is long enough that thermal equilibrium is mostly maintained and the temperature remains effectively constant throughout the device. In adiabatic operation, the frequency is high enough that mechanically-induced thermal gradients cannot quickly dissipate sufficient quantities of heat. Higher frequency usually implies that the thermoelastic dissipation effect is located in the adiabatic region, where Q_{TED} increases with decreasing device dimension, rather than near the minimum Q_{TED} valley present in some flexural devices [47], [4], [93]. However,

for longitudinal waves, since the thermal path is proportional to the wavelength, the adiabatic operation actually occurs at lower frequencies, while the isothermal operation occurs when the wavelength becomes short enough that the temperature gradients can diffuse out. An expression for Q_{TED} in a longitudinal acoustic wave can be found as [12]

$$Q_{\mathrm{TED}} = \frac{9\rho C_P^2}{\kappa T_0 \alpha^2 \omega} \tag{21}$$

2.3.7 Quasi-Intrinsic and Other Dissipation Mechanisms

A broad category of remaining dissipation mechanisms include intergranular TED and a variety of mechanisms caused by impurities, defects, dislocations, vacancies, isotopic scattering, lattice mismatches, and grain boundary scattering. These mechanisms are termed quasi-intrinsic due to their origin with non-idealities in the material while retaining their intrinsicality when the resonator dimensions are much greater than the average size of the defect which causes dissipation. TED generated by the random orientation of the grains has been first studied by Zener [98] and found to depend on the grain size. TED generated by grains in polycrystalline materials generally affects very high-frequency operation due to the small grain size; for example, a large dissipation peak occurs at close to 14 GHz in polysilicon [86]. Grain boundary and defect scattering are phonon scattering mechanisms that depend on grain size in polycrystallites and defect density, respectively. Defect-induced dissipation is typically higher than other intrinsic loss mechanisms for most materials unless extra care is taken when creating them. They appear as an effective viscosity for the material. These mechanisms can be mitigated with high quality, single-crystal material growth.

2.4 Extrinsic Dissipation Mechanisms

2.4.1 Bulk Modal TED

TED results from the coupling of the vibrational domain into the thermal domain and the subsequent dissipation of the thermal energy via irreversible heat flow through thermal gradients. To quantify this dissipation, one should solve the governing equations of thermoelasticity distributed over the structure of interest. For general situations, such as implementation by the finite element method, it is convenient to work in Cartesian coordinates. Hence, for every point in the structure, one should solve (subject to appropriate boundary conditions) [4, 48]

$$\rho\frac{\partial^2 u_i}{\partial t^2} - \frac{E}{2\left(1+\nu\right)\left(1-2\nu\right)}\frac{\partial^2 u_j}{\partial x_i \partial x_j} - \frac{E}{2\left(1+\nu\right)}\frac{\partial^2 u_i}{\partial {x_j}^2} = -\frac{\alpha E}{\left(1-2\nu\right)}\frac{\partial T}{\partial x_i} \tag{22}$$

$$\rho C_P \frac{\partial T}{\partial t} - \kappa\frac{\partial^2 T}{\partial {x_i}^2} = -\frac{\alpha E}{3\left(1-2\nu\right)}T_0\frac{\partial \epsilon_{ii}}{\partial t}, \tag{23}$$

where u_i represents the displacement in the x_i^{th} direction, t represents time, and σ_{ij} and ϵ_{ij} are the linearized stress and strain components. T_0 is the ambient temperature of the device and T is the localized temperature offset from ambient. The remaining material properties are the linear coefficient of thermal expansion α, the specific heat C_P, and the thermal conductivity κ. The preceding equation applies for homogeneous isotropic material. For an anisotropic material, such as single-crystalline silicon, the above must be reformulated to

$$\rho u_{i,tt} - \left(c_{ijkl}u_{k,l}\right)_{,j} = -c_{ijkl}\alpha_{kl}T_{,j} \tag{24}$$

$$\rho C_P T_{,t} - \left(\kappa_{ij}T_{,i}\right)_{,j} = -T_0 K_{\text{an.}}\alpha_{ij}u_{i,jt}, \tag{25}$$

where α and κ are now treated as tensors, $K_{\text{an.}} = \frac{1}{9}C_{ijkl}\delta_{ij}\delta_{kl}$ is the anisotropic bulk modulus, the Einstein repeated index convention applies to the tensors, and an index after a comma represents a derivative with respect to the corresponding variable.

As a concrete example, consider disk resonators such as the type shown in Figure 10. Single-crystalline silicon (SCS) solid disks can be operated in a many modes, which are labeled with the index m (Figure 11). These modes were simulated in COMSOL multi-physics finite element software after implementing the fully-anisotropic and fully-coupled TED equations given by (24) and (25). For the case of $m = 0$, the vibration pattern corresponds to radial expansion in all directions (often termed the breathing mode). Since silicon is anisotropic, the displacement is not uniform around the circumference of the disk. For this mode, coupled thermoelastic COMSOL finite element simulations predict a Q_{TED} of 46 million. For $m = 2$, the anisotropy of the silicon causes a split into two modes, one with anti-nodes aligned with the <100> directions of the disk and the other with the anti-nodes aligned with the <110> directions of the disk. Q_{TED} in these cases will be 680 million and 530 million, respectively, indicating that the $m = 2$ mode is preferred for low TED. For $m = 3$, Q_{TED} of a solid SCS disk is 85 million.

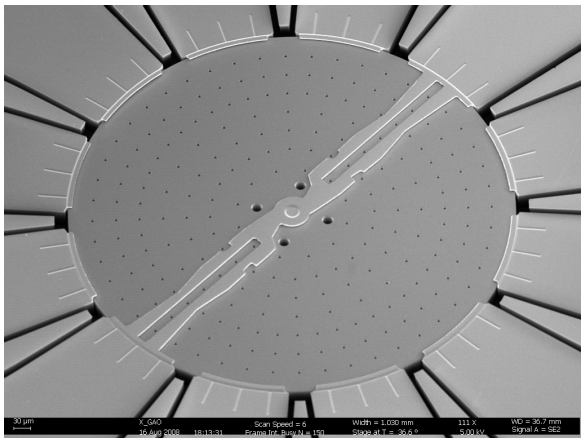

Figure 10: SEM view of an 800 μm diameter bulk acoustic wave (BAW) disk gyroscope with uniform 6 μm diameter holes in 40 μm thick silicon-on-insulator (SOI) substrate.

However, from a practical standpoint, the disk resonator often is large in size, so it requires perforations or release holes during fabrication to ensure that it is fully released from the underlying substrate during the release etch process. Adding release holes in a uniformly-distributed pattern without regard to their position in the disk drastically reduces the attainable Q by creating local thermal gradients about the hole circumference as the

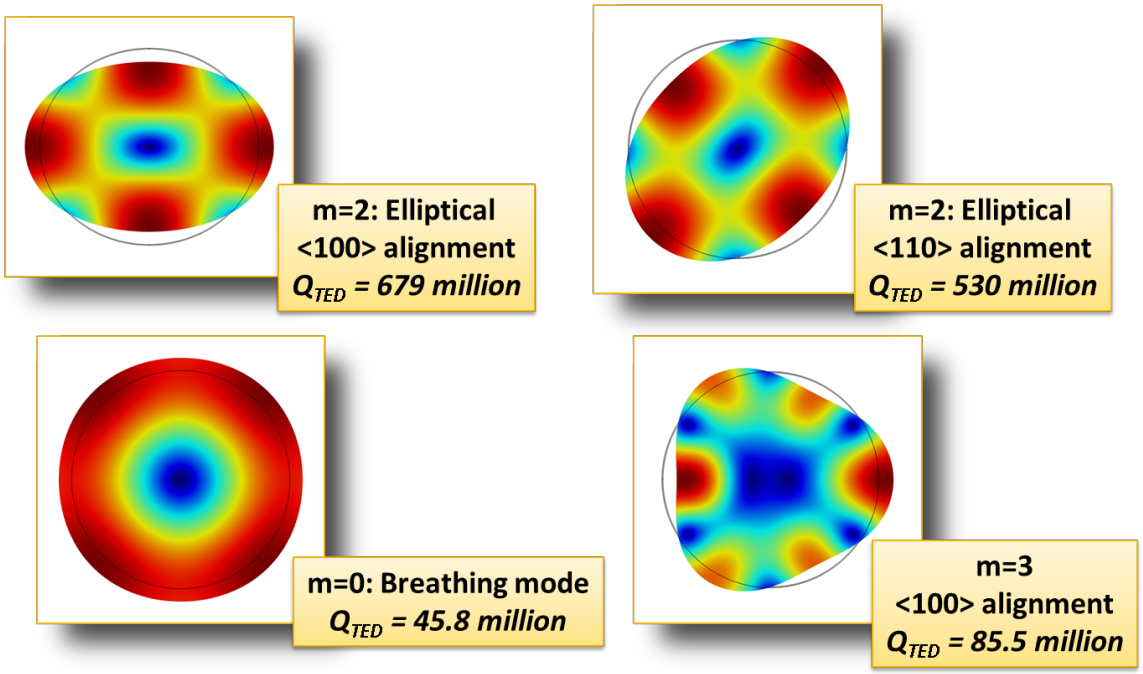

Figure 11: Finite element simulations of fundamental bulk acoustic wave (BAW) modes of a single-crystalline silicon (SCS) disk fabricated on an (001) wafer using anisotropic fully-coupled TED formulation of (24) and (25) implemented in COMSOL multiphysics finite element software.

disk deforms. For the $m = 2$ mode aligned to the <100> directions of the silicon disk, as shown in Figure 12, Q_{TED} will be 182,000, which is a substantial drop from 680 million obtained earlier for the solid disk. Therefore, the number of holes should be restricted and their placements carefully considered to minimize TED.

Ultimately, the Q determined by TED of a single relaxation mechanism of the structure can be well approximated by [4, 47]

$$Q_{\text{TED}}^{-1} = \Delta_E \frac{\omega\tau_{\text{th}}}{1 + (\omega\tau_{\text{th}})^2}, \tag{26}$$

where Δ_E is the relaxation strength of the Young's Modulus defined by

$$\Delta_E = \frac{E\alpha^2 T_0}{\rho C_P} \tag{27}$$

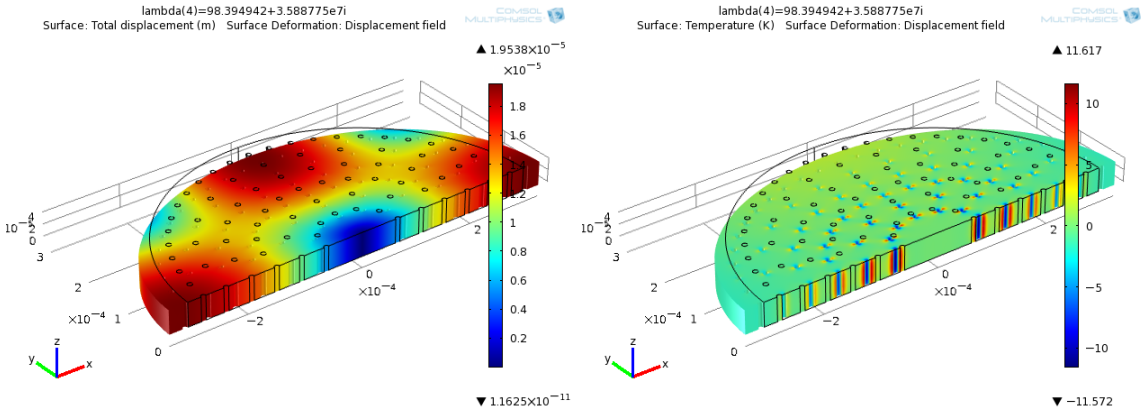

Figure 12: Displacement and temperature fields for coupled eigenvalue thermoelastic solution of m=2 mode of anisotropic Ø 600 µm x 40 µm SCS disk with release holes obtained from COMSOL finite element analysis: (left) isometric view of the modal displacement field; (right) isometric view of the modal temperature field. A half disk with symmetry boundary condition is used to reduce computational complexity. Note the development of thermal gradients around the circumference of each release hole as the disk deforms.

and the thermal relaxation time constant τ_{th} is given by

$$\tau_{\text{th}} = \frac{\rho C_P {d_{\text{th}}}^2}{\pi^2 \kappa}. \tag{28}$$

In the above, ω is the driven angular frequency and d_{th} is the thermal path length defined by the temperature distribution over the structure. A key point of this dissertation is determining d_{th} as a function of the geometry of the MEMS resonator in question. If ω is low enough that the typical resonator is operated in the isothermal region where $\omega\tau_{\text{th}} << 1$, (26) reduces to

$$Q_{\text{TED}}^{-1} = \Delta_E \omega \tau_{\text{th}}. \tag{29}$$

Alternatively, other MEMS resonators have a high modal stiffness. It is usually safe to assume these operate in the adiabatic TED regime, for which

$$Q_{\text{TED}}^{-1} = \frac{\Delta_E}{\omega \tau_{\text{th}}}. \tag{30}$$

2.4.2 Support Loss (Q_{Support})

Support loss is defined by radiation of energy from the device to the surroundings through vibration of the supporting structure which is the result of non-ideality of the clamp size (finite width). This process is depicted conceptually in Figure 13. Many analytical [28], [25], [27], [2] and numerical [11], [95], [96] approaches have been developed to predict support loss. The most popular calculation approach is the perfectly-matched layer (PML) method [11]. In this method, the radiation of acoustic energy into the support is captured by an artificial domain, inside which a complex coordinate transformation is applied to damp out the waves without creating reflection at the interface.

One method of increasing Q_{Support} is to design the location of the support structure where the acoustic wave amplitude is minimal, such as the center of a BAW disk resonator. Second, one may exploit acoustic impedance mismatch to reflect outgoing acoustic waves back to the resonator [92]. Another method is to design the resonator geometry itself to concentrate the acoustic energy far from the supporting area [72]. This approach is illustrated in Figure 14.

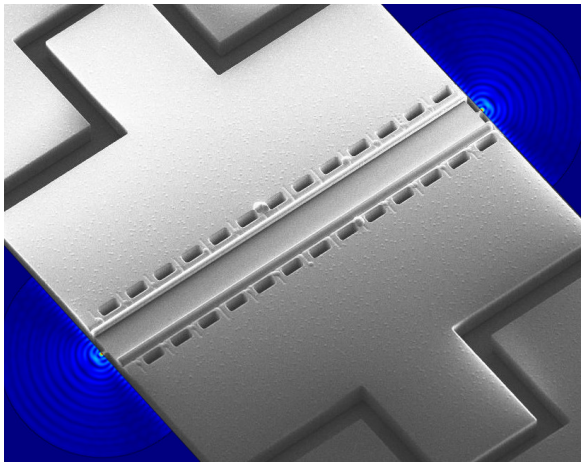

Figure 13: Schematic diagram of acoustic energy radiating from supports of a SiBAR resonator.

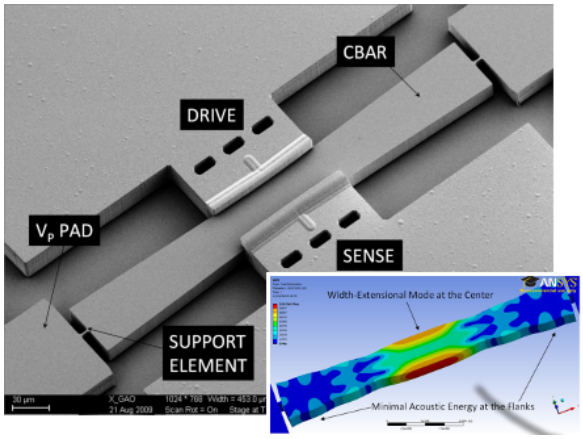

Figure 14: Resonator geometry can be modified to concentrate acoustic energy away from the support tethers in a capacitive single-crystal silicon BAW resonator. This results in an ultra-high quality factor near the predicted intrinsic fQ limit for single-crystal silicon, while the shear strain modulation results a low TCf of -6.31 ppm/°C [72].

2.4.3 Calculating Q_{Support} via the Acoustic S-Parameter Method

In this section, a novel method is developed for calculating the support loss of a MEMS resonator. This method was inspired by the use of S-parameters in microwave engineering. However, contrary to electrical quantities, which can be considered as lumped quantities on the ports of an electrical network, the acoustic quantities of interest when calculating support loss are distributed over the boundaries of the resonator. A similar approach was outlined in [7], but the acoustic ports were considered in terms of plane waves only. The acoustic quantities are the particle surface tractions, T_i and the particle velocities v_i. The surfaces which define the boundaries of the MEMS resonator can be assigned parameters to represent the two dimensions of each surface, e.g., ξ and η. By analogy to the electrical S-parameters, the acoustic S-parameters give the relation between incoming and outgoing stress waves:

$$S_{ij}(\xi,\eta) = \left.\frac{T_i^-(\xi,\eta)}{T_j^+(\xi,\eta)}\right|_{T_{k\neq j}^+(\xi\neq\xi_j,\eta\neq\eta_j)=0}. \tag{31}$$

where ξ and η correspond to a particular but non-specific surface. The above definition also requires specification of the acoustic port impedances. The acoustic impedance (inverse

admittance) is defined as

$$Z_n = -\frac{T_n}{v_n} = 1/Y_n, \tag{32}$$

the magnitude of which can be calculated as

$$|Z_n| = \rho \cdot v_a. \tag{33}$$

Taking the electrical S-parameter analogy further and making use of the acoustic impedance definition, the relation between T_n, v_n and T_n^+, T_n^- is

$$\begin{aligned} T_n &= T_n^+ + T_n^- \\ v_n &= v_n^+ - v_n^- = \frac{T_n^+ - T_n^-}{Z_n}. \end{aligned} \tag{34}$$

Taking the ratio of the above,

$$\frac{v_n}{T_n} = \frac{T_n^+ - T_n^-}{T_n^+ + T_n^-} Y_n = \frac{1 - \Gamma_n}{1 + \Gamma_n} Y_n, \tag{35}$$

where $\Gamma_n = T_n^-/T_n^+ = S_{nn}$ is the reflection coefficient. The above can be solved for T_n^+ and T_n^-, resulting in

$$\begin{aligned} T_n^+ &= \frac{1}{2}\left(T_n + Z_n v_n\right) \\ T_n^- &= \frac{1}{2}\left(T_n - Z_n v_n\right). \end{aligned} \tag{36}$$

The ratio of the above is the reflection coefficient, so

$$S_{nn}(\xi,\eta) = \Gamma_n(\xi,\eta) = \frac{T_n^-(\xi,\eta)}{T_n^+(\xi,\eta)} = \frac{T_n(\xi,\eta) + Z_n v_n(\xi,\eta)}{T_n(\xi,\eta) - Z_n v_n(\xi,\eta)}. \tag{37}$$

The meaning of Q_{Support} must be established in terms of the acoustic S-parameters. Consider a "2-port" network in which one port represents the boundaries of the vibration mode of the structure and the other port is the surface of the boundary between the resonator and its

attachment. "2-port" is written in quotes since there are an infinite number of ports over the boundaries in the continuous S-parameter representation here. In matrix form,

$$\begin{Bmatrix} T_s^-(\xi,\eta) \\ T_n^-(\xi,\eta) \end{Bmatrix} = \begin{bmatrix} S_{ss}(\xi,\eta) & S_{sn}(\xi,\eta) \\ S_{ns}(\xi,\eta) & S_{nn}(\xi,\eta) \end{bmatrix} \begin{Bmatrix} T_s^+(\xi,\eta) \\ T_n^+(\xi,\eta) \end{Bmatrix}. \tag{38}$$

In the above, if T_n^+ is zero, as can be expected for the passive support element, then

$$\begin{aligned} T_s^- &= S_{ss} T_s^+ \\ T_n^- &= S_{ns} T_s^+. \end{aligned} \tag{39}$$

The Q due to loss of vibrational energy through port n can be directly found as

$$Q_{\text{Support}} = 2\pi \frac{P_s^+}{P_n^-} = \frac{2\pi}{|S_{sn}(\xi,\eta)|^2}. \tag{40}$$

To find the power on each port, the acoustic Poynting vector should be integrated over the corresponding boundary. This leads to

$$Q_{\text{Support}} = 2\pi \frac{\int_{A_s} \sum_i \left(|T_i(\xi,\eta)|^2 / Z_{si} + Z_{si} |v_i(\xi,\eta)|^2 \right) dA}{\int_{A_n} \sum_i \left(|T_i(\xi,\eta)|^2 / Z_{ni} + Z_{ni} |v_i(\xi,\eta)|^2 \right) dA}. \tag{41}$$

Strictly speaking, the two terms in each of the integrals should be equal to the magnitude of the acoustic Poynting vector, but both are included to average them in case of any small discrepancies in the FE solutions.

In general, it is desired to calculate the worst-case lower bound on Q_{Support} so that one may say the final Q is guaranteed to be above a certain value. Since there is no energy removed from the system if the resonator anchor boundaries are perfectly fixed or stress-free, then clearly there will be no support loss in those situations and Q_{Support} can increase without bound. The opposite case occurs when the resonator is acoustically matched at its anchor boundaries. The best acoustic match for the resonator is the resonator itself.

This condition is illustrated for a SiBAR in Figure 15. In COMSOL, symmetry and anti-symmetry boundary conditions were used to artificially mirror the SiBAR onto itself, respectively. In the case of anti-symmetric loading, the main acoustic propagation out of the SiBAR support is in the normal direction to the support boundary. However, for the symmetric loading, the main acoustic propagation is polarized in the transverse direction. It is found that the normal propagation is significantly higher in magnitude than the transverse propagation for the cases studied in this dissertation, but in general both loadings should be considered and a final Q calculated according with (7).

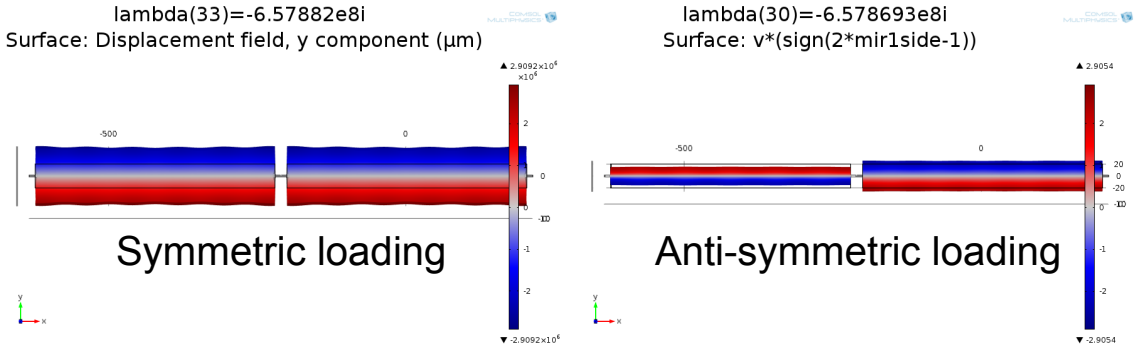

Figure 15: Symmetric (left) and anti-symmetric (right) acoustically-mirrored loading condition for SiBAR.

In order to justify the approach outlined above, the Q_{Support} should be benchmarked against a known support loss limited resonator. The radial breathing modes (Figure 16) of the diamond disk studied by [92] provides an ideal benchmark, since analytical calculations are also available [27]. Tables 4 through 6 compare the Q_{Support} calculated by the acoustic S-parameter method with the results presented in [27]. Good agreement is obtained in most cases, and the process corners are confirmed to show the same qualitative behavior.

2.4.4 Air-fluid Damping (Q_{Air})

Air-fluid damping occurs when a MEMS device operates in a gaseous or liquid environment. Due to vibrations at the device surface, a net force is exerted on the molecules of the surrounding fluid medium. The work done by this force compresses and displaces the gas from its equilibrium position, causing irreversible thermodynamic losses in the gas similar

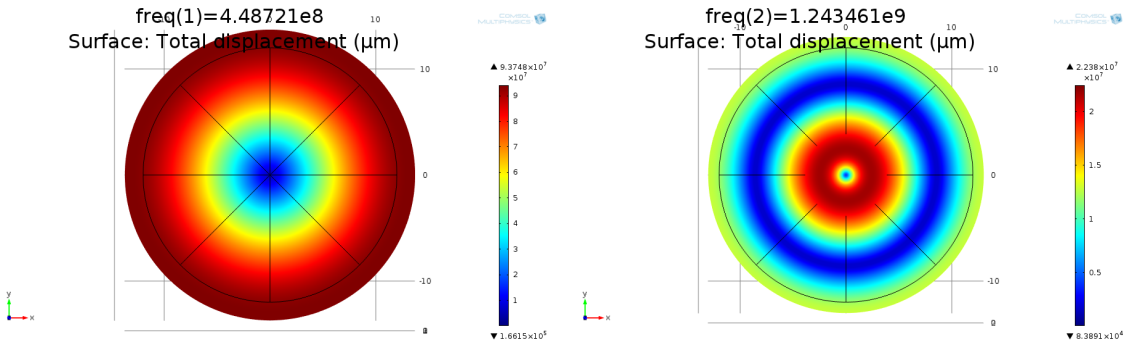

Figure 16: The first and second radial breathing modes of a disk resonator.

Table 4: Comparison of best-case support loss radial bulk modes of a disk resonator (R_{disk} = 12 μm, H_{disk} = 3 μm, r_{support} = 0.6 μm, h_{support} = 1 μm) calculated by acoustic S-parameters compared with analytical model in [27] and measured results of [92].

Radial bulk mode freq.	Q_{measured} [92]	Best Q_{Support} [27]	Best Q_{Support} (S-params)
f_1 = 448.7 MHz	24117	139180	82360
f_2 = 1243.3 MHz	12050	24575	4174

to TED in a solid [37]. Because MEMS devices often utilize narrow gaps in the sub-micrometer range, squeeze-film damping is commonly observed [10], [91]. If the gaps are large, the device will operate in the molecular regime, where the quality factor is expected to be inversely proportional to absolute pressure. A hermetically sealed micro-vacuum package can be used to avoid the effects of air damping [56].

Table 5: Comparison of nominal support loss radial bulk modes of a disk resonator (R_{disk} = 12 μm, H_{disk} = 3 μm, r_{support} = 0.8 μm, h_{support} = 0.8 μm) calculated by acoustic S-parameters compared with analytical model in [27] and measured results of [92].

Radial bulk mode freq.	Q_{measured} [92]	Nom. Q_{Support} [27]	Nom. Q_{Support} (S-params)
f_1 = 448.7 MHz	24117	28698	44777
f_2 = 1243.5 MHz	12050	12205	3466

Table 6: Comparison of worst-case support loss radial bulk modes of a disk resonator (R_{disk} = 12 μm, H_{disk} = 3 μm, r_{support} = 1 μm, h_{support} = 0.6 μm) calculated by acoustic S-parameters compared with analytical model in [27] and measured results of [92].

Radial bulk mode freq.	Q_{measured} [92]	Worst Q_{Support} [27]	Worst Q_{Support} (S-params)
f_1 = 448.7 MHz	24117	6718	28079
f_2 = 1243.7 MHz	12050	6226	2868

2.4.5 Surface and Interface Loss (Q_{Surface})

Q_{Surface} is affected by scattering losses on the device surface, which can be improved by careful processing [4]. The DRIE process is known for creating scallops on the trench sidewalls; however, recent advances have made it possible to reduce scalloping effects. Nitridation of the sidewall during HARPSS nano-gap fabrication process results in a very smooth trench profile, resulting in little surface scattering and high values of Q_{Surface} [71]. Hydrogen annealing is also available to reflow the silicon surface. A related effect, interface scattering, is especially important in composite laminar MEMS devices such as piezoelectrically-transduced resonators. This has been investigated analytically from the continuum mechanics approach [29]. Coating of devices must be done carefully to ensure a good quality adhesion which is free of voids between the coating layer and the resonator.

2.4.6 Dielectric Loss Tangent and Electrical Loading

Dielectric loss results from imperfect insulation of real dielectric materials, creating a shunt parasitic path to ground in the device equivalent circuit model [60]. This parasitic resistance is determined by the dielectric loss tangent of the material, and impacts the overall Q of the BAW MEMS device by electrically loading the input and output terminals. Electrical loading can impact the Q if significant mismatch exists between the device motional resistance and the sustaining amplifier [3].

2.5 Summary of Energy Dissipation Mechanisms

In this chapter, the major energy dissipation mechanisms which limit the Q of resonant MEMS devices have been reviewed. These effects may be intrinsic or quasi-intrinsic, depending on material properties and quality of material growth or extrinsic, depending on the design and fabrication non-idealities of the device.

Major intrinsic dissipation mechanisms limiting Q in micromechanical resonators were described. The dependency of intrinsic dissipation mechanisms on temperature, frequency, propagation direction and polarization of the acoustic wave in resonators as well as operating mode were discussed qualitatively. Quantitative criteria, such as Debye temperature and phonon relaxation time, can be used to compare and choose the best material, resonance mode and direction for the desired frequency range of operation. For this purpose, the intrinsic Q limit as a function of frequency may be compared for materials commonly used to implement micromechanical resonators. Different effects resulting from the coupling between mechanical and electrical domains in metals, doped semiconductors, and piezoelectric materials were briefly described. This coupling leads to further dissipation of acoustic energy in resonators.

Several extrinsic dissipation mechanisms were also described. The main extrinsic Q-limiting dissipation mechanisms of concern to the resonant MEMS designer are bulk TED, support loss, and air damping, while the others (surface, electrical loss and loading) can be treated as additional parasitic dissipation mechanisms. These mechanisms were described and several methods used to suppress and eliminate them reviewed. Careful consideration of the extrinsic and intrinsic dissipation mechanisms and operation in Landau-Rumer regime makes it theoretically possible to reach high Qs in GHz BAW micro- and nanomechanical resonators. Further, decreasing the temperature leads to less phonon-phonon dissipation in general.

CHAPTER III

DISSIPATION IN SIBAR AND TPOS BAW RESONATORS

This chapter serves as a bridge to connect the SiBAR and TPoS technologies with the Linear Acoustic Bandgap (LAB) structures presented in the next chapter. To understand the effect of LAB on the Q of the device, and its limitations in improving the overall Q, the dissipation mechanisms in SiBARs and TPoS resonators must be well-understood. The reason, as will be elaborated on in the next chapter, is that the LAB technology can be used for trapping acoustic energy within the body of the resonator, effectively eliminating the support loss contributor to Q, but it cannot eliminate other sources of dissipation, such as the aluminum nitride (AlN) layer added on top of a SiBAR to form a piezoelectrically-transduced TPoS resonator. In addition, predictive Q models for SiBAR and TPoS, taking into account their main energy dissipation mechanisms, respectively, had not yet been developed, and it is a useful contribution to apply the results of the preceding chapter to these technologies.

3.1 Intrinsic Dissipation in SiBARs

In this section, the main intrinsic dissipation mechanisms in silicon bulk acoustic resonators are considered. However, only phonon-phonon based effects are accounted for since phonon-electron dissipation will depend on the doping level of the silicon resonator and a single value cannot be ascribed until the doping level is known. Also, since experimental data is not readily available for MEMS resonators in the Landau-Rumer regime, the focus of this chapter is on SiBAR and TPoS resonators in the low UHF (30 MHz to 300 MHz) range.

3.1.1 Akhieser Dissipation in SiBARs

Using (14), (13), (12), and the material properties in Appendix A, values for Q_{AKE} can be calculated. It should be noted that using (13) and (12) are rough approximations. The Grüneisen coefficient which appears in (14) is a mean-square value which represents the average interaction of the particular acoustic wave defined by its propagation direction and polarization with the thermal phonon population, while (13) is a different average value which is determined by the thermal phonon contribution to thermal conductivity. Hence, these two values are not necessarily equal, but may be sufficiently close for many cases. A further point of note is that (12) is the lattice contribution, and must be separated from the electronic contribution to the thermal conductivity when relying on experimental values (which is important for metals or highly-doped semiconductors, i.e., silicon). Using this equation, approximate values for Q_{AKE} are given in Table 7 for the [100] and [110] directions of silicon for a 100 MHz SiBAR.

Table 7: Calculated values of Q_{AKE} for [100] and [110] directions of SCS according to (14).

Si Direction	Q_{AKE}
[100]	369,261
[110]	349,711

3.1.2 Acoustic TED in SiBARs

The Q_{TED} for a longitudinal acoustic wave can be calculated by (21). Since the thermal path depends on the wavelength only, differences in TED between different directions of propagation will be small, and a single value can be used. At 100 MHz, the Q_{TED} limit can be approximated as 54,896,237.

3.2 Bulk TED in BAW Resonators

In the preceding section, the intrinsic TED limit for a longitudinal acoustic wave was found to be close to 55 million. However, when the wave is confined to a resonator structure with finite dimensions, the propagating acoustic waves will reflect from the boundaries and form a standing wave pattern. This can disrupt the assumptions which go into (21). Instead, FE simulations can be performed to calculate TED, as were done for the bulk SCS disks in the previous chapter. Performing a similar set of simulations for an ideal SiBAR structure without support tethers, the Q_{BulkTED} is found to be just over 7.5 million (Figure 17), which is a factor of 8 less than the acoustic wave approximation. This is in agreement with the expectation that halving the thermal path will reduce the Q_{TED} by a factor of 4 and also that the temperature extremes are reduced by a factor of 2 in the SiBAR.

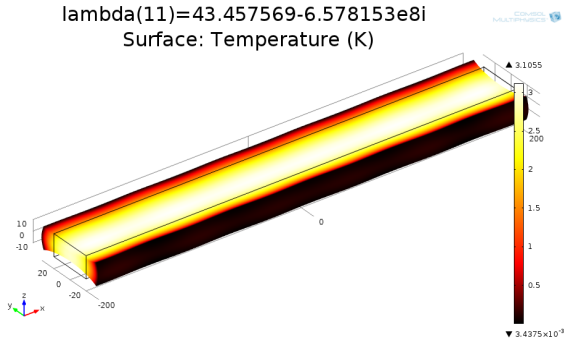

Figure 17: The temperature field when a SiBAR undergoes extensional vibration in the width direction corresponding to the mode shape shown in Figure 3 calculated using the fully-coupled finite element simulation approach developed in this work. The thermal path (distance from max T to min T) will be proportional to half the width of the SiBAR. For this resonator, the Q_{BulkTED} is just over 7.5 million. The dimensions of the SiBAR are 400 μm x 40 μm x 20 μm and it is aligned to the [110] direction of silicon.

3.2.1 Orientation Dependence of Bulk TED in SiBARs

The Q_{BulkTED} for the two main orientations of SiBARs is shown in Table 8. These values are calculated using a small section of the SiBAR and applying periodic boundary conditions to simulate a SiBAR of infinite length (Figure 18). The Q_{BulkTED} is slightly higher for the sectional models since the stress-free boundary condition at the end of the SiBAR allows it

to relax and creates a slight thermal gradient along its length.

Table 8: Calculated values of Q_{BulkTED} for [100] and [110] directions of SCS for sectional models of a SiBAR.

Si Direction	Q_{BulkTED}
[100]	5,367,380
[110]	7,700,038

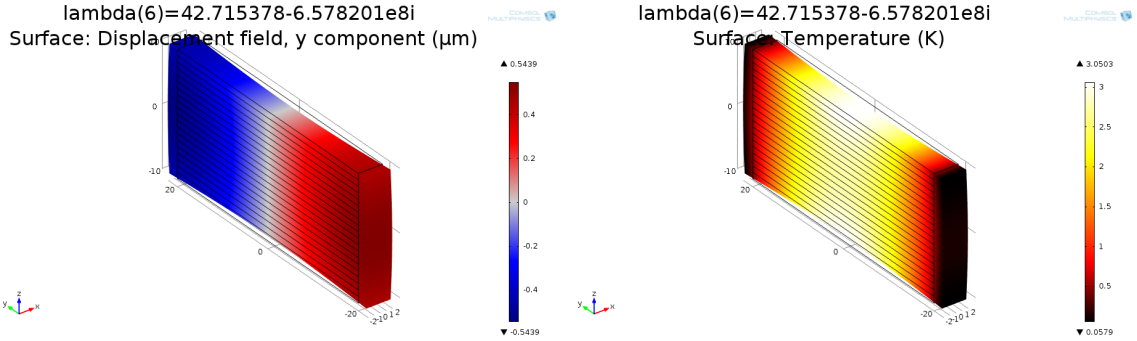

Figure 18: Sectional TED model of SiBAR oriented along the [110] direction of silicon with Q_{BulkTED} of 7.7 million, in good agreement with the full-length SiBAR model value of 7.5 million.

3.2.2 Effect of Scalloping on Bulk TED

During the DRIE silicon etch Bosch process, the etched trench sidewall will exhibit the characteristic scalloping pattern shown in Figure 19 which arises due to the isotropic nature of SF_6 etching. While techniques can be developed to mitigate or even eliminate the scalloping from the trench sidewalls, it is important to ascertain the impact of such scalloping on the Q to see how much surface improvement is necessary. It is known that improving the surface polish can improve that quality factor, but not necessarily the fundamental origin of the surface contribution to loss. TED is one possible mechanism, so it is investigated here.

Figure 20 shows the same sectional model of the SiBAR as in Figure 18 with several scallops cut out along its thickness direction on the sidewalls defined by the trench etch.

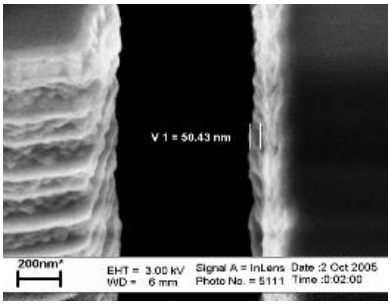

Figure 19: SEM image of DRIE scalloping. The scallop radius in this case is about 50 nm [31].

These scallops were purposefully made with a larger than typical radius to try to penetrate the center of the sectional model and incur the most effect on the TED. However, even with these large scallops, the Q_{BulkTED} only came down to 7.62 million from the 7.7 million obtained for the device without scallops. Therefore, scalloping (and other surface roughness) is not expected to be an important contributor to TED in SiBARs because the strain energy is concentrated along the center of the SiBAR and not at its surfaces where it would have the most effect.

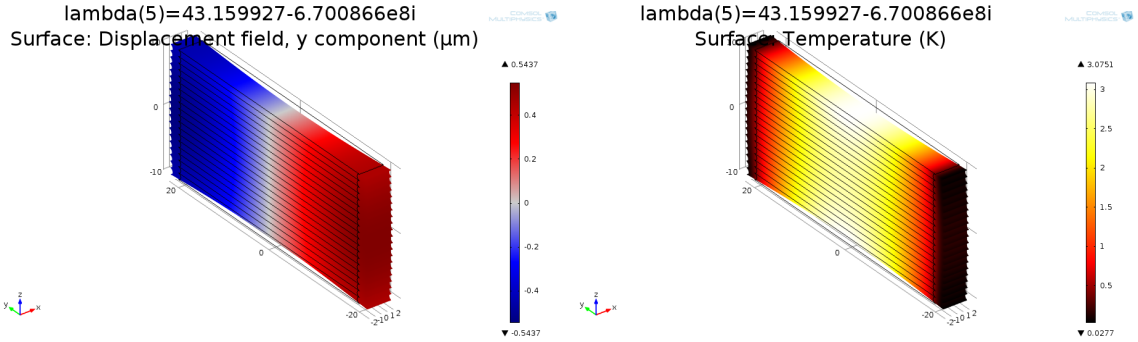

Figure 20: Displacement (left) and temperature (right) fields for a section of SiBAR resonance mode with 20 large scallops in the thickness direction (scallop radius = 0.5 μm). Similar mode shapes and temperature fields are obtained as for Figure 18, suggesting that the scalloping on the trenches will have little impact on TED. This is confirmed by the Q factors, which are 7.62 million and 7.7 million with and without scalloping, respectively.

3.3 Support Loss in SiBARs

Figure 21 shows the faces which are considered as part of the resonator system and those which are part of the anchor boundary. The loading conditions (symmetric and antisymmetric) were discussed previously and depicted in Figure 15. Solving for the eigenmode of interest, (41) can be applied to determine the Q_{Support} of the SiBAR, again for [100] and [110] orientations relative to silicon. These results are give in Table 9. The main reason for the difference in support loss between the two directions is that the Poisson's ratio of [110] silicon is close to 0.04, while for [100] silicon, it is nearly 10 times that amount, leading to a less uniform mode shape along the length of the SiBAR and more motion at the support tether.

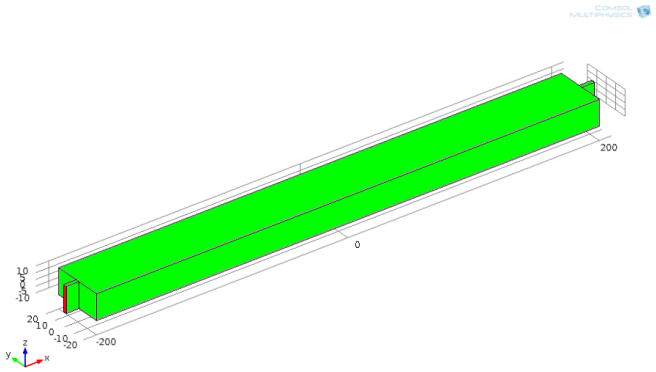

Figure 21: Schematic diagram of SiBAR showing which faces are considered as part of the system (s, colored green) and as part of the anchor (n, colored red) according to (41).

Table 9: Calculated values of Q_{Support} for [100] and [110] directions of SCS for entire-length models of a SiBAR including support tether. The SiBAR dimensions are the same as given previously, while the support tether dimensions are 10 μm by 3 μm.

Si Direction	Q_{Support}
[100]	226,165
[110]	583,367

3.4 Overall Q for SiBAR and Comparison with Experimental Results

The preceding results can be combined using (7) to derive an overall estimate for the Q of the device in a particular mode. As there were large differences in [100] and [110] SiBARs for individual loss components, it can be expected that a similar trend should be observed in the overall Q. Indeed, measurements performed by our group [69] have shown this dependence. Table 10 compares the overall estimated Q with the results from [69]. As can be observed in the table, the estimates for Q are within a factor of 2 of the model, demonstrating good accuracy from a priori knowledge of the SiBAR's material and dimension. The main components dominating the Q are determined to be Akhieser dissipation and support loss. Support loss is most likely to be the main contributor to the discrepancy of Q between the different directions of silicon.

Table 10: Calculated values of Q for [100] and [110] directions of SCS of a SiBAR based on combination of the individual dissipation mechanisms explored in this chapter through (7).

Si Direction	$Q_{\text{estimated}}$	Q_{measured}
[100]	136,348	60-70,000
[110]	211,785	101,570

3.5 Impact of Small Angular Offsets from Desired Orientation

Also in [69], the impact of small angular offsets from the desired orientation to [100] or [110] crystal directions was studied. For angular offsets about [100], no discernable pattern of Q could be observed, but for the [110] direction, an offset as small as 0.1° brought the Q down by as much as 50%. As a first attempt at explaining this behavior, the prior models were modified to include the angular dependence in Akhieser dissipation, TED, and support loss. These results are summarized in Table 11. Based on these results, it seems that none of the identified dominant Q components varies significantly enough to account for the observed pattern in Q.

Table 11: Calculated values of various Q components for angular misalignments about the [110] direction of SCS of a SiBAR.

Angular Misalignment	Q_{AKE}	Q_{TED}	Q_{Support}
0°	349,711	7,700,038	583,367
±0.1°	349,702	7,700,022	583,364
±0.2°	349,677	7,699,971	583,352
±1°	348,860	7,698,343	580,104

3.6 Impact of Structural Imperfection on $Q_{Support}$

In this section, imperfections of the SiBAR are considered and compared with the perfectly-symmetric case investigated in earlier sections. It is presumed that the imperfections of the structure may lead to scattering through the support of the device, and support loss simulations confirm this assumption. One type of structural asymmetry is shown in Figure 22. The results for Q_{Support} from these simulations are shown in Table 12. As can be determined from this table, the [100] direction shows much less sensitivity (22% of 226,000) to structural asymmetry than the [110] direction, which dropped a drastic 64% of the initial Q of 583,000 for the 1 μm tether offset. This strongly suggests, but cannot fully confirm, that the results of [69] are likely due to structural asymmetries introduced as a consequence of the fabrication process (e.g., lithography errors or inability to produce perfect trenches on slightly rotated silicon).

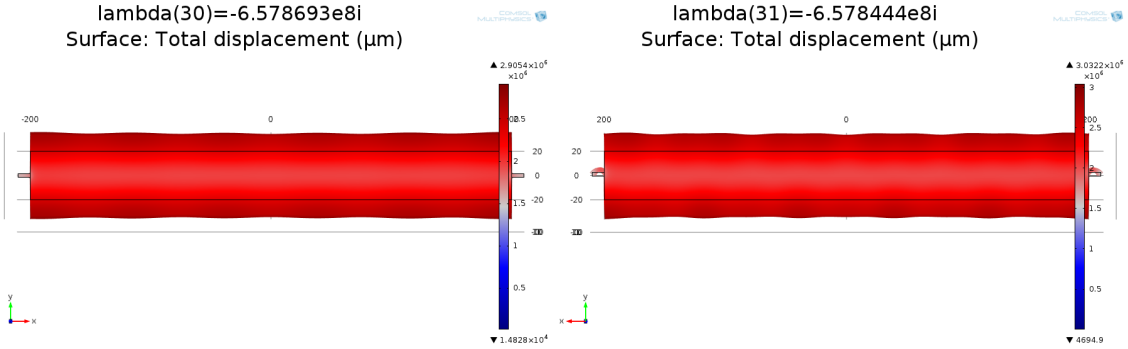

Figure 22: Comparison of (left) fully-symmetric SiBAR with its support tethers located on its central axis; (right) SiBAR with support tethers offset 1 μm away from its central axis.

Table 12: Results for Q_{Support} from simulations of Figure 22.

Si Direction	Q_{Support} Fully-symmetric	Q_{Support} 1 μm Offset
[100]	226,165	175,836
[110]	583,367	208,159

In addition to asymmetry of the structure, there can be imperfections such as the scalloping examined by TED earlier, which may contribute to extra Q_{Support}. The same model for the perfectly symmetric tether case above was used to explore the effect of scalloping on support loss. These models are shown in Figure 23. The results of this study are presented in Table 13. From these results, it can be deduced that the [110]-oriented SiBAR is much less sensitive to scalloping than the [100]-oriented SiBAR. This suggests higher interaction of the acoustic waves in the [100] SiBAR with its sidewalls, resulting in more energy leakage through the support, presumably as a result of the difference in Poisson's ratio discussed earlier.

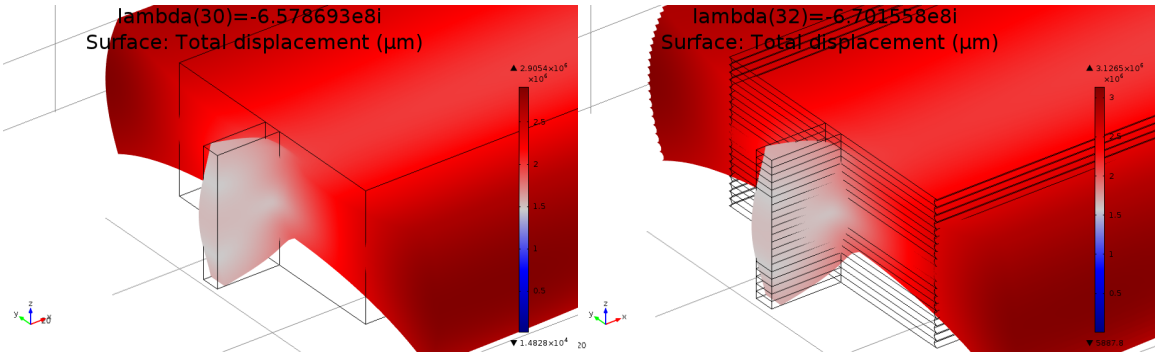

Figure 23: Comparison of (left) scallop free SiBAR with (right) SiBAR with 20 0.5 μm radius scallops along its thickness.

Table 13: Results for Q_{Support} from simulations of Figure 23.

Si Direction	Q_{Support} Fully-symmetric	Q_{Support} 1 μm Offset
[100]	226,165	41,193
[110]	583,367	534,380

3.7 Impact of AlN Layer in TPoS Resonators

A key process in fabricating TPoS Resonators is the deposition of an AlN or other piezoelectric material sandwiched between conductive metal layers. Figure 24 shows the growth of polycrystalline AlN in columnar grains. The orientation of these grains can be determined by XRD rocking curve measurements. Good quality AlN is oriented to the vertical axis with rocking curves on the order of 1°.

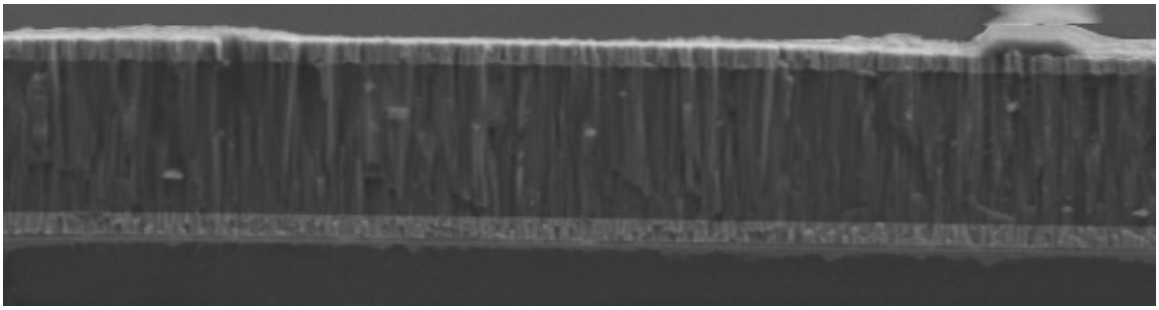

Figure 24: Growth of AlN in vertical columns of AlN crystallites. (Courtesy of Roozbeh Tabrizian)

Simulating the effect of the AlN layer is extremely difficult and requires detailed knowledge of the AlN microstructure. However, good headway can be made by considering an approximate model. The geometry for this model is depicted in Figure 25. On top of the silicon layer is an AlN layer composed of individual hexagonal crystallites. Initially, the assumption is made that each individual AlN crystallite is oriented along the thickness direction of the SiBAR. In this case, a Q_{BulkTED} value of 183,900 is simulated, contrasting sharply with the Q_{BulkTED} of 7.7 million for the plain SiBAR.

Next, the impact of misalignment of the crystalline grains is considered. As an example, if a worst-case 2.5° rocking curve distribution is assumed for the grain orientations, each individual crystallite can be assigned an orientation falling on this distribution at random. After carrying out the simulation (using the same model as the perfectly-aligned case to avoid numerical difficulty), the resulting Q_{BulkTED} came out to be 183,268. This is not initially alarming except that the size of the crystallite lattice parameter was 1 μm. Due to the difficulty in manually assigning random orientations to each crystallite (this can be

easily scripted if sufficient time is available), the effect of grain size can be extrapolated by assuming the dissipation is proportional to area. Table 14 summarizes these results. From this table, it is seen that additional TED due to the grains of AlN, in addition to the bulk effect of the AlN layer itself, can easily drop the Q from the 100,000 measured for a pure SiBAR to 10,000 or less for the TPoS device, which corresponds well with the difference in measured quality factors for TPoS devices vs. SiBARs (as will be demonstrated in the next chapter using LAB supports to suppress the support loss component).

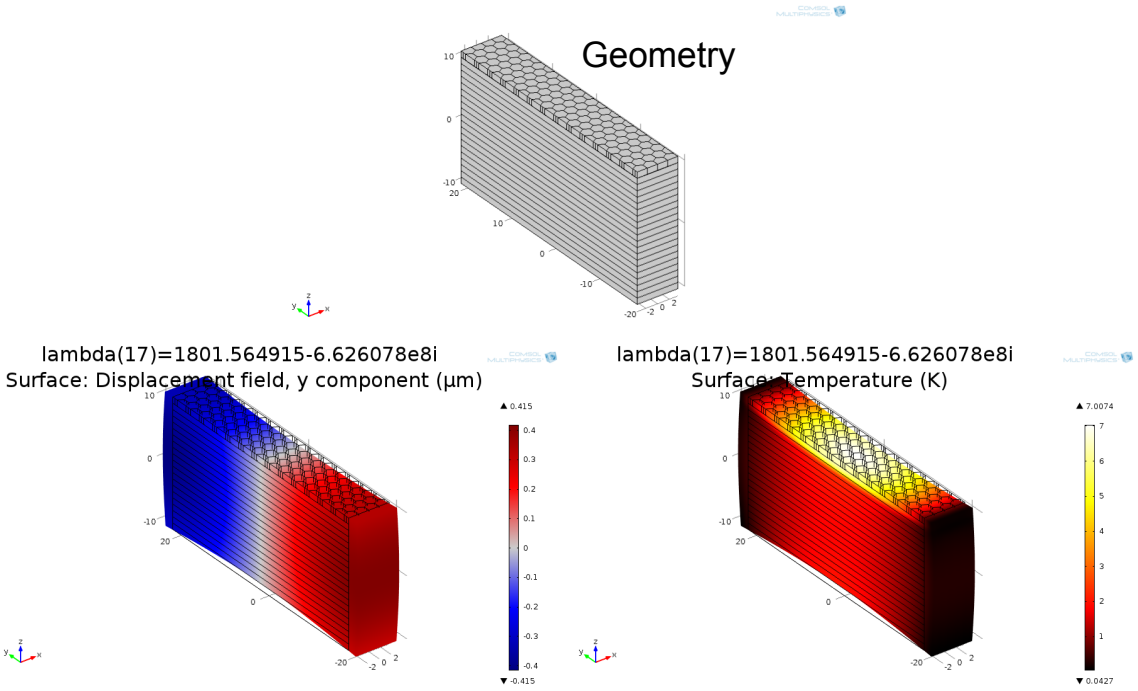

Figure 25: (top middle) AlN layer added on top of 100 MHz SiBAR showing individual grains with hexagonal lattice constant equal to 1 µm. (bottom left) Displacement of TPoS model in SiBAR mode. (bottom right) Corresponding temperature distribution showing that most temperature change is concentrated in the AlN layer. The corresponding Q_{BulkTED} is 183,900, down from 7.7 million for the silicon-only structure.

3.8 Summary of Dissipation in SiBAR and TPoS

This chapter applied the Q analysis framework to modeling the perceived main dissipation mechanisms for the Q of SiBAR and TPoS devices. Since a TPoS device is essentially a SiBAR with an additional piezoelectric layer on its surface, the SiBAR Q model applies to

Table 14: Q_{BulkTED} vs. AlN Grain Size for a 100 MHz TPoS SiBAR.

AlN lattice parameter (hexagonal)	Q_{BulkTED} (random orientation)
1 μm	183,268
100 nm	136,836
10 nm	5,196

the main body of the device and the piezoelectric layer can be accounted for as an additional source of dissipation. A number of surprising and interesting results have been obtained: first, TED doesn't appear to be limiting SiBARs up to 100 MHz while Akhieser and support loss seem to be the dominant dissipation mechanisms. Scalloping doesn't have significant effect in terms of TED, but can affect support loss by increasing the amount of scattering from the acoustic wave through the resonator supports for certain orientations of SiBARs. The base Q of a perfectly-symmetric SiBAR is not particularly sensitive to small rotations about the normal symmetry axes of silicon, but if the structure has a slight asymmetry, the support loss will increase rapidly. This is more pronounced for the [110] direction and agrees well with the experimental result of [69], suggesting [100] is a preferred orientation if Q stability is preferred (assuming scalloping can be sufficiently controlled). Finally, addition of the AlN layer to create a TPoS SiBAR resonator drops the base SiBAR Q from 7.7 million to 183,000. Scaling of the AlN grain size to experimental values and accounting for random orientations of the crystallites is expected to decrease this number even further.

CHAPTER IV

LINEAR ACOUSTIC BANDGAP (LAB) STRUCTURES

During the course of the preceding study on SiBAR and TPoS resonators, it became apparent that designing the resonator to suppress loss and enhance Q is extremely important. Toward this goal, linear acoustic bandgap (LAB) structures, a class of compact 1D micro-scale phononic crystal (PC) which can be directly integrated with micromechanical devices, were developed[1]. LAB structures are distinguished by small dimensions perpendicular to the line containing the 1D PC lattice. PCs can be used to manipulate the acoustic properties of materials. In the case of LAB structures, this manipulation arises from the formation of frequency stop bands, or bandgaps, which convert silicon from a material capable of supporting acoustic waves to a material which rejects acoustic propagation at frequencies in the bandgap (the acoustic waves become evanescent). PCs exhibiting acoustic stop-bands are of interest for their inherent frequency filtering characteristics. One- [100], [45] and two-dimensional [38, 54, 55, 59, 80] PCs have been used to create frequency bandgaps, but implementation of these structures typically requires a large area or multiple stacked layers. This work introduced AlN-on-Si and Si-only coupled-ring LAB structures, which can be implemented in minimal area without repeated stacking of material layers. The bandgap properties of the LAB structure are experimentally confirmed with single-device test structures. These LAB structures were successfully integrated as support elements of high-frequency AlN-on-Si resonators and demonstrate tangible Q and IL improvements. Converged finite element models also predict bandgaps in GHz frequencies wider than 10 MHz, allowing for scaling into higher frequencies. Finally, enablement of tuning ports

[1]This section is adapted from two conference papers: [83] and [82], with additions.

without harming the resonator's Q is demonstrated by using LABs to route the tuning signal.

4.1 Coupled-ring Linear Acoustic Bandgap (LAB) Structures

Recently, 1D PC structures derived by slicing a strip from a 2D PC plate have been demonstrated in simulation [34]. By generalizing the basis structure beyond strips cut from 2D PCs, the 1D PC concept can be extended. The design space is broadened such that only 1D periodicity is required and the PC basis can assume a variety of shapes and orientations. In this paradigm, 2D and 3D PCs can be considered specialized cases of the 1D PC with increasing dimensions of periodicity. A particular instance is the coupled-ring LAB structure depicted in Figure 26, for which the 3D basis is repeated at each lattice point with lattice constant a. Ring inner and outer radii (r_i , r_o), coupling beam width w, and layer thicknesses d_i parameterize the basis dimensions.

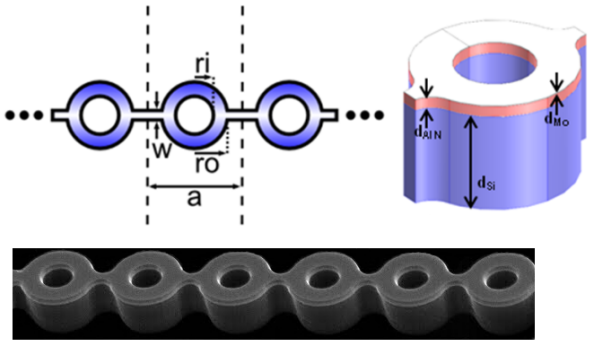

Figure 26: (top) Schematic and 3D view of coupled-ring LAB structure with AlN-on-Si stack (a = 20 μm, r_i = 4 μm, r_o = 8 μm, w = 2 μm, d_{Si} = 10 μm, d_{AlN} = 1 μm, d_{Mo} = 100 nm); (bot.) SEM of fabricated AlN-on-Si coupled-ring LAB structure.

4.2 Calculating LAB Dispersion Characteristic

The periodic nature of a PC combined with the mismatch between the basis structural material and the surrounding air or vacuum create acoustic bandgaps, or frequencies of no allowed acoustic propagation. To calculate the acoustic dispersion behavior of the coupled-ring LAB structures, modified eigenvalue analysis based on the Bloch relationship [80]

is performed. Wave vector contributions to the linear elastic equations are derived and implemented in COMSOL finite element software, beginning with the linear elastic force balance equation in the absence of externally applied force:

$$-\rho u_{i,tt} + \sigma_{ij,j} = 0, \tag{42}$$

where $\sigma_{ij,j}$ is the first derivative of the Cauchy stress tensor with respect to j^{th} component, $u_{i,tt}$ is the second derivative of displacement in the i^{th} direction with respect to time t, and ρ is the material density. Tensor quantities are expressed with Cartesian components, while a comma separates indices from derivatives, and the Einstein summation rule applies where appropriate. The Cauchy strain tensor ϵ_{kl} is related to σ_{ij} through the anisotropic Hooke's law,

$$\sigma_{ij} = c_{ijkl}\epsilon_{kl}, \tag{43}$$

where c_{ijkl} represents the fourth-order elastic stiffness tensor and ϵ_{kl} is defined as

$$\epsilon_{kl} = \frac{1}{2}\left(u_{k,l} + u_{l,k}\right). \tag{44}$$

In a 1D PC, the acoustic displacement wave must be of the Bloch-Floquet form to meet periodic boundary conditions:

$$u_i(x_m, k_n, t) = \tilde{u}_i(x_m)e^{i(k_x x - \omega t)}. \tag{45}$$

(43)-(45) are substituted into (42) and differentiated to establish a characteristic wave equation including the wave vector dependence:

$$\rho\omega^2\delta_{ik}\tilde{u}_k + \left(c_{ijkl}\tilde{u}_{k,l}\right)_{,j} + \left(ik_l c_{ijkl}\tilde{u}_k\right)_{,j} + ik_j c_{ijkl}\tilde{u}_{k,l} - k_j k_l c_{ijkl}\tilde{u}_k = 0 \tag{46}$$

(46) was implemented in the COMSOL model with customized code to unwrap crossing bands and automatically obtain the bandgaps. The resulting eigenfrequencies were mapped

to acoustic wavenumber k over the irreducible first Brillouin zone (BZ) of the 1D PC (Figure 27). In all cases, the finite element mesh density was refined until converged results were obtained.

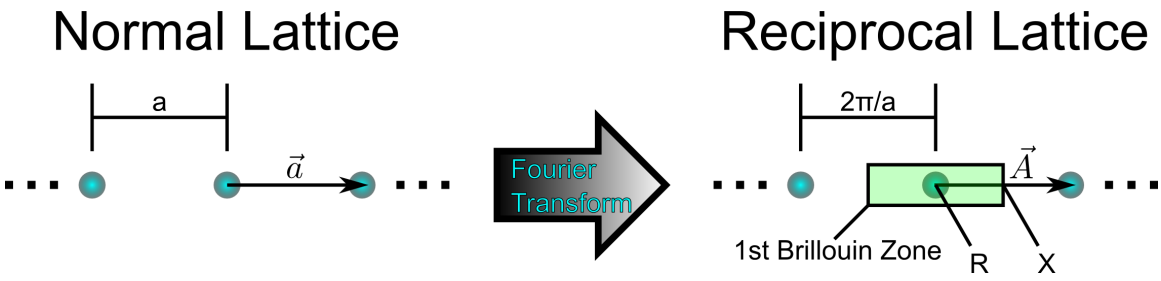

Figure 27: The 1D PC (lattice constant a) in normal space and reciprocal space (reciprocal lattice constant $2\pi/a$).

4.3 Dispersion Characteristic for AlN-on-Si and Si-only CR-LAB Structures

Acoustic dispersion curves using the dimensions given in Figure 26 are shown from 0-500 MHz for AlN-on-Si LAB rings and Si-only rings (Figure 28). These results indicate that the piezoelectric stack influences, but does not eliminate, the presence of bandgaps in the structure. By decreasing d_{Si} of Si-only coupled-ring structures to 1 μm, several complete bandgaps up to 1.97 GHz can be obtained (Figure 29). A bandgap of 12 MHz is predicted at 1.9 GHz, while a 22 MHz bandgap is obtained at 1.7 GHz, demonstrating the suitability of the LAB structure to ultra-high RF applications.

4.4 Experimental Determination of CR-LAB Bandgaps

Devices were fabricated on a silicon-on-insulator (SOI) substrate with 10 μm device layer thickness (d_{Si}) using a process similar to [80]. The piezoelectric stack consists of 100 nm Mo electrodes and 1 μm thick AlN. LAB structures were formed during patterning of the stack and device definition.

Specialized LAB test structures were developed to experimentally verify the bandgaps predicted in simulation. Claw-shaped AlN-on-Si transducers, which operate with a wide

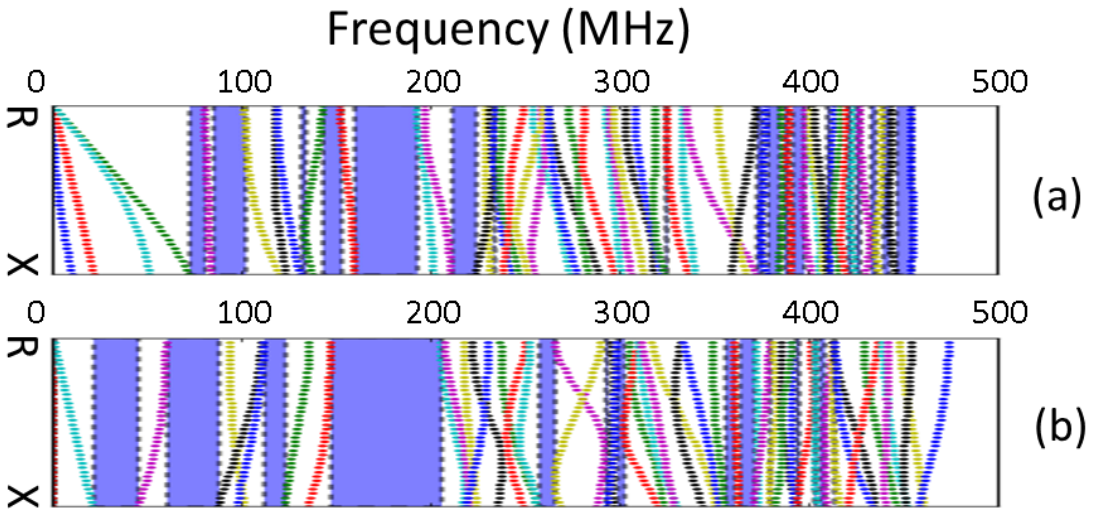

Figure 28: Acoustic dispersion curves with d_{Si} = 10 μm from 0-500 MHz for (a) AlN-on-Si LAB rings and (b) Si-only rings. Complete bandgaps are shaded in blue.

bandwidth up to 500 MHz, are connected through coupled-ring LAB structures (Figure 30). The transducers are designed to avoid any strong resonances over the band of operation.

Measurements, obtained with an Agilent E8364B vector network analyzer, were taken in air at room temperature unless otherwise noted with standard SOLT calibration. Transmission measurements of a six-period, Si-only LAB ring test structure with nine rows and corresponding reference are shown in Figure 31, confirming the predicted large complete bandgap from 160-205 MHz (Figure 28). Compared with the reference beams, transmission through the LAB structures is strongly suppressed below the noise floor. The experimental result is in good agreement with finite element predictions of the S_{21} frequency response (Figure 32). To reduce computation time of the frequency response simulation, the finite element simulation was performed in 3D for a test structure with one row of six coupled rings. Admittance parameters were obtained by applying appropriate electrical boundary conditions to the piezoelectric layer and converted to S-parameters assuming 50 Ohm terminations.

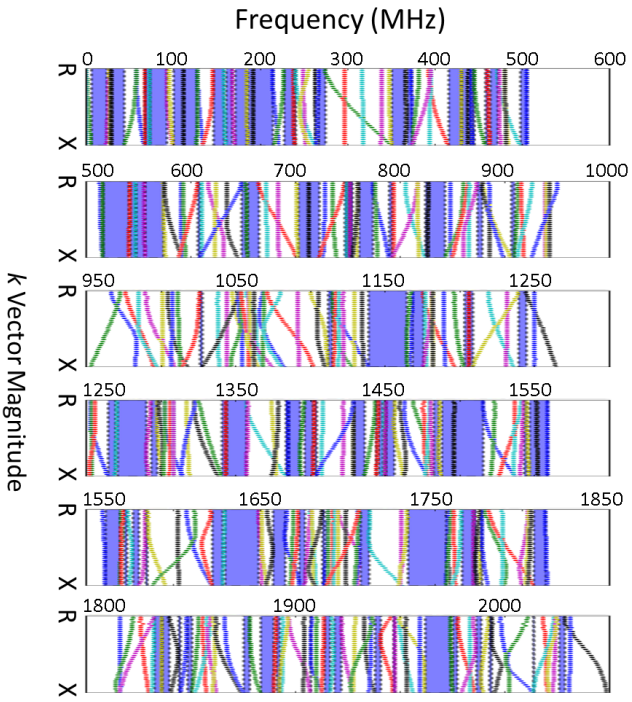

Figure 29: Acoustic dispersion curves from 0-2.05 GHz for Si-only rings, d_{Si} = 1 μm. Complete bandgaps shaded blue.

4.5 Enhancement of $Q_{Support}$ and IL by LAB Supports

LAB structures are good candidates to enhance the performance of high-frequency micromechanical resonators, which can be significantly affected by acoustic loss through support tethers. To demonstrate the effectiveness of the LAB structures, AlN-on-Si resonators were designed with six periods of coupled-ring supports. Identical devices with simple beam tethers, whose width equals w of the coupled-ring basis, are fabricated side-by-side

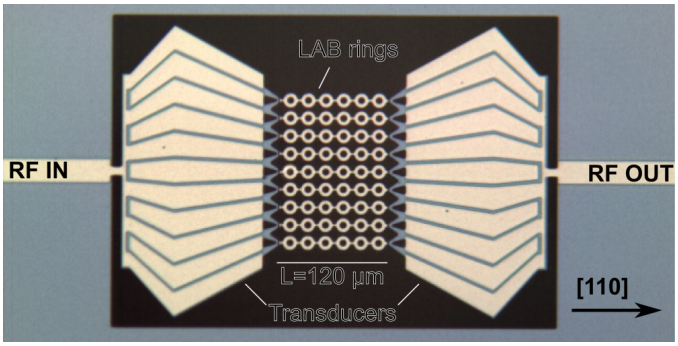

Figure 30: Optical micrograph of LAB acoustic transmission test structure.

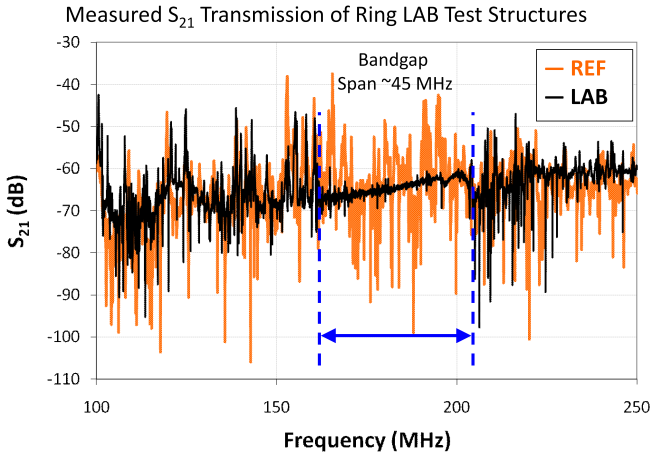

Figure 31: Measured S_{21} transmission response for Si-only LAB rings compared with equivalent reference beams.

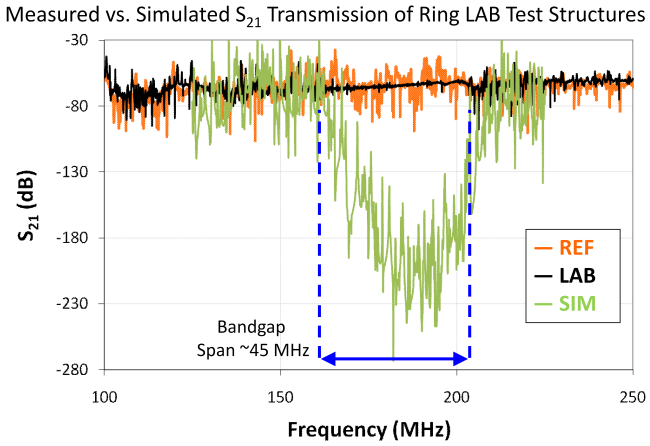

Figure 32: Measurements in Figure 31 with overlaid simulated S_{21} results.

with the LAB-enhanced devices for comparison.

Several examples of quality factor improvement in high-frequency resonators with AlN-on-Si LAB supports are given (Figures 33 and 35). To eliminate the effect of material property variations across the wafer, comparisons were made between adjacent devices.

Figure 34 shows the S_{21} response of a third-order LAB-enhanced lateral-extension-mode resonator at 213 MHz, which falls in the predicted bandgap from 210 to 223 MHz (Figure 28). This device demonstrates an 82% Q improvement and 4.9 dB IL improvement over an identical resonator with simple tethers. The simulated strain patterns suggest that

the LAB structures effectively block acoustic energy from coupling to the substrate.

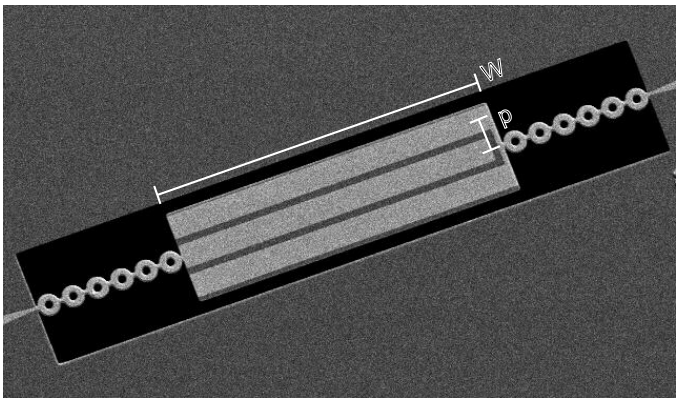

Figure 33: SEM of 3rd-order aluminum-nitride-on-silicon piezoelectric resonator (p = 20 μm, W = 220 μm) with integrated one-dimensional coupled-ring phononic crystal tether.

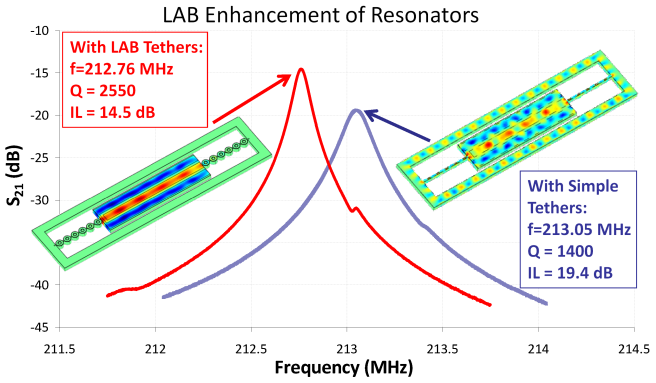

Figure 34: Measured S_{21} transmission and simulated strain patterns of same resonators with and without LAB tethers demonstrating 82% improvement in Q and 4.9 dB improvement in insertion loss (IL) as a result of suppression of acoustic loss through the support structure.

The 11th-order resonator with AlN-on-Si LAB supports (Figure 35) exhibits a low IL of 3.8 dB at 178 MHz, which is located in the large bandgap between 159 and 192 MHz (Figure 36). The same device has a Q of 11,400 at 603 MHz compared to the equivalent simple tether device Q of 7,200, suggesting existence of a bandgap at this frequency (Figure 37). The fQ_{unloaded} product is $7.24\text{x}10^{12}$, on par with or surpassing recently reported results for piezoelectric-on-silicon resonators [30, 44, 76]. The highest measured Q improvement for this design is from 1,450 to 1,930 (32%) with corresponding IL improvement of 2.17 dB at 178 MHz.

To verify repeatable improvements due to LAB tethers, adjacent pairs of several third-order designs were measured across multiple fabrication runs and across each wafer. An average Q improvement of 2x and average IL improvement of 30% are obtained (Figures 38 and 39). Due to the myriad variations possible with a 3D basis in a 1D PC, engineering of the bandgap to application requirements is possible, e.g., by choosing a different thickness. With these attractive attributes, the LAB structure shows potential to become a standard component of high-Q resonant MEMS designs.

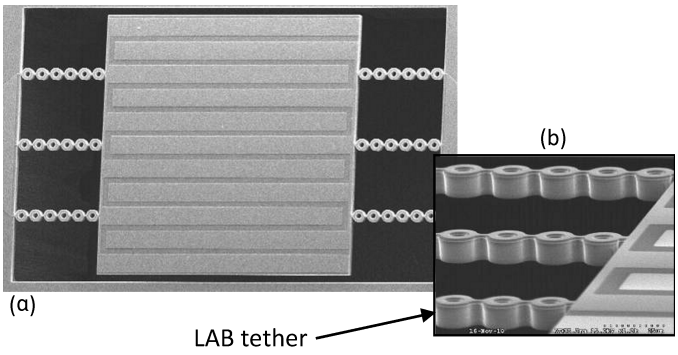

Figure 35: (a) SEM of 11th-order LAB resonator (p = 24 μm, w = 264 μm); (b) close-up of LAB coupled-ring tethers.

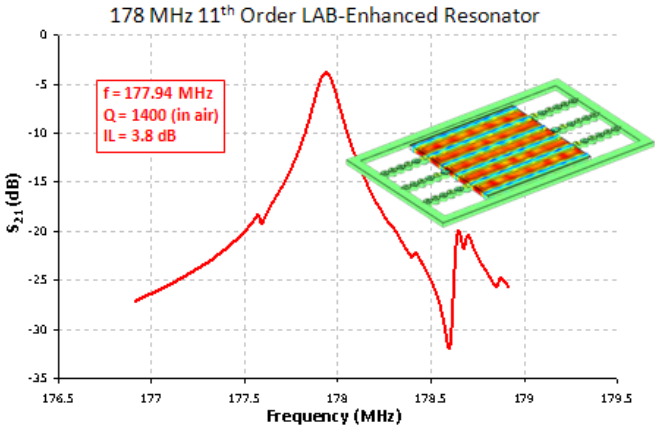

Figure 36: Measured S_{21} response for 11th-order AlN-on-Si resonators with (inset) length-extensional mode shape at 178 MHz.

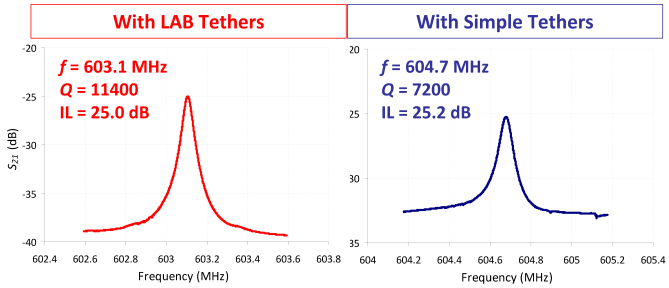

Figure 37: High-frequency mode of LAB-enhanced resonator (left) and high-frequency mode of reference resonator (right).

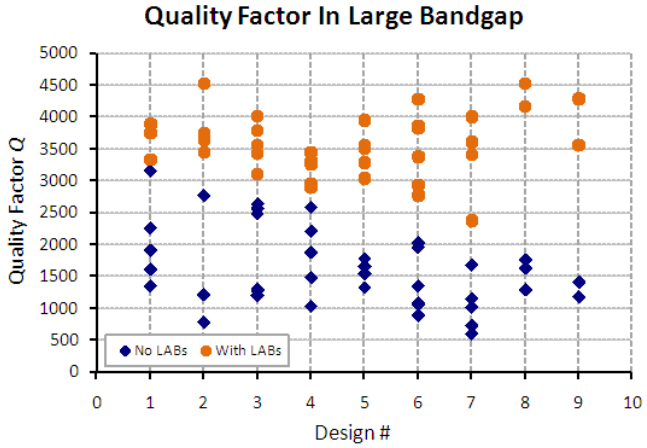

Figure 38: Q measurements of various LAB-enhanced designs and equivalent reference devices with third-order frequency located in the large bandgap between 159 and 192 MHz.

4.6 Spurious Mode Suppression by Mode Clamping with LABs

Next, a technique was investigated that utilizes arrays of coupled-ring linear acoustic bandgap (LAB) structures, which exhibit characteristic frequency stop bands, to reduce spurious modes in the wide-band response of AlN-on-Si lateral mode resonators. Aggressive LAB tethering (one support per finger) of high-order modes yields an increase in atmospheric quality factor (Q) from 1860 to 2890 for the designed peak at 209 MHz, compared to resonators with traditional tethers. Spurious modes from 0 to 360 MHz are suppressed by at least 30 dB relative to the main peak. The LAB structures presented achieve this goal through a combination of complete acoustic bandgaps and deaf bands. While piezoelectric MEMS resonators can be easily interfaced with low-power electronics, the appearance of

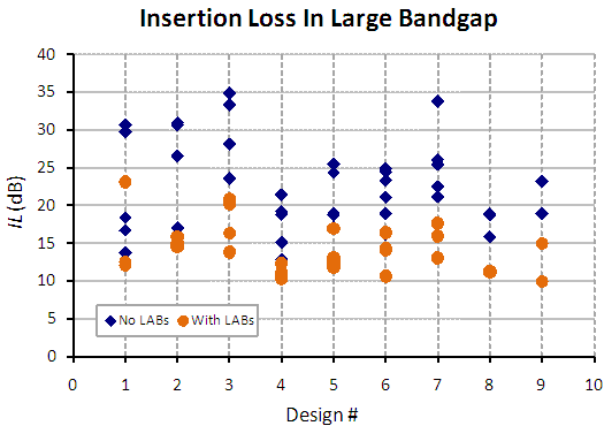

Figure 39: IL measurements of various LAB-enhanced designs and equivalent reference devices with third-order frequency located in the large bandgap between 159 and 192 MHz.

sufficiently strong low-Q spurious modes near the designed operation frequency can cause degraded oscillator performance. Oscillator phase and gain conditions may cause the spurious mode to become preferred over the desired mode during start-up, causing the oscillator to lock into the spurious mode. Additionally, feedthrough and coupling between the desired and the spurious modes can degrade phase noise performance and increase frequency instability, depending on the proximity of the spur [90].

Therefore, it is essential to eliminate wide-band spurious modes in piezoelectric micromechanical resonators for use in oscillators [5]. The linear acoustic bandgap (LAB) structures may be used to achieve this goal by creating support structures that utilize a combination of complete acoustic bandgaps [53] and deaf bands [33] to suppress the spurious modes without lowering the Q of the desired mode.

In addition to complete acoustic bandgaps, "deaf bands" [33] can also be found in the coupled-ring LAB structure dispersion characteristic. These bands demonstrate minimal coupling to the LAB structure when waves from the acoustic source exhibit orthogonal polarization to the mode of the LAB structure at the boundary between the two components. The mode shapes of two such deaf bands are depicted in Figure 40, where the acoustic

source is a longitudinal acoustic wave propagating orthogonally to the axis of the coupled-ring LAB structure. For these modes, displacement corresponding to the polarization of the longitudinal wave is effectively zero on the exposed faces of the coupling beam, meaning these bands of the LAB structure are deaf to the longitudinal waves propagating in this direction. Thus, LAB structures and integrated devices must be carefully designed to maximize the attenuation effects provided by complete acoustic bandgaps as well as deaf bands.

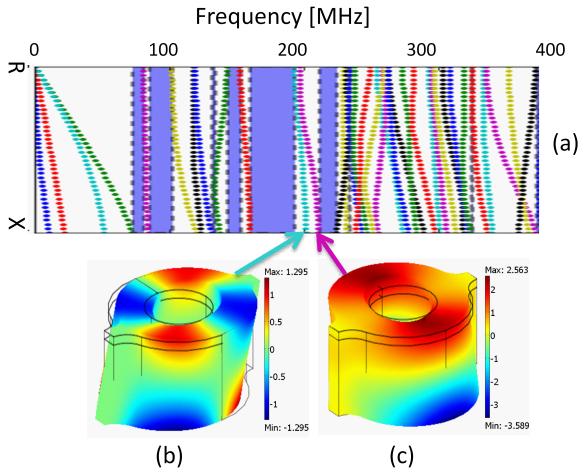

Figure 40: (a) Acoustic dispersion curve for AlN-on-Si coupled-ring linear acoustic bandgap (LAB) structure (bandgaps shaded blue); (b, c) mode shapes of indicated bands showing displacement polarization orthogonal to the axis of the LAB structure.

As seen above, LAB structures can serve as Q-enhancing support elements for MEMS resonators by tailoring bandgaps and deaf bands to confine acoustic energy within the device at the desired operation frequency. This confinement of energy enables an aggressive tethering approach using LAB structures, where one pair of tethers is used for each finger of the interdigitated transducer, to simultaneously improve the support loss component of Q (Q_{Support}) and provide significant attenuation of spurious modes which lie outside of the designed bandgaps.

The perfectly matched layer (PML) method was employed in COMSOL finite element software to study the effect of aggressive tethering on resonator support loss [15]. PMLs are

additional artificial domains attached to the device which absorb incoming acoustic waves and emulate loss of acoustic energy into the substrate surrounding the device. In this way, PMLs give an estimation of the theoretical lower bound on Q_{Support}.

Figure 41 shows the results of applying PMLs to an 11$^{\text{th}}$-order, 20 μm pitch, 220 μm wide AlN-on-Si resonator, comparing both traditional simple beam support tethers and six periods of coupled-ring LAB supports. For both designs, three pairs of support tethers are used to minimize the number of parallel acoustic leakage paths while maintaining sufficient structural support.

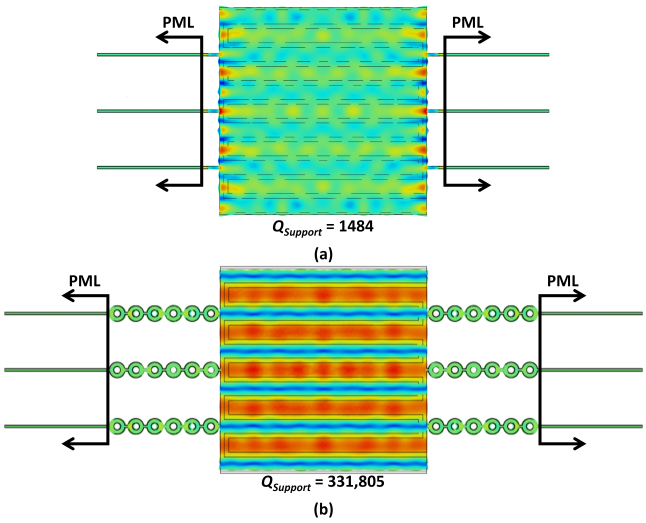

Figure 41: COMSOL PML simulation for a device with three support pairs; (a) simple tethers; (b) LAB tethers.

To avoid acoustic mismatch, the PML domains were created by extending the cross-section of the support tethers by a certain distance known as the PML length. In addition to this length, there are several parameters in the PML implementation of COMSOL which must be swept to obtain accurate values for the support loss. Additionally, a sufficiently fine mesh is needed to ensure convergence of the support loss value. Sweeping these parameters enables exploration of the PML design space to determine the lower bound of Q_{Support}. Because reflections and confinement of acoustic energy due to material mismatch are neglected in simulation, the PML result underestimates the value of Q_{Support} (i.e., the

values obtained from the PML method are lower than those obtained in reality).

With these considerations in mind, the Q_{Support} for the 11^{th}-order resonator with three pairs of simple tethers is estimated to be 1484 (Figure 41a), while a Q_{Support} of 331,805 is obtained for the same device with LAB tethers, showing over 200-fold improvement of support loss (Figure 41b). Note that the mode shape in Figure 41a shows deterioration, and a wave-like pattern develops along the supported edge of the resonator. Comparison of these results with other sets of PML parameters shows that as Q_{Support} is increased, the mode shape of the design in Figure 41a approaches that of Figure 41b, where the rippling along the supported edge is less apparent, suggesting that the support loss can have localized impact on the resonator mode shape.

Figure 42 studies a device that uses one pair of support tethers per finger of the interdigitated transducer structure. In addition to the PML method, periodic boundary conditions are employed to reduce the number of fingers to two. This effectively models an infinite order resonator and greatly reduces required computation time to calculate Q_{Support} (each support contributes a large number of elements). The high number of support tethers confines the mode more closely to the resonator body and nearly eliminates the waves along the supported edge. The confinement also reduces the number of possible resonance modes in the vicinity of the desired mode, which translates into higher Q_{Support}, even in the traditional tether case. Over 100-fold improvement is obtained in simulation by employing aggressive LAB tethers, boosting the estimated Q_{Support} from 21,723 to 2,489,724 (Figure 42).

A close-up SEM image of an aggressive LAB tether array is shown in Figure 43. SEM images of fabricated devices with simple tethers and LAB tether arrays are shown in Figures 44 and 45. The LAB-supported resonators have six periods per support tether. Because the LAB support array provides Q enhancement of insertion loss (IL), the width of the resonator body was decreased.

To quantify the impact of the LAB support array, the devices of Figures 44 and 45 were measured on a Cascade Microtech Summit 12000 M probe station at atmospheric pressure

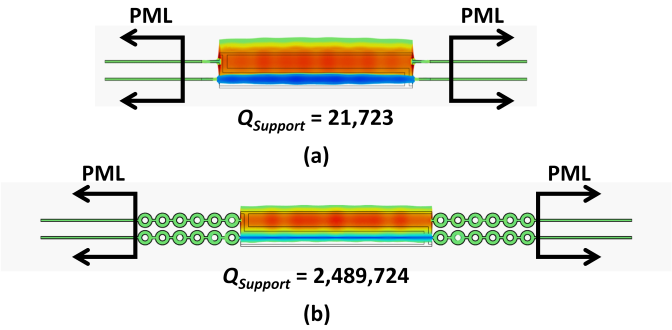

Figure 42: COMSOL PML simulation for an infinite order device; periodic boundary conditions are applied to the appropriate faces of the device to emulate infinite extent; (a) simple tethers; (b) LAB tethers.

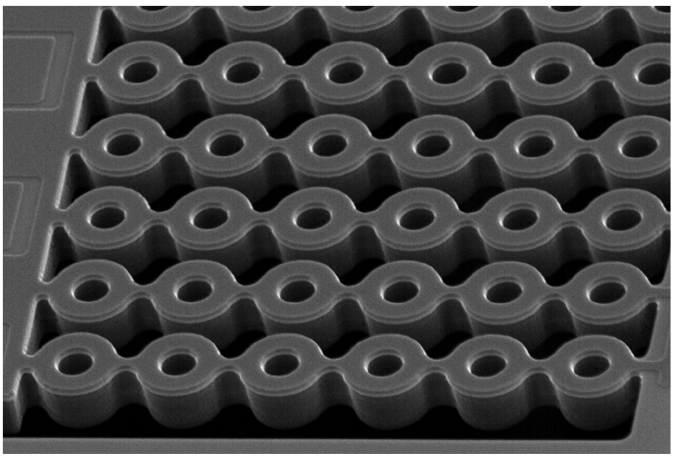

Figure 43: SEM image of fabricated LAB ring tether array.

and room temperature. The data were taken with an Agilent N5241a PNA-X network analyzer in two-port configuration.

A 1 GHz span was measured to observe the wide-spectrum response of both devices (Figure 46). All spurious modes below 360 MHz are suppressed by at least 30 dB relative to the desired mode, which lies near 209.5 MHz. A few spurs are amplified in the range 150-250 MHz as a result of acoustic confinement introduced by the LAB support array; however, they are not large enough to impact oscillator operation at the desired peak.

In addition to spurious mode suppression in the vicinity of the desired peak, at least 25 dB of suppression is obtained at higher frequencies between 360 MHz and 680 MHz. The cluster of spurious modes near 370 MHz is well-suppressed in IL compared to the reference

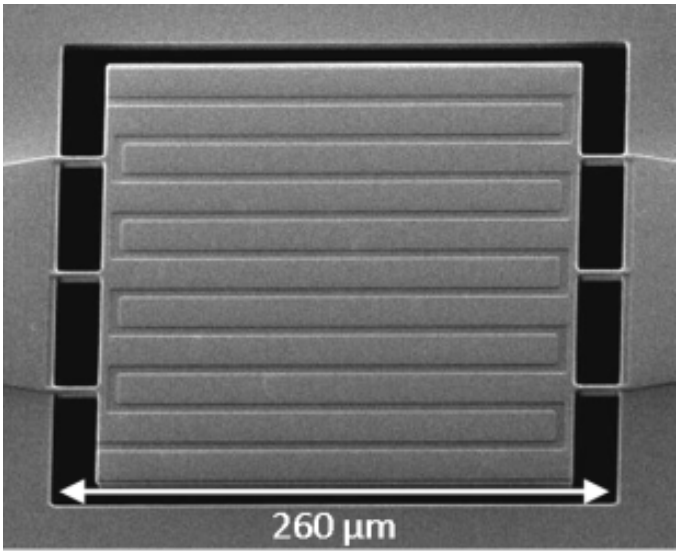

Figure 44: SEM image of 11th-order, 20 μm pitch AlN-on-Si resonator fabricated on 10 μm SOI wafers with 3 pairs of traditional beam supports (20 μ x 2 μm).

device. There is also an acoustically quiet section of the frequency spectrum from 380 MHz to 480 MHz in the LAB-supported resonator, when compared to several spurious modes in the reference response. A spurious mode is found at 680 MHz in the LAB-supported case. It is not clear if a relationship exists between this mode and the reference spurious modes in that vicinity; however, it may indicate a bandgap or deaf band introduced by LAB structures at that frequency.

Figure 47 shows a 50 MHz span centered about the desired mode. The LAB array has completely removed a spur on the high-frequency side of the reference device peak. Underlying modes are boosted by the LAB tethers but remain near the noise floor and will have minimal effect on oscillator performance. Finally, Figure 48 gives a narrow-span (2 MHz) measurement of the main peaks for both reference and LAB array devices. The LAB array is found to improve the device Q by almost 60% from 1860 to 2890.

Comparison of the measured Q value with the Q_{Support} value predicted by COMSOL finite element PML simulations for the simple tether case (Figure 48 vs. Figure 41a) yields the conclusion that support loss simulations are accurate to about 20%. However, this particular case ignores reflections back into the resonator body from material and geometry

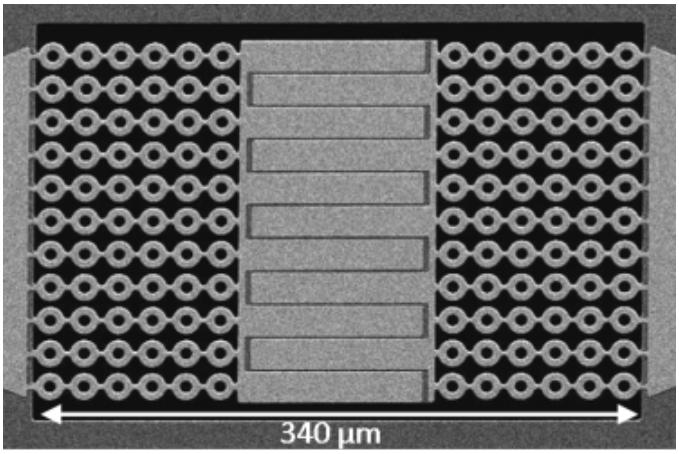

Figure 45: SEM images of 11[th]-order, 20 µm pitch AlN-on-Si resonators fabricated on 10 µm SOI wafers: 11 pairs of 6 period coupled-ring LAB supports.

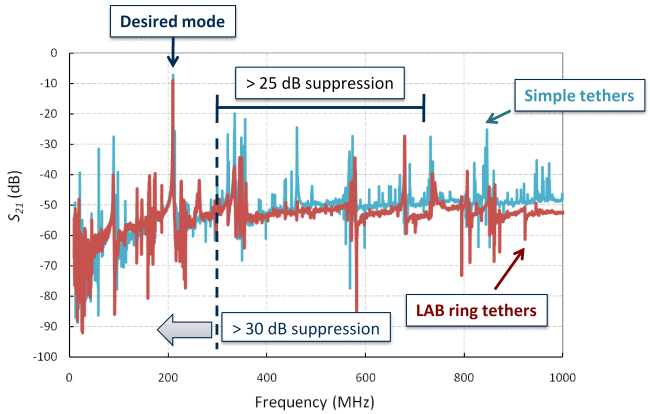

Figure 46: Measured S_{21} response showing wide-band spurious suppression. Below 360 MHz, spurious modes are suppressed at least 30 dB relative to the desired mode. Between 360 MHz and 680 MHz, spurious modes are suppressed at least 25 dB.

mismatches in the support structure. In that context, COMSOL PML simulations predict the lower bound of the Q value, which is accurate for support loss limited resonators.

However, the predicted Q_{Support} for the LAB-enhanced resonator was in the millions, whereas the measured value was still limited to a few thousand (Figure 48 vs. Figure 42b). In high-order piezoelectric MEMS resonators, a large component of the dissipation can be attributed to the piezoelectric transduction stack [9]. LAB array supports nearly eliminate support loss, which causes other factors to become dominant in the expression of the overall

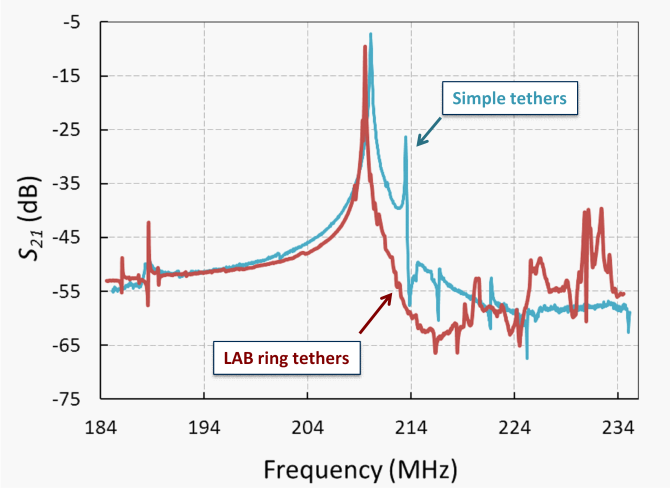

Figure 47: Medium-span (50 MHz) response for both devices at 210 MHz.

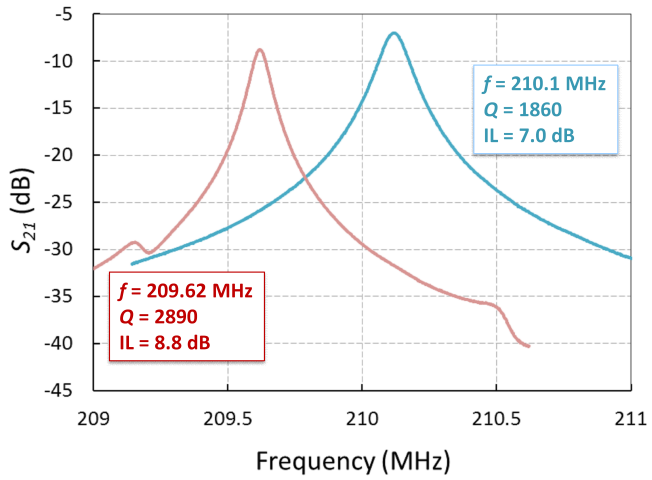

Figure 48: Narrow-span (2 MHz) response for both devices at 210 MHz.

Q:

$$Q = \left[\frac{1}{Q_{\text{Support}}} + \frac{1}{Q_{\text{Other}}} \right]^{-1} \tag{47}$$

Finally, the enhanced Q of the LAB supported device also improves the device IL, enabling a reduced transduction area for similar levels of IL. Thus, LAB structures can be incorporated into MEMS resonators without significantly increasing device area. Aggressive tethering of MEMS resonators with LAB arrays can control and suppress spurious

modes which negatively impact MEMS oscillator performance. The PML method was employed to predict the lower bound of support loss contribution to overall resonator Q, and demonstrated that this approach agrees well with measured experimental values when the resonator is support-loss limited.

4.7 Scaling of LAB Structures

In section 4.3, the thickness of the nominal CR-LAB design was scaled and it was predicted to show bandgaps in the GHz range without scaling the lateral dimensions. This is because thickness-dependent modes get pushed to higher frequencies, opening windows in the dispersion characteristic where no propagating mode exists. If this approach were followed, bandgaps could be generated at GHz frequencies without resorting to extreme lithography measures. However, no thin silicon runs were available at the time of writing and the silicon thickness approaches the thickness of the AlN layer, suggesting AlN will have a greater impact when determining the dispersion characteristics. Instead, to verify scaling of the frequency bandgaps, a 20 μm-thick silicon run of TPoS was available. Since the thickness is increases by twice, in order to guarantee existence of a bandgap, the lateral dimensions were also increased by a factor of two. Figure 49 shows the result of simulating a SiBAR resonator (W = 48 μm) with 3 periods of 2X-scale LAB support rings. From the frequencies of the trapped modes in the resonator, the bandgap can be extracted as 81.9 MHz to 102.6 MHz, in good agreement with scaling the dispersion curves in the bottom of Figure 28. The main resonance mode of the SiBAR is found at 87.9 MHz, which should be far enough from the edge of the bandgap that good support loss suppression can be achieved.

Figure 50 shows the effect of modifying the number of LAB unit cells for the main resonance mode at 88 MHz. Table 15 tabulates the Q_{Support} of these devices, as well as compares with a similar SiBAR with modified width (W = 40 μm) which has its main resonance located near the edge of the bandgap at 106 MHz. These values were calculated

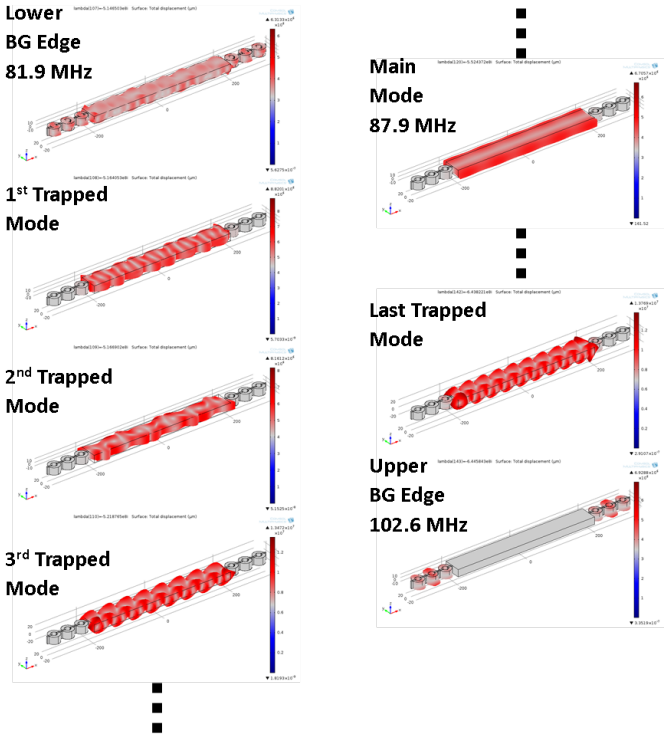

Figure 49: Simulations of a 2X-scale LAB-enhanced 3rd-order SiBAR resonator with 3 support rings. Based on the trapped modes in the resonator (indicated by evanescent decay of vibration in the LAB structure), the scaled bandgap can be expected to exist between 81.9 MHz and 102.6 MHz, in good agreement with the scaled dispersion curve of Figure 28.

using the acoustic S-parameter method rather than PMLs. Based on this table, for a SiBAR resonance located in the bandgap, each additional unit cell of the LAB tether corresponds to a 100-fold improvement in Q_{Support}, suggesting evanescent (exponential) decay of the vibration due to the LAB support, consistent with the theory of non-propagating waves. At the edge of the bandgap, inconsistent results are obtained, with Q_{support} varying from 7,700 to 3.1 million and back to 240,000 with each additional LAB unit cell. This suggests that LABs can enhance Q_{support} even outside the bandgap, but more care needs to be taken as there may exist a "quasi-deaf" band which can interact with the SiBAR in different ways depending on the number of LAB unit cells. For stability of Q_{Support}, it is recommended to design LAB tethers which are centered on the desired mode of resonance. It is also interesting to note that adding scallops to the sidewalls as was done previously for SiBAR

resonators did not have a major effect on Q_{Support} for the 3 unit cell LAB-enhanced SiBAR. This suggests that surface scattering can be mitigated in BAW resonators by trapping the acoustic energy inside the resonator such that it is eventually returned to the original mode of the device.

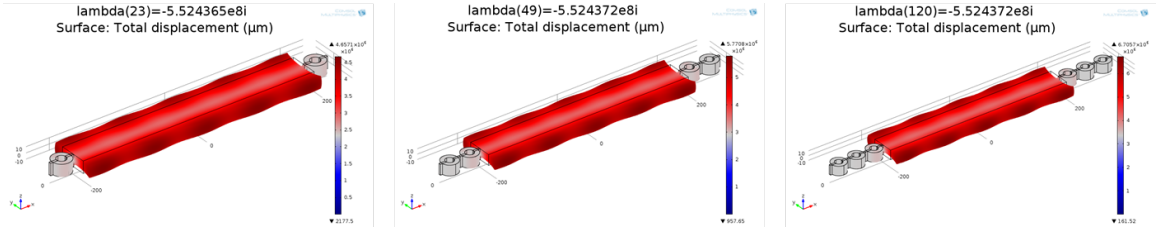

Figure 50: Effect of modifying number of unit cells on LAB-enhanced SiBAR resonator.

Table 15: Q_{Support} for two different width SiBARs with varying number of LAB unit cells in the support tethers.

Num. LAB Unit Cells	Q_{Support} (in BG) W = 48 µm	Q_{Support} (edge of BG) W = 40 µm
1	2.62 million	7,700
2	169.2 million	3.1 million
3	10.2 billion	240,000
3 (w/ scallop)	8.4 billion	-

4.7.1 Experimental Confirmation of 2X Bandgap Scaling

Figure 51 shows SEM and optical views of a redesigned test structure based on the well-known acoustic horn concept. This test structure operates similarly to that shown in Figure 30 and is expected to respond to a wide bandwidth of signals. Figure 52 shows measurement results from this and similar test structures with varying number of LAB unit cells between the transducers. With these structures, the bandgap is clearly observed as supression of transmission in the expected frequency range compared with a reference structure, as indicated on the plots. With only one LAB unit cell, a 15 MHz bandgap was measured. However, for two or more LAB unit cells, the bandgap remained constant at 25 MHz, suggesting that the slope of the bandgap edge is very sharp in these latter cases.

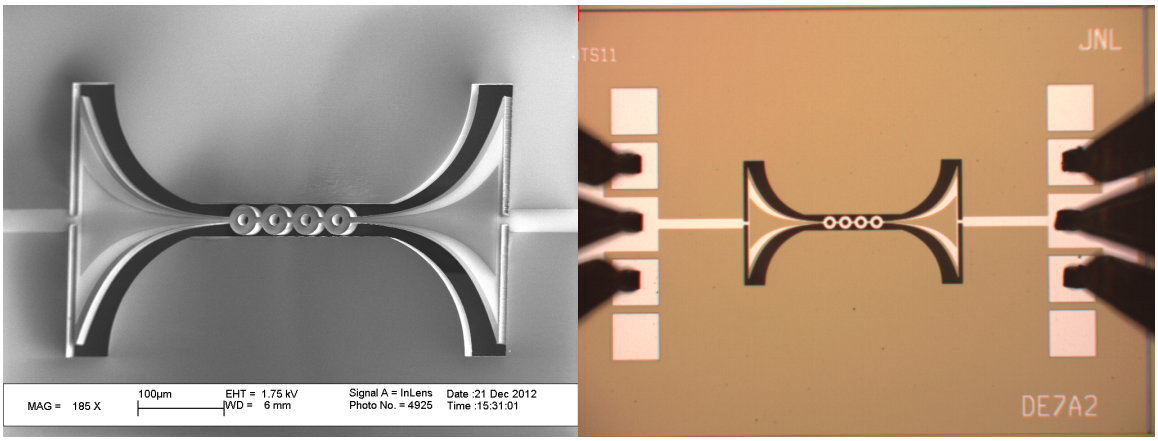

Figure 51: SEM and optical views of a redesigned test structure based on the acoustic horn concept for experimental characterization of acoustic bandgaps in the same vein as Figure 30.

It is also important to verify that the Q_{Support} enhancement for resonators remains after scaling the bandgaps. Figure 53 shows a reference TPoS device with center frequency of 88 MHz, while Figure 54 shows the LAB-enhanced version of the resonator with a 4 unit cell LAB tether. In the reference case, a Q_{unloaded} of 4806 was obtained at an IL of 8.4 dB, while the LAB-enhanced device improved the Q_{unloaded} to 8980 and the IL to 5.8 dB. If the Q_{Support} is assumed to be fully removed by the LAB tethers, then the original Q_{Support} for the reference device can be calculated as 10,340. Hence, the Q_{Support} of the LAB-enhanced devices can be expected to be well above 10,000. This result can be used to calibrate the support loss simulations by providing a known range for Q_{Support} in the reference device case.

4.8 LAB Enablement of Frequency Tuning and Trimming

Based on the preceding results of this chapter, LAB-supported resonators can have very large Q_{Support}, effectively eliminating support loss such that Akhieser dissipation (in SiBARs) and TED (in AlN TPoS resonators) will dominate the actual Qs of the device. As was seen in the case of aggressive tethering, many tethers can be attached to the device without affecting the Q, in lieu of the traditional approach of minimizing the number

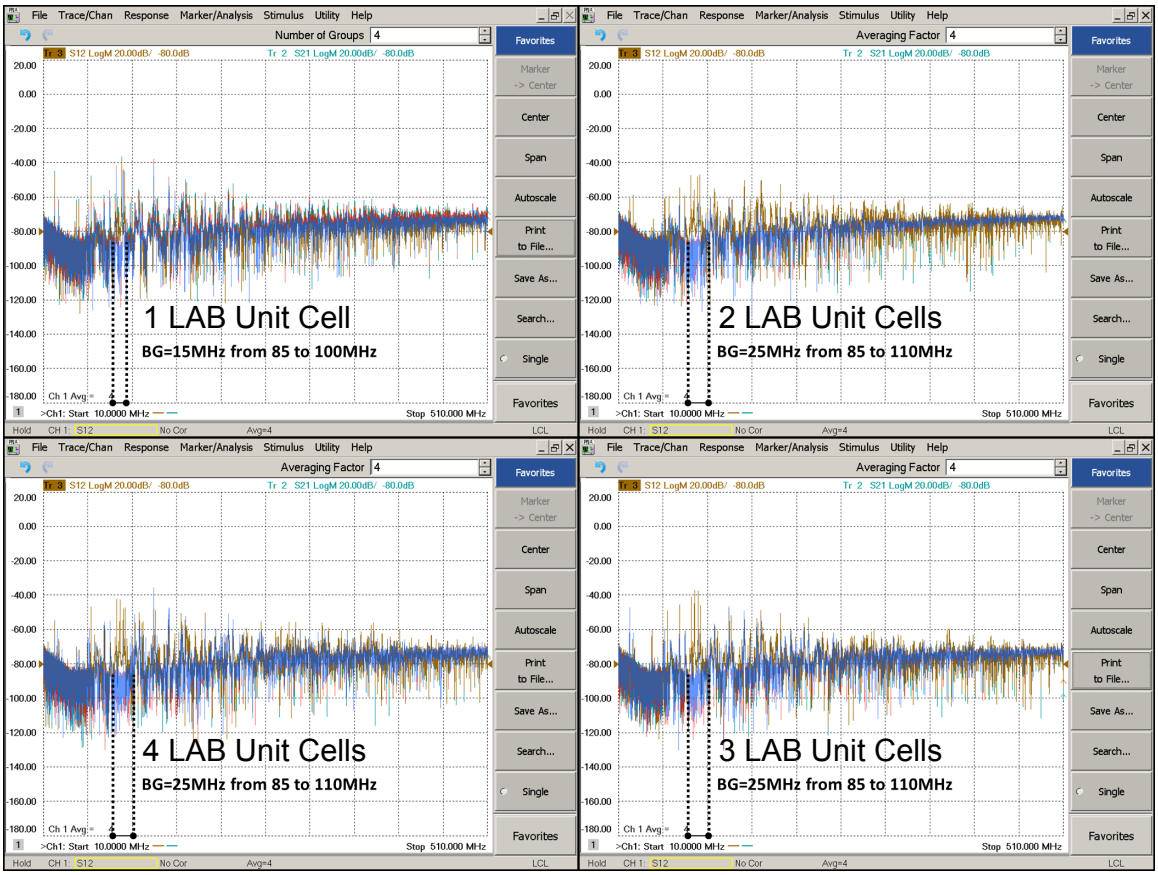

Figure 52: Measured results from test structures similar to that shown in Figure 51 with varying number of LAB unit cells (1 to 4, clockwise from top left).

of support tethers. In the preceding cases, the additional tethers were used to maximize the transduction area in a 2-port resonator configuration. However, it is not necessary to restrict LAB tethers to the task of routing in the RF signals. They can also route DC or other electrical signals, which suggests the possibility of using an array of LAB tethers for both transduction and tuning. Figure 55 shows a device in which 3 ports have been created by routing the Mo traces on the outer AlN covering the support substrate. This approach allows great flexibility in routing signals since the traces outside the resonator can occupy larger area than if they were routed on the resonator itself. Two of the ports are used for normal 2-port S-parameter measurement, while the 3rd port is used for adjusting the piezoelectric termination. Due to the piezoelectric stiffening effect, opening or shorting

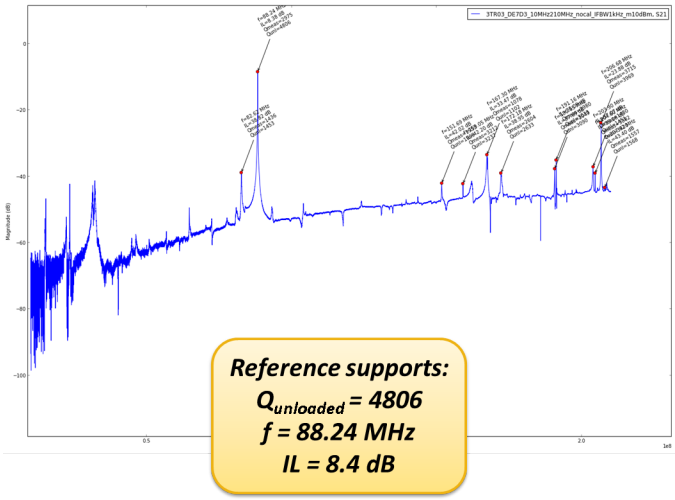

Figure 53: A reference TPoS device centered in the scaled bandgap.

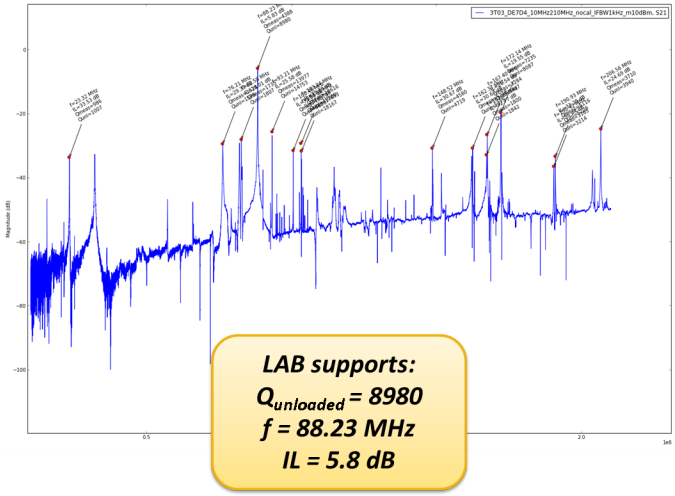

Figure 54: A LAB-enhanced TPoS device centered in the scaled bandgap.

the piezoelectric layer adjusts the stiffness of the film, which modifies the resonance frequency of the device. Figure 56 illustrates this concept for the device shown in Figure 55. For this particular configuration, 600 Hz tuning was achieved at 104.7821 MHz, which is sufficient for fine control of a temperature-compensated oscillator. Further, the Q remained at 5000 or above for the entire tuning range, while the IL was kept below 14 dB. Equivalent reference devices had Qs less than 3000 and ILs greater than 17 dB. It is expected that the resonator design can be optimized for larger tuning range with LAB-enabled tuning, depending on the needs of the application. Finally, since the tuning is controlled by the

piezoelectric termination, this technique is compatible with laser trimming of a Pt resistor in the case that permanent change to the resonance frequency is desired.

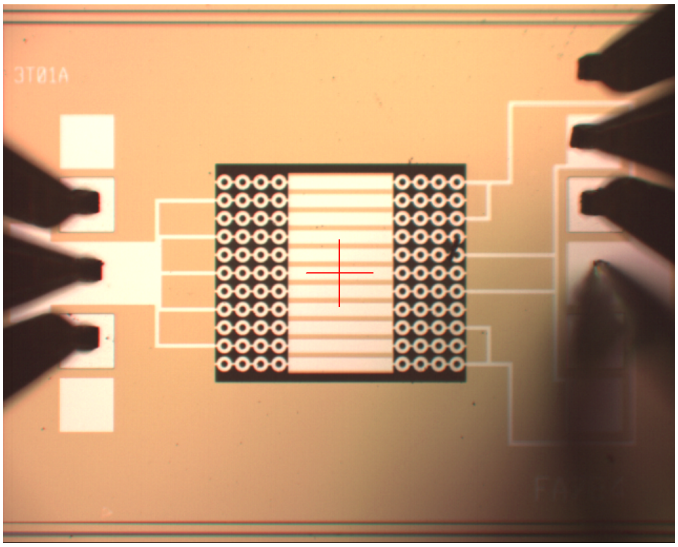

Figure 55: Optical view of probe placement for 3 port tuning experiment. GSG probes are used for RF ports, while a DC probe was used to adjust the piezoelectric termination of the tuning port.

4.9 Summary of LAB Structures

The LAB structures developed in this work demonstrated acoustic bandgaps over a certain range of frequencies. These bandgaps were designed and experimentally verified by special test structures. Using them as support elements was shown to increase Q by almost 2X. Further, the bandgap frequencies could be scaled by changing the parameters of the unit cell, and LABs were shown to enable tuning of multi-port TPoS resonators.

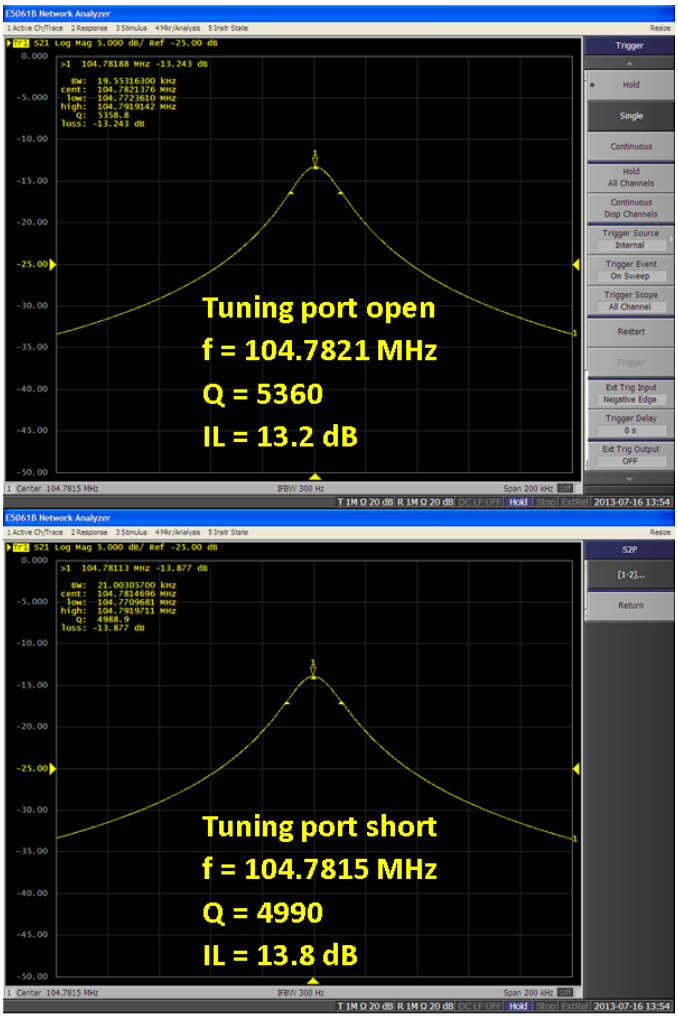

Figure 56: Measured tuning results showing 600 Hz tuning range at 104.7821 MHz by opening or shorting the tuning port. IL and Q change only slightly (6% for Q), suggesting some resistive heating is introduced through the shorted piezoelectric tuning port. Similar reference devices have initial Q factors less than 3000.

CHAPTER V

3D MICRO-HEMISPHERICAL SHELL RESONATORS (μHSRS)

> The practical limit in size reduction is probably reached when the shell thickness for the desirable operating frequency becomes unacceptably small. — Dr. David Lynch in 2001 on scaling Northrop Grumman's Hemispherical Resonator Gyro (HRG) to tenths of millimeters in thickness

As the above quote demonstrates, the ability to fabricate 3D μHSRs, a MEMS device inspired by the well-known macroscale HRG [67], with shell thicknesses on the order of microns is a completely novel development in the past couple years. Prior to undertaking this task at Georgia Tech, it was not even known if microshells could be robust enough to support themselves, let alone be subjected to vibration. However, this has become a reality and free-standing shells with thicknesses in the range of a few micron to hundreds of nanometers have been successfully fabricated and operated in their resonance modes. Interest in axisymmetric 3D micromachined shell resonators, with applications including rotation and other sensors, is growing due to their potential for high quality factor (Q) at low frequencies and high insensitivity to environmental vibrations, packaging stresses, and thermal gradients [14, 16, 65, 73–75, 77, 84, 85, 102]. Acting as a gyroscope, the principal axes of vibration of a micro-hemispherical shell resonator (μHSR, such as that shown in Figure 57) precess due to Coriolis forces when the device experiences external rotation [67]. This precession occurs as a result of energy transfer between degenerate vibration modes of the shell. To pick off the angle of rotation with the highest accuracy, it is important that the amplitudes of the degenerate modes decay at equal rates in free oscillation, so that damping errors do not result in angle errors on readout [79]. In addition, to increase the overall free-oscillation decay time ($\tau = 2Q/\omega$), the energy dissipation and angular frequency ω should

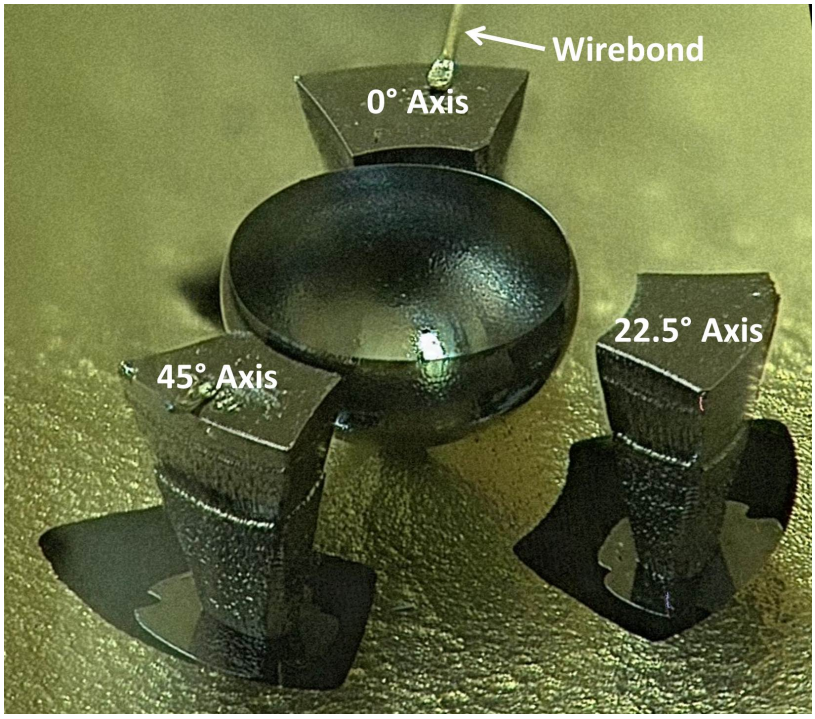

Figure 57: Optical micrograph [85] of a 1240 μm diameter, 2 μm thick ALD TiN-coated thermally-grown oxide micro-hemispherical shell resonator (μHSR) assembled with multi-axis silicon electrode pillars for capacitive testing created using the process detailed in [77].

be minimized. To reach these goals in a minimal volume, the thickness of the resonator shell must be reduced to sub-micron levels, which results in very high aspect ratio shells compared with their macroscale equivalents [52, 67]. Therefore, understanding the origins and effects of energy dissipation is critical to achieve high-performance μHSRs.

Although many sources of dissipation exist in μHSRs, at this early stage of development, efforts must be directed toward identifying practical sources of dissipation and on understanding those that set the fundamental limits of Q. Dissipations may be categorized into those that occur inside the material (bulk losses), and those that occur in the vicinity of the shell's surfaces (surface losses). Key bulk losses include those that originate from the imperfections in the quality of the material (e.g., polycrystalline grains, defects, voids) and thermoelastic dissipation (TED) [86, 97–99], while surface losses may include carbonaceous contamination [61], water penetration [20], surface scattering, loss due to a damage layer which extends a characteristic depth into the bulk of the material [23], and surface

TED which originates with the homogeneity of strain due to roughness of the shell's surface. In the case of water penetration in thin shells, this may become a bulk dissipation effect if water diffuses through the entire thickness of the shell. In addition, the resulting Q may be loaded by other factors, such as coating materials, anchor loss, air damping, and electrical impedance mismatch [9]. Although any of the preceding dissipation sources may play important roles, TED is the focus of this chapter since it is an omnipresent and fundamental phenomenon which bears concern for most practical vibrating bodies. Further, little attention has been paid in literature to surface TED as a potential dominant surface loss mechanism. It is therefore important to develop models to account for surface TED, which may then serve as an analogy for the study of other surface dissipation effects. Due to the novelty of μHSRs, a slight detour is motivated to revisit their operation principles and vibration modes and frequencies prior to examining their dissipation and quality factor.

5.1 Vibration Modes and Frequencies of μHSRs

For many applications of μHSRs, the lowest frequency inextensional modes [66] form the modes of interest. Following the spherical coordinate system shown in the top of Figure 58, the inextensional modes are degenerate in the circumferential, or θ, direction in an ideal μHSR, and exhibit $\cos(m\theta)$ and $\sin(m\theta)$ dependency, respectively, where m is the integer order of the mode. The higher-order modes along the polar (φ) direction are typically neglected since they will occur at higher frequencies, minimizing their usefulness in capacitively-transduced resonators. Simulated displacement patterns of the first few of these modes ($m = 2$ and $m = 3$) are shown in the middle row of Figure 58 and the corresponding mode pattern at the shell rim is depicted in the bottom row of Figure 58. The undeformed contour of the rim is shown with a dashed line, while each degenerate mode (corresponding to either $\cos(m\theta)$ or $\sin(m\theta)$) is colored blue and red, respectively. As can be deduced from Figure 58, each m mode has $2m$ nodes and $2m$ antinodes. Furthermore, the angular split between the degenerate mode pairs is $90°/m$. The angular frequency of the m^{th}

mode (ω_m) of a constant thickness hemispherical shell can be approximated in Rayleigh's inextensional theory by [21, 49, 66, 85]

$$\omega_m = \sqrt{\frac{2}{3}} m\left(m^2 - 1\right) \sqrt{K_m} \sqrt{\frac{E}{2\,(1+\nu)\,\rho}} \frac{h}{R^2}, \tag{48}$$

where K_m is a mode-dependent constant determined by

$$K_m = \frac{\int_0^{\varphi_f} \tan^{2m}\left(\frac{\varphi}{2}\right) / \sin^3\varphi d\varphi}{\int_0^{\varphi_f} \left(m^2 + 1 + \sin^2\varphi + 2m\cos\varphi\right) \sin\varphi \tan^{2m}\left(\frac{\varphi}{2}\right) d\varphi} \tag{49}$$

and E, ν, and ρ are the Young's modulus, the Poisson's ratio, and the mass density of the material, respectively. The geometric parameters are the shell thickness, h, and the mid-shell radius, R. φ_f indicates the extent of the polar angle, which terminates at the rim of the shell. For this work, φ_f is always assumed to be $\pi/2$ (a true hemisphere).

5.2 Steady-State Thermoelastic Equation of Motion for Thin Hemispherical Shell of Isotropic Material

In the case of a thin hemispherical shell of homogeneous isotropic material, by analogy to a thin plate, the stresses in the r direction can be assumed negligible, resulting in a 2D solution domain for the displacements over (φ, θ). The mid-shell surface ($r = R$) is taken as the reference surface. When it is necessary to consider the thickness direction of the shell, as in the calculation of strain, the radial offset coordinate $z = r - R$ from the mid-shell surface is employed. Hence, the stresses and strains on the mid-surface of the shell are subject to the constitutive relations

$$\begin{Bmatrix} \sigma_{\varphi\varphi} \\ \sigma_{\theta\theta} \\ \sigma_{\varphi\theta} \end{Bmatrix} = \frac{E}{(1+\nu)(1-2\nu)} \begin{bmatrix} 1-\nu & \nu & \\ \nu & 1-\nu & \\ & & 1-2\nu \end{bmatrix} \begin{Bmatrix} \epsilon_{\varphi\varphi} \\ \epsilon_{\theta\theta} \\ \epsilon_{\varphi\theta} \end{Bmatrix}, \tag{50}$$

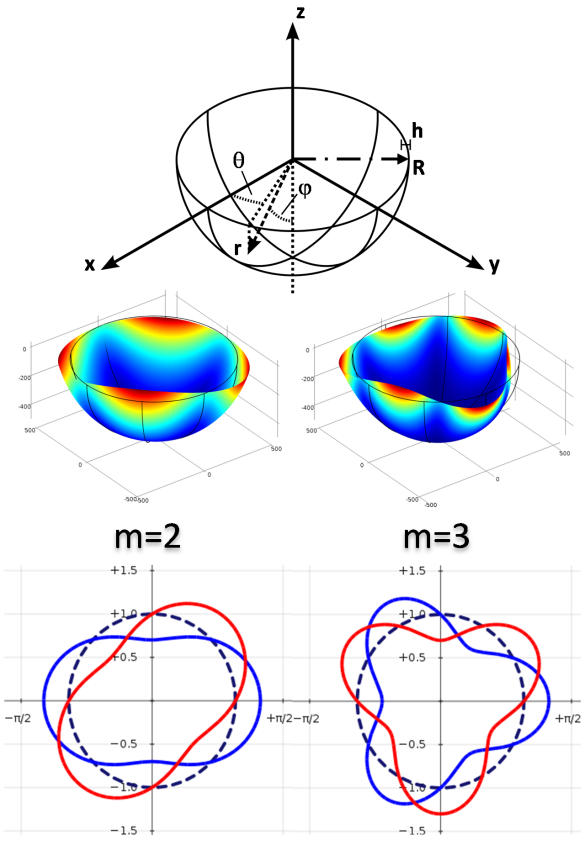

Figure 58: (top) Spherical coordinate system used in this work indicating polar angle φ, circumferential angle θ, and radial position r. The mid-shell radius is R and its thickness is h. (middle) $m = 2$ and $m = 3$ μHSR vibration mode displacement patterns. (bottom) Schematic of the $m = 2$ and $m = 3$ mode patterns at the shell rim depicting the angular alignment between the degenerate mode pairs (see text for details). The scale of the vibration is exaggerated for clarity.

and the radially-directed strain component can be found from

$$\epsilon_{rr} = -\frac{\nu}{1-\nu}\left(\epsilon_{\varphi\varphi} + \epsilon_{\theta\theta}\right). \tag{51}$$

The sinusoidal steady-state equations of motion including the effect of TED can derived

from (22) and (23) in the thin shell approximation in spherical coordinates as

$$
\begin{aligned}
-\rho\omega^2 u_\varphi - \frac{E}{R(1+\nu)(1-2\nu)}\Big[&\frac{\partial}{\partial\varphi}\left((1-\nu)\epsilon_{\varphi\varphi}+\nu\epsilon_{\theta\theta}\right)\\
&+\frac{(1-2\nu)}{\sin\varphi}\frac{\partial\epsilon_{\varphi\theta}}{\partial\theta}+(1-2\nu)\cot\varphi\left(\epsilon_{\varphi\varphi}-\epsilon_{\theta\theta}\right)\Big]=\\
&-\frac{\alpha E}{(1-2\nu)}\frac{1}{R}\frac{\partial T}{\partial\varphi}\\
-\rho\omega^2 u_\theta - \frac{E}{R(1+\nu)(1-2\nu)}\Big[&(1-2\nu)\frac{\partial\epsilon_{\varphi\theta}}{\partial\varphi}\\
&+\frac{1}{\sin\varphi}\frac{\partial}{\partial\theta}\left(\nu\epsilon_{\varphi\varphi}+(1-\nu)\epsilon_{\theta\theta}\right)\\
&+2(1-2\nu)\cot\varphi\epsilon_{\varphi\theta}\Big]=\\
&-\frac{\alpha E}{(1-2\nu)}\frac{1}{R\sin\varphi}\frac{\partial T}{\partial\theta}\\
-\rho\omega^2 u_r + \frac{E}{R(1+\nu)(1-2\nu)}&\left(\epsilon_{\varphi\varphi}+\epsilon_{\theta\theta}\right)=\\
&-\frac{\alpha E}{(1-2\nu)}\frac{\partial T}{\partial r}
\end{aligned}
\tag{52}
$$

$$
\begin{aligned}
j\omega\rho C_P T - \frac{\kappa}{R^2}\Big(&\frac{\partial^2 T}{\partial\varphi^2}+\cot\varphi\frac{\partial T}{\partial\varphi}\\
&+\frac{1}{\sin^2\varphi}\frac{\partial^2 T}{\partial\theta^2}+R^2\frac{\partial^2 T}{\partial r^2}+2R\frac{\partial T}{\partial r}\Big)\\
&=-\frac{j\omega\alpha E T_0}{3(1-2\nu)}\left(\epsilon^z_{\varphi\varphi}+\epsilon^z_{\theta\theta}+\epsilon^z_{rr}\right),
\end{aligned}
\tag{53}
$$

in which (53) retains the z dependency of both T and ϵ_{ij}. This bears similarity to the situation of thermoelastic dissipation in a flexural ring gyro [26]. The mid-surface strains in the hemispherical shell are [21, 22]

$$
\begin{aligned}
\epsilon_{\varphi\varphi} &= \left(\partial u_\varphi/\partial\varphi + u_r\right)/R\\
\epsilon_{\theta\theta} &= \left(\partial u_\theta/\partial\theta + u_\varphi\cos\varphi + u_r\sin\varphi\right)/R\sin\varphi\\
\epsilon_{\varphi\theta} &= \frac{1}{2}\left(\partial u_\varphi/\partial\theta + \sin\varphi\,\partial u_\theta/\partial\varphi\right.\\
&\qquad\qquad \left.-u_\theta\cos\varphi\right)/R\sin\varphi.
\end{aligned}
\tag{54}
$$

Since the shell is considered to be in quasi-inextensional deformation, to find the strains above the mid-surface at position (φ, θ, z), one should calculate the radii of curvature r_{ij} in the φ and θ directions [81, 89]. The strains are then

$$\epsilon_{ij}^{z} = \frac{z}{r_{ij}}, \tag{55}$$

and the radii of curvature are found as

$$\begin{aligned}
&\frac{1}{r_{\varphi\varphi}} = \frac{1}{R^2}\left(\frac{\partial u_\varphi}{\partial \varphi} - \frac{\partial^2 u_r}{\partial \varphi^2}\right) \\
&\frac{1}{r_{\theta\theta}} = \\
&\quad \frac{1}{R^2}\left(\frac{1}{\sin\varphi}\frac{\partial u_\theta}{\partial \theta} + \cot\varphi u_\varphi - \frac{1}{\sin^2\varphi}\frac{\partial^2 u_r}{\partial \theta^2} - \cot\varphi\frac{\partial u_r}{\partial \varphi}\right) \\
&\frac{1}{r_{\varphi\theta}} = \frac{1}{r_{\theta\varphi}} = \\
&\quad \frac{1}{R^2\sin\varphi}\left(\frac{\partial u_\varphi}{\partial \theta} + \sin\varphi\frac{\partial u_\theta}{\partial \varphi} - \cos\varphi u_\theta \right. \\
&\qquad\qquad \left. +2\left(\cot\varphi\frac{\partial u_r}{\partial \theta} - \frac{\partial^2 u_r}{\partial \varphi \partial \theta}\right)\right).
\end{aligned} \tag{56}$$

5.3 Derivation of φ-Dependent Equation of Motion

In (52), let $A = \rho\omega^2$ and $B = \frac{E}{R^2(1+\nu)}$ and set the left-hand side equal to 0. ω is assumed to be small enough that $A << B$ in the quasi-static limit. Then,

$$\begin{aligned}
&-Au_\varphi - BR\frac{1}{(1-2\nu)}\frac{\partial}{\partial \varphi}\left[(1-\nu)\epsilon_{\varphi\varphi} + \nu\epsilon_{\theta\theta}\right] \\
&\qquad - BR\frac{1}{\sin\varphi}\frac{\partial \epsilon_{\varphi\theta}}{\partial \theta} - BR\cot\varphi\left(\epsilon_{\varphi\varphi} - \epsilon_{\theta\theta}\right) = 0 \\
&-Au_\theta - BR\frac{1}{(1-2\nu)\sin\varphi}\frac{\partial}{\partial \theta}\left[\nu\epsilon_{\varphi\varphi} + (1-\nu)\epsilon_{\theta\theta}\right] \\
&\qquad - BR\frac{\partial \epsilon_{\varphi\theta}}{\partial \varphi} - 2BR\cot\varphi\epsilon_{\varphi\theta} = 0 \\
&-Au_r + BR\frac{1}{(1-2\nu)}\left(\epsilon_{\varphi\varphi} + \epsilon_{\theta\theta}\right) = 0.
\end{aligned} \tag{57}$$

From the last line above, it is apparent that

$$u_r = -\frac{1}{2}\left[\frac{\partial u_\varphi}{\partial \varphi} + \frac{1}{\sin\varphi}\frac{\partial u_\theta}{\partial \theta} + \cot\varphi u_\varphi\right]. \tag{58}$$

In other words, u_r is a mixture of u_φ and u_θ and can be considered as a dependent functional. Then the task is reduced to solving for the latter displacements. Plugging in u_r and manipulating the expressions results in

$$\begin{aligned}
&\left[\frac{\partial^2}{\partial \varphi^2} + \cot\varphi\frac{\partial}{\partial \varphi} + 1 + \frac{2A}{B} - \cot^2\varphi \right.\\
&\qquad\left. + \frac{1}{\sin^2\varphi}\frac{\partial^2}{\partial \theta^2} + 2\frac{\cot\varphi}{\sin\varphi}\frac{\partial}{\partial \theta}\right]u_\varphi = 0\\
&\left[\frac{\partial^2}{\partial \varphi^2} + \cot\varphi\frac{\partial}{\partial \varphi} + 1 + \frac{2A}{B} - \cot^2\varphi \right.\\
&\qquad\left. + \frac{1}{\sin^2\varphi}\frac{\partial^2}{\partial \theta^2} - 2\frac{\cot\varphi}{\sin\varphi}\frac{\partial}{\partial \theta}\right]u_\theta = 0.
\end{aligned} \tag{59}$$

Due to the similarity of the expressions for u_φ and u_θ, with the exception of a sign in one of the θ derivatives, one may expect that they are $\cos(m\theta)$ and $\sin(m\theta)$ pairs as in Rayleigh's solutions. Effecting this assumption for the θ dependency results in (for the φ dependency of both u_φ and u_θ)

$$\begin{Bmatrix} u_\varphi(\varphi,\theta) \\ u_\theta(\varphi,\theta) \end{Bmatrix} = u(\varphi)\begin{Bmatrix} \cos(m\theta) \\ \sin(m\theta) \end{Bmatrix} \tag{60}$$

and $u(\varphi)$ satisfies

$$\begin{aligned}
&\left[\frac{\partial^2}{\partial \varphi^2} + \cot\varphi\frac{\partial}{\partial \varphi} + 2\left(1 + \frac{A}{B}\right) \right.\\
&\qquad\left. - \frac{m^2+1}{\sin^2\varphi} - 2m\frac{\cot\varphi}{\sin\varphi}\right]u(\varphi) = 0.
\end{aligned} \tag{61}$$

5.4 Analysis of Bulk TED in μHSRs

5.4.1 The Rayleigh Inextensional Assumption and TED

In Section 5.2, we derive the steady-state thermoelastic equation of motion for a thin isotropic hemispherical shell in the coordinate system of Figure 58. Assuming that (52) and (53) are weakly coupled such that the modal displacement solutions are not significantly perturbed by thermal strains (this can be verified since the right hand side of (52) is multiplied by the coefficient of thermal expansion (α) which is on the order of ppm; further, no significant departure of the mode shapes is seen in the finite element models when they are compared with and without the effect of TED), the displacement degrees-of-freedom (DOFs) can be separated from the temperature DOF when solving the system of equations. Lord Rayleigh first obtained solutions to the left-hand side of (52) for the hemispherical shell by assuming that the mid-surface is in a state of inextensional strain, leading to pure flexural bending modes of the shell [66]. Strictly speaking, Rayleigh's solutions apply only in the case that $\omega \to 0$ (i.e., the quasi-static limit). However, these solutions are usually sufficient for most applications, including the μHSRs considered here. Following Rayleigh's inextensional shell theory [21, 22, 49, 66], the strains on the mid-surface of the hemispherical shell must be identically zero:

$$\epsilon_{\varphi\varphi} = \epsilon_{\theta\theta} = \epsilon_{\varphi\theta} = 0. \tag{62}$$

This sets up a system of partial differential equations, and the resulting mode shapes of the hemispherical shell are [21, 22, 49, 66]

$$\begin{aligned} u_\varphi(\varphi,\theta) &= \frac{1}{\sqrt{m^2+1}} U_{\text{tot.}}^{\max} \sin\varphi \tan^m(\varphi/2) \cos m\theta \\ u_\theta(\varphi,\theta) &= \frac{1}{\sqrt{m^2+1}} U_{\text{tot.}}^{\max} \sin\varphi \tan^m(\varphi/2) \sin m\theta \\ u_r(\varphi,\theta) &= -\frac{1}{\sqrt{m^2+1}} U_{\text{tot.}}^{\max} (m+\cos\varphi) \tan^m(\varphi/2) \cos m\theta. \end{aligned} \tag{63}$$

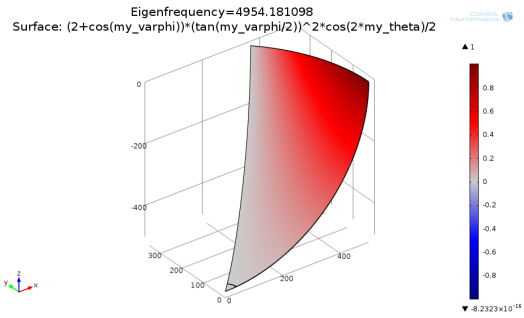

Figure 59: Normalized radial displacement u_r obtained using (63) for a one-eighth axisymmetric sector of the shell.

This model generates the normalized radial displacement u_r shown in Figure 59 for a one-eighth axisymmetric sector of the shell. Similar plots can be obtained for u_φ and u_θ.

Considering the right hand side of (53), the volumetric strain

$$\epsilon^z_{\text{vol}} = \epsilon^z_{\varphi\varphi} + \epsilon^z_{\theta\theta} + \epsilon^z_{rr} \tag{64}$$

is the cause of localized temperature increases and decreases. To account for the effect of these localized temperature changes, which will produce thermal gradients, the volumetric strain must be calculated from (63). If κ becomes non-zero, the locations of heat sources will still be governed by ϵ^z_{vol}, but the temperature field will diffuse (and average) over the shell according to (53). (64) can be simplified by considering (51), resulting in

$$\epsilon^z_{\text{vol}} = \left(\frac{1-2\nu}{1-\nu}\right)\left(\epsilon^z_{\varphi\varphi} + \epsilon^z_{\theta\theta}\right). \tag{65}$$

The volumetric strain can therefore be found by appropriately substituting (55) and (56) into (65). Carrying out the substitutions results in lengthy expressions which are omitted for brevity. Instead, the resulting forms of $\epsilon^z_{\varphi\varphi}$, $\epsilon^z_{\theta\theta}$, and ϵ^z_{vol} are plotted for the $m = 2$ mode over φ and θ of a complete hemisphere in Figure 60. $\epsilon^z_{\varphi\varphi}$ is always equal in magnitude but opposite in sign with $\epsilon^z_{\theta\theta}$; therefore ϵ^z_{vol} is always zero in accordance with (65). This will be true for any m and is a consequence of the inextensional assumption made earlier. This type of strain state is termed *anti-biaxial*. Since ϵ^z_{vol} is zero using this approach, the

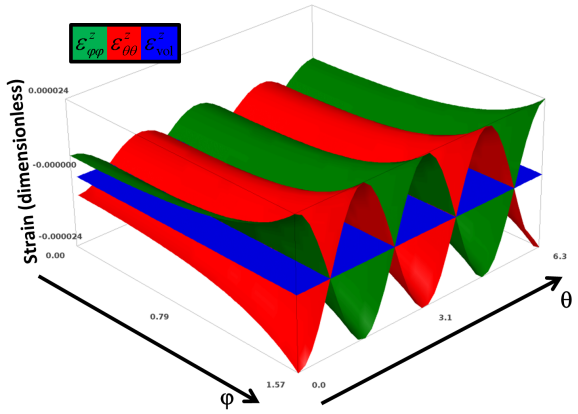

Figure 60: $\epsilon^z_{\varphi\varphi}$ (green), $\epsilon^z_{\theta\theta}$ (red), and $\epsilon^z_{\mathrm{vol}}$ (blue) derived from Rayleigh's solutions showing that $\epsilon^z_{\mathrm{vol}} \propto \epsilon^z_{\varphi\varphi} + \epsilon^z_{\theta\theta}$ is always zero over the shell using inextensional shell theory and therefore the resulting bulk TED is also zero by (53). This strain state is termed *anti-biaxial*.

resulting bulk TED will also be zero since no thermal gradients can develop to cause heat flux in agreement with (53). This result differs from [17], where only the $\epsilon^z_{\theta\theta}$ component of the volumetric strain was considered, but the current result is more complete since all terms of the volumetric strain were considered. As a consequence of the above, linearized shell theory in Rayleigh's inextensional approximation is insufficient for calculating the bulk TED in a hemisphere and requires extension.

5.4.2 Relaxation of the Inextensional Assumption and Neutral Surface Oscillations

The Rayleigh inextensional approximation leads to a semi-trivial solution of the left-hand side of (52) in the quasi-static limit for which the strains, as well as their derivatives, are zero. By relaxing the assumption that the strains on the mid-surface are zero, more general solutions of the elastic part of the equations can be found. In Section 5.3, we find after separating the φ and θ dependence that these solutions must satisfy

$$\begin{Bmatrix} u_\varphi(\varphi,\theta) \\ u_\theta(\varphi,\theta) \end{Bmatrix} = u(\varphi) \begin{Bmatrix} \cos(m\theta) \\ \sin(m\theta) \end{Bmatrix} \tag{66}$$

and

$$\left[\frac{\partial^2}{\partial\varphi^2} + \cot\varphi\frac{\partial}{\partial\varphi} + 2\left(1+\frac{A}{B}\right) - \frac{m^2+1}{\sin^2\varphi} - 2m\frac{\cot\varphi}{\sin\varphi}\right]u(\varphi) = 0, \tag{67}$$

where $u(\varphi)$ represents the φ-dependent part of the solutions.

Analytical solutions to the above differential equation exist in terms of the hypergeometric function which are closely related to the associated Legendre functions $P_n^{\sqrt{m^2+1}}(\cos(\varphi + a_0))$ and $Q_n^{\sqrt{m^2+1}}(\cos(\varphi + b_0))$ [1] and can be seen as perturbed versions of the latter functions since these are the solutions when the $-2m\frac{\cot\varphi}{\sin\varphi}$ term is dropped. Since the associated Legendre functions are orthogonal over the domain of interest, these results suggest that a series expansion of $u(\varphi)$ in terms of the associated Legendre functions would contain a dominant term corresponding to the solution of (67) without the $-2m\frac{\cot\varphi}{\sin\varphi}$ term plus a few significant perturbation components. The remaining perturbation terms can be neglected without significant influence on the final solution. Hence, $u(\varphi)$ can be written as

$$\begin{aligned} u(\varphi) = {} & A_0 P_0^{\sqrt{m^2+1}}(\cos(\varphi + a_0)) \\ & + B_0 Q_0^{\sqrt{m^2+1}}(\cos(\varphi + b_0)) \\ & + \sum_{n\neq 0} A_n^{\text{perturb.}} P_n^{\sqrt{m^2+1}}(\cos(\varphi + a_n)) \\ & + \sum_{n\neq 0} B_n^{\text{perturb.}} Q_n^{\sqrt{m^2+1}}(\cos(\varphi + b_n)). \end{aligned} \tag{68}$$

The above solutions need to satisfy the stress-free boundary conditions which effectively correspond to zero displacement at the bottom of the shell and maximum displacement at the rim. The lowest possible fundamental for a given m corresponds to $n = 0$ in the above. It can be expected that the fundamental solution closely mimics the Rayleigh solution. Figure 61 compares the normalized associated Legendre function $P_0^{\sqrt{m^2+1}}(\cos(\varphi + \pi))$ with the φ-dependent part of the Rayleigh solution as well as the exact hypergeometric solution.

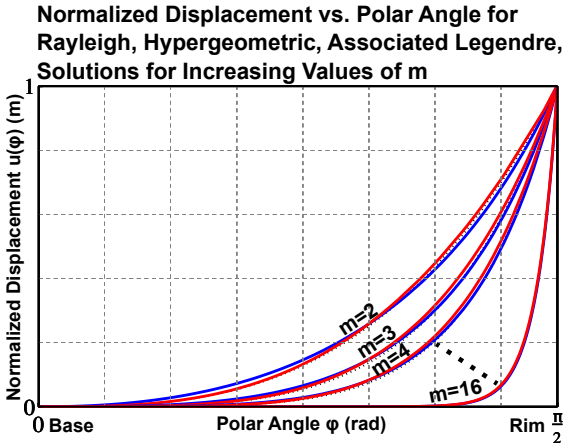

Figure 61: Comparison of normalized $u(\varphi)$ displacement for $P_0^{\sqrt{m^2+1}}(\cos(\varphi+\pi))$ (solid blue line) vs. Rayleigh's solution $\tan^2(\varphi/2)\sin(\varphi)$ (dotted black line) and exact hypergeometric solution (solid red line) showing excellent agreement between these functional forms for the $m = 2, 3, 4$, and 16 modes. As the order of m increases, the forms of the solutions converge.

The functions show a high degree of similarity, and $P_0^{\sqrt{m^2+1}}(\cos(\varphi+\pi))$ satisfies the boundary conditions. This is not true for $Q_0^{\sqrt{m^2+1}}(\cos(\varphi + b_0))$ (it cannot satisfy the boundary conditions, no matter how b_0 is adjusted), so that term is discarded from the solution.

Next, the perturbation terms are considered. For sufficiently high orders of n, the phase shifts a_n and b_n can be adjusted such that the boundary conditions are satisfied. Figure 62 shows as an example the sum of $P_{28}^{\sqrt{5}}(sin(\varphi + a_{28})) + Q_{28}^{\sqrt{5}}(sin(\varphi + a_{28}))$ where $a_{28} = b_{28} = -0.395°$ is a small phase shift sufficient to set the displacement to 0 at the bottom of the shell and keep the displacement finite at the shell's rim. These solutions are overlaid on top of $\cos(28\varphi+\pi/2)$ for comparison, showing that the perturbations mimic an oscillatory pattern which has a sharply increasing envelope near the rim. The reason for selection of $n = 28$ will become clear in the next section. Since the displacement components are oscillatory and the strains on the mid-surface are non-zero, it is expected that the oscillations are reflected into displacement of the neutral surface away from the mid-shell surface. A good approximate model of these types of solutions is

$$u(\varphi) \approx ae^{b\varphi}\cos(c\varphi + d). \tag{69}$$

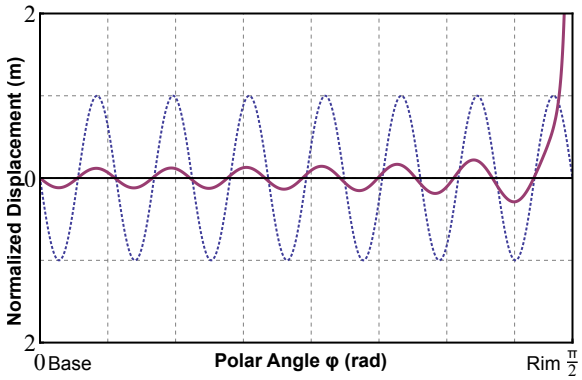

Figure 62: Comparison of the sum of $P_{28}^{\sqrt{5}}(sin(\varphi + a_{28})) + Q_{28}^{\sqrt{5}}(sin(\varphi + b_{28}))$ (solid magenta line) where $a_{28} = b_{28} = -0.395°$ with $\cos(28\varphi + \pi/2)$ (dotted blue line), showing that the perturbation solutions mimic an oscillatory pattern of nearly constant wavelength with a sharply increasing envelope near the rim. A good approximate model of these types of solutions is $ae^{b\varphi}\cos(c\varphi + d)$.

5.4.3 Determination of Bulk TED Thermal Path from Neutral Surface Oscillations

The oscillation of the neutral surface will set the thermal path of bulk TED. The thermal path is defined as the average path length between the hottest and coolest regions of the shell. The cos term reflecting the spatial behavior of the neutral surface oscillations in (69) has as argument $c\varphi$. This can be rewritten as $c\varphi = \frac{cR\varphi}{R} = k_\varphi \cdot R\varphi$, which yields $k_\varphi = \frac{2\pi}{\lambda} = \frac{c}{R}$, giving $\lambda = \frac{2\pi R}{c}$. Then the thermal path d can be taken as $d \approx \frac{1}{2}\lambda = \frac{\pi R}{c}$. To determine c, an analogy may be drawn between an infinitely thin plate and an infinitely thin hemisphere as was done in Section 5.2. The perturbing oscillations to the neutral surface of the shell have a flexural characteristic similar to the 0^{th}-order antisymmetric Lamb waves, which exhibit a dependence of the acoustic wave velocity on the ratio of the plate thickness to the wavelength [40]. Hence, for a finite thickness shell of small h/R ratio, we may expect the oscillatory component which matches the dispersion condition to become dominant. Indeed, FE models confirm this effect. From FE results similar to those shown later in Figure 67 for various shell thickness, the constant c is extracted to be

$$c \approx \frac{5}{4}\left(\frac{h}{R}\right)^{-\frac{1}{2}}. \tag{70}$$

In the case of an $R = 500$ μm, $h = 1$ μm μHSR, c is found to be equal to 28 by the above formula (i.e., there are 14 full wavelengths of the oscillation over the φ direction of the hemisphere). Therefore, the thermal path can be found as

$$d \approx \frac{4}{5}\pi R\left(\frac{h}{R}\right)^{\frac{1}{2}} = \frac{4}{5}\pi\left(Rh\right)^{\frac{1}{2}}. \tag{71}$$

5.4.4 Finite Element Implementation of Bulk TED

COMSOL multiphysics was used as the finite element software to solve the fully-coupled system of equations defined in (22) and (23). COMSOL is a powerful FE suite and allows nearly arbitrary coupling of different built-in physics domains, in addition to custom equations. In this work, the Solid Mechanics module of COMSOL was used with thermal expansion enabled to account for the left and right hand sides of (22). The Heat Transfer in Solids module was used to account for the second term on the left of (23), and the first term on the left and the right hand side were co-implemented as a body heat source. Shell-type finite elements can be used to study the behavior of hemispherical shells, but these use simplifying assumptions about the nature of the strain in the thickness direction (i.e., (50)). Instead, fully-3D quasi-cuboidal finite elements are used, which retain the full six-component stress and strain matrices and more accurately capture the behavior of the μHSR through its thickness. As shown in Figure 63, a mapped meshing scheme is used over the μHSR with uniformly-sized elements. The mesh is constructed so that it is fully-symmetric, and convergence of the element size indicates that agreement of less than 1 mHz between the degenerate modes can be achieved, setting the numerical error [85]. Further, decreasing the size of the elements in the lateral directions (across the surface area) of the shell is determined to be more important for convergence than layering elements in the thickness direction, since the aspect ratios of the elements approach unity. Using a sufficiently powerful compute node, meshes with lateral element dimensions less than 1.5 μm were created, consuming upwards of 60 GB of physical memory during the fully-coupled

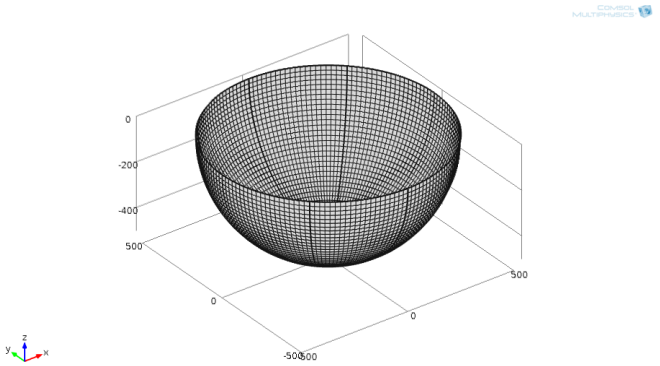

Figure 63: An example of the fully-symmetric mapped meshing strategy used in the COMSOL model for a shell with $R = 500$ μm and $h = 1$ μm.

TED solution process for the one-eighth axisymmetric sector model of the shell. A nominal shell radius and thickness of 500 μm and 1 μm were used, respectively, and are assumed in the latter figures unless otherwise specified. Material properties for silicon dioxide (Table A.4) were taken from the COMSOL material property database and are in good agreement with typical values reported in literature.

Figure 64 plots the result of solving the COMSOL model for the $m = 2$ mode shape and extracting $u(\varphi)$. Excellent agreement is obtained between the FE results and the analytical models discussed earlier. Figure 65 shows the volumetric strain which is derived from these displacements in the absence of thermal conductivity ($\kappa = 0$). The resulting temperature field is a scaled version of the volumetric strain field. In contrast, in the case $\kappa \neq 0$, the temperature diffuses through the thickness of the shell, effectively eliminating the thermal gradient in the radial direction. However, the heat sources still result from the volumetric strain pattern, and lateral thermal gradients form over the surface of the shell (Figure 66).

In these models, the neutral surface of the μHSR is observed to not lie in the exact middle of the shell (Figure 67). Instead, the deviations of the neutral surface from the mid-surface oscillate with rapid decay from the rim of the shell to its bottom, in agreement with the oscillatory behaviors predicted by the perturbation terms of the analytical model. Further, these oscillations are observed across several orders of magnitude in the h/R ratio

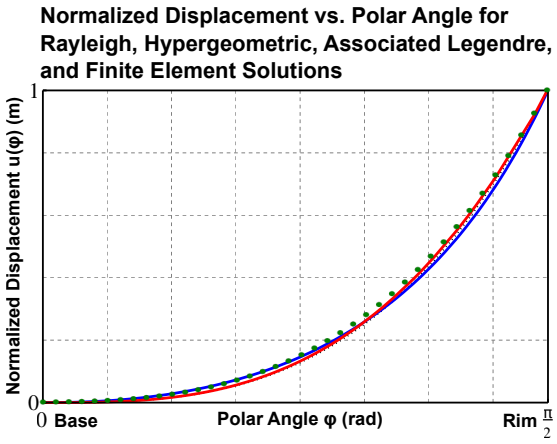

Figure 64: Comparison of various solutions of normalized $u(\varphi)$ for $m = 2$ mode. Analytic solutions are the Rayleigh inextensional modes (dotted black line), the exact hypergeometric solution (solid red curve), and $P_0^{\sqrt{m^2+1}}(\cos(\varphi + a_0))$ (solid blue line). The finite element results (green circles) are overlaid onto these plots and show excellent agreement.

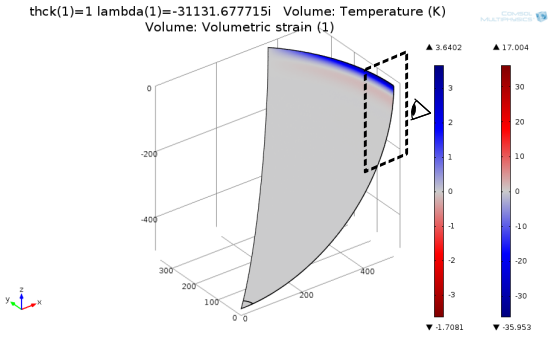

Figure 65: Volumetric strain and temperature field obtained using COMSOL assuming thermal conductivity $\kappa = 0$. These fields are not uniform through the thickness of the shell. The eye and dashed black box indicate the perspective in Figure 67.

of the shell and remained present after a convergence study with multiple layers of elements (Figure 67). The consistency of these results suggest that the oscillation of neutral surface is a physical feature of the shell and not an artifact of the finite element solution. In fact, the finite element solution can support the linear change in the strain through the thickness of a shell element required by Rayleigh's inextensional shell theory, but the computation converges to the result where the neutral surface does not lie on the mid-surface of the shell. Figure 67 shows the finite element results for 1 μm, 4.6 μm, and 10 μm shells, respectively, and illustrates the dependency of the neutral surface (determined by the locations where

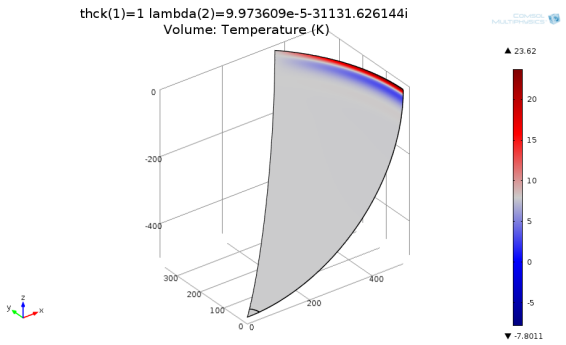

Figure 66: Temperature field obtained using COMSOL assuming thermal conductivity $\kappa \neq 0$. This field is approximately uniform through the thickness of the shell.

$\epsilon^z_{\text{vol}} = 0$) on the ratio of the shell's thickness and radius. It is observed that the neutral surface exits the shells (representing the first half wavelength of the oscillation) on their inner surfaces at greater depths for the thicker shells. These results verify the predictions of the analytical model based on associated Legendre functions.

As was shown in Figure 60, inextensional shell theory was found to predict zero volumetric strain and hence zero bulk TED for the μHSR. The reason for this was the anti-biaxial state of strain in the φ and θ directions, whose total was always zero. Since the sum of the diagonals of the strain matrix is an invariant, if the strain matrix is diagonalized to find the principal strains, then the sum of these principal strains, and the volumetric strain, must also be zero. Hence, the principal strains, whose orientations may occur along rotated directions on the surface of the shell compared with the φ and θ directions, must also exist in a state of anti-biaxial strain. Plotting the principal strains for the case of Figure 8 is shown in Figure 68. This figure shows an approximately anti-biaxial strain state calculated by COMSOL for the principal strains along the first (blue) and second (red) principal strain directions, respectively. The arrow heads indicate that the first principal strains are compressive for this section of the shell, while the second principal strains are tensile. If there exists a difference in magnitude between the first and second principal strains at any location on the shell, the result is a non-zero third principal strain normal to the shell's surface, which results in non-zero volumetric strain and is the actual cause of bulk TED

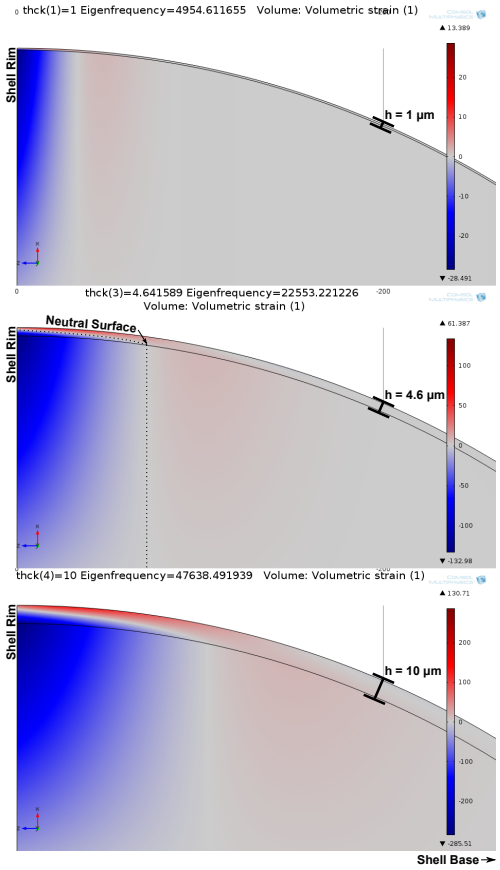

Figure 67: Volumetric strain looking toward the ZX plane (as indicated in Figure 65) showing neutral surface (determined by the locations where $\epsilon^{z}_{\text{vol}} = 0$) for (top) 1 µm, (middle) 4.6 µm, and (bottom) 10 µm thick shells, showing the dependency of the neutral surface oscillations on the h/R ratio of the shell. The shell radius is 500 µm in all cases.

in the µHSR according to the neutral surface oscillations. Although this figure shows the particular case of $m = 2$, the anti-biaxial strain state will occur for any low-order m.

5.4.5 Finite Element Verification of Bulk TED Thermal Path

As seen in Figure 66, the localized hot and cool regions for a thin shell with finite thermal conductivity are effectively determined by averaging the temperature distribution through the thickness of the shell obtained in the absence of thermal conductivity due to thermal diffusion. This suggests a method to extract the thermal path: first obtain the volumetric strain on the inner and outer surfaces, and then average the results to produce an approximation of the temperature distribution over the surface of the shell from which the thermal

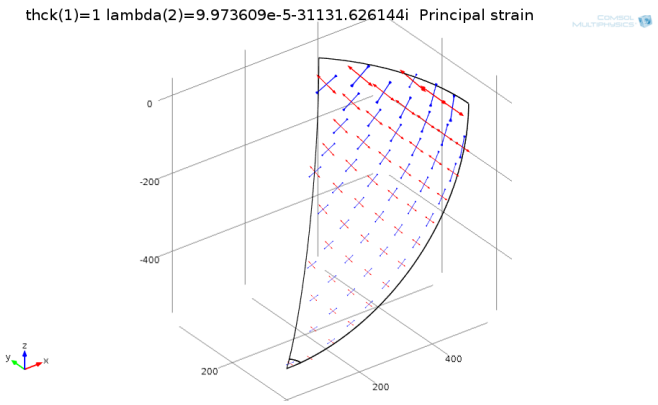

Figure 68: Anti-biaxial principal strain state for $m = 2$ inextensional mode shown on outer surface of shell for a one-eigth axisymmetric sector. Inner surface is similar with opposite sign. Blue (red) arrows represent the first (second) principal strain axis and magnitude.

path can be calculated. Since the volumetric strain follows the same $\cos(m\theta)$ and $\sin(m\theta)$ dependence as the displacements, it suffices to examine the inner and outer surfaces along the polar direction in the ZX plane. Figure 69 plots the volumetric strain for a $R = 500$ μm, $h = 1$ μm shell in the $m = 2$ mode along its inner and outer surfaces for $\kappa = 0$. Excellent fits could be obtained to the FE data by the approximate models given in (69). Parameters b and c of Figure 69 are approximately equal, suggesting they can be reduced to a single effective parameter b', resulting in

$$\epsilon_{\text{vol}}(\varphi, \theta, z = -\frac{h}{2}) \approx C\frac{h}{2R^2}\cos(m\theta)\, e^{(b'\varphi)}\cos(b'\varphi) \tag{72}$$

on the inner surface, and

$$\epsilon_{\text{vol}}(\varphi, \theta, z = +\frac{h}{2}) \approx -C\frac{h}{2R^2}\cos(m\theta)\, e^{(b'\varphi)}\sin(b'\varphi) \tag{73}$$

on the outer surface, where C is an arbitrary constant.

If $\kappa \neq 0$, then the localized temperature will correspond to the averaged volumetric

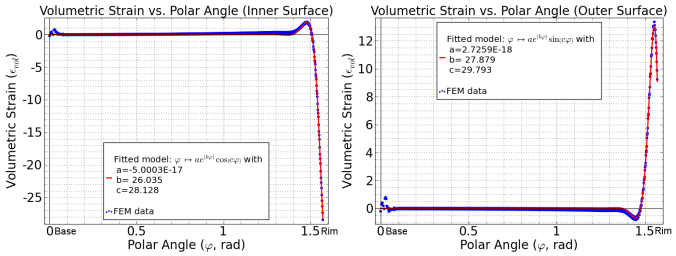

Figure 69: Volumetric strain vs. polar angle on (left) inner and (right) outer surfaces showing form of (72) and (73) with $b \approx c$. Finite element data is shown by points and the fitted model is shown by a solid line.

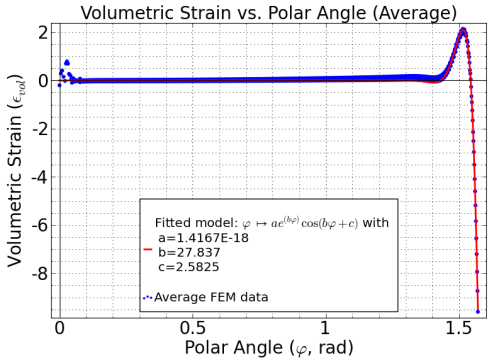

Figure 70: Averaged volumetric strain over both inner and outer surfaces vs. polar angle showing form of (74). The model parameters here are b' and c' which differ from b and c of Figure 69 as explained in the text.

strains on the inner and outer surfaces:

$$\epsilon_{\text{vol}}^{\text{avg}}(\varphi,\theta) \approx C\frac{h}{\sqrt{2}R^2}\cos(m\theta)\, e^{(b'\varphi)}\cos\left(b'\varphi+\frac{\pi}{4}\right), \tag{74}$$

where the resulting temperature profile is

$$T_{\text{avg}}(\varphi,\theta) \approx T_{\max}\frac{h}{\sqrt{2}R^2}\cos(m\theta)\, e^{(b'\varphi)}\cos\left(b'\varphi+\frac{\pi}{4}\right). \tag{75}$$

Figure 70 shows (74) fitted to the averaged volumetric strain data of Figure 69. Figure 71 uses the same parameters b' and c' as Figure 70 in (75) and a very good fit is maintained in the presence of finite κ despite being extracted from volumetric strain data.

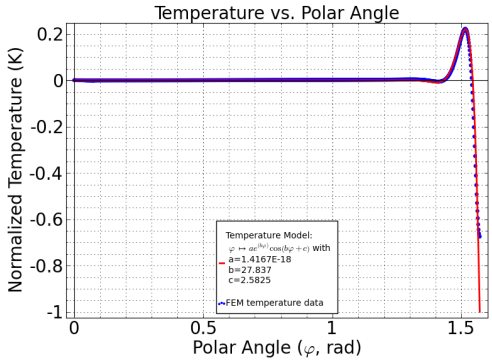

Figure 71: Temperature vs. polar angle on shell ZX plane showing excellent match with form of (75) using the same parameters as in Figure 70.

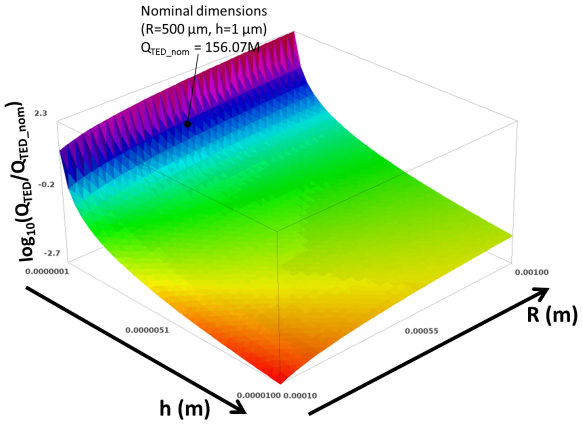

Figure 72: Normalized bulk TED Q factor vs. h and R near normalization point showing scaling trend. The normalization point is $h = 1$ µm, $R = 500$ µm, for which a Q_{TED} of 156.07 million was obtained from Figure 66.

5.4.6 Scaling Law of Bulk TED in µHSRs

Combining (48), (27)–(29), and (71) yields

$$Q_{\text{TED}} = \left(\frac{5}{4}\right)^2 \frac{\sqrt{3}}{m\,(m^2-1)\,\sqrt{K_m}} \frac{\kappa\sqrt{\rho\,(1+\nu)}}{sE^{\frac{3}{2}}\alpha^2 T_0} \frac{R}{h^2} \tag{76}$$

The factor s is included to account for the difference between the relaxation strength before and after averaging of the temperature due to diffusion both laterally and across the thickness. An exact value for s could be determined by the use of Green's functions to calculate the exact temperature profile for a given maximum displacement after accounting for diffusion assuming as input the heat source distributions determined when $\kappa = 0$, but

a worst-case lower bound of Q_{TED} can be obtained by simply setting $s = 1$. (76) is plotted for an oxide μHSR over different ranges of h and R in Figure 72, respectively. In this case, s was determined by the FE results in Figure 66 for the nominal shell parameters by $Q_{\mathrm{TED}} = \frac{\mathrm{Im}\{\lambda\}}{2\mathrm{Re}\{\lambda\}}$ [4].

5.5 Analysis of Surface TED in μHSRs

5.5.1 Finite Element Model of a Single Asperity by Gaussian-shaped Young's Modulus Perturbation

In [85], it was demonstrated that there is a direct equivalence between a thickness perturbation at a point on the shell and an equivalent change in Young's modulus, up to a factor of ½. This fact can be exploited in the analysis of asperities on μHSRs. Figure 73 shows an exemplary Young's modulus mapping of an asperity with a Gaussian profile with its standard deviation equal to 1° in both the φ and θ directions. Figure 74 shows the result of solving the preceding model for the volumetric strain. The solution method uses the same fully-coupled thermoelastic approach in COMSOL as for bulk TED. It is noted that there is a volumetric strain build-up in the vicinity of the asperity. The volumetric strain concentrates in four lobes around the base of the asperity. Figure 75 shows a zoomed-in views of the μHSR surface in the vicinity of the Gaussian asperity (indicated by concentric rainbow-colored contours in the top image). The top image clearly shows the development of the four lobes of volumetric strain with alternating sign around the base of the asperity (indicated by the red-white-blue contours). The orientation of these lobes is found to agree with the anti-biaxial principal strains (blue and red arrows). Due to the temperature increase and decrease associated with the volumetric strain concentrations around the base of the asperity, the thermal gradients can be calculated, showing lateral heat flux around the base of the asperity. In the case that $\kappa = 0$, the lobes of hot and cold temperature are coincident with those of the volumetric strain build-up around the asperity. This is illustrated by the middle image of Figure 75. However, when $\kappa \neq 0$, the temperature diffuses over the area and through the thickness of the shell (bottom image of Figure 75).

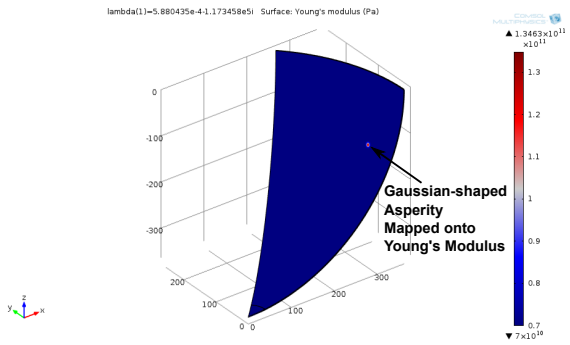

Figure 73: Shell with single Gaussian-shaped asperity with angular spread (standard deviation) of 1°. At the center of the asperity, the Young's modulus is modified to be close to 200% of normal (i.e., double the effective stiffness).

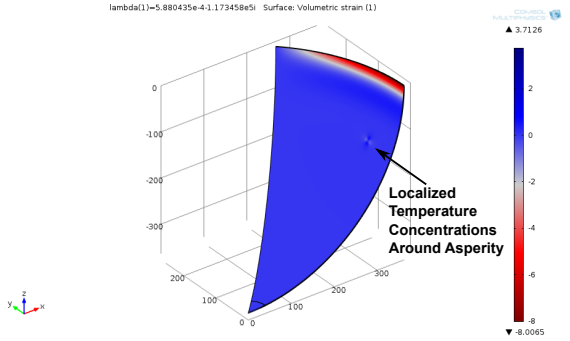

Figure 74: Shell with single Gaussian-shaped asperity showing resulting volumetric strain pattern. The volumetric strain concentrates in four lobes oriented along the principal strain directions around the base of the asperity.

5.5.2 Analogy to Asperity on 2D Plate in Anti-Biaxial Principal Strain

In Section 5.2, an analogy was made between the situation of a thin shell and that of a thin plate. This analogy can also apply to the situation of an asperity on a thin shell or on a thin plate. Figure 76 shows the latter case, where the principal strain axes line up with the global x and y axes. Instead of mapping the thickness variation associated with the asperity to the Young's modulus, in this case a conical asperity was included geometrically at the center of the circular plate. The plate is circular in shape and forced to be in anti-biaxial strain. The actual shape of the plate on which the asperity lies is not of great importance to this model. Figure 76 shows a zoomed-in top view of the asperity located on the plate. The principal strain axes have been made visible to indicate the anti-biaxial strain state. In

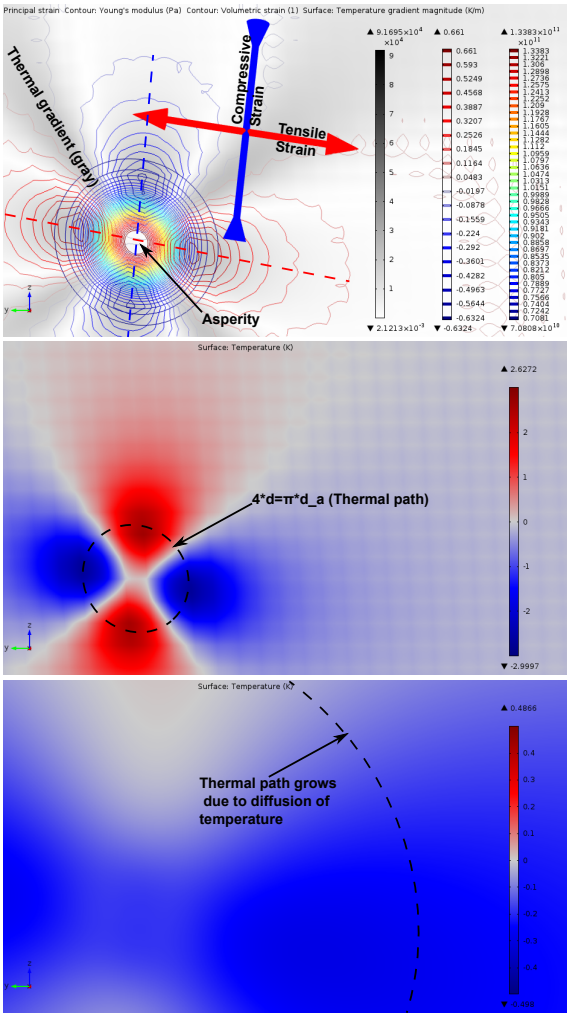

Figure 75: (top) Close-up of Gaussian asperity (indicated by rainbow-colored contours) showing anti-biaxial principal strain axes (blue and red arrows). The lobes of the volumetric strain pattern (indicated red-white-blue contours) agree with the orientation of the principal strain axes. There is a lateral heat flux around the diameter of the asperity indicated by the non-zero thermal gradient (shown in grayscale). (middle) Same view of asperity showing the temperature field in the case that $\kappa = 0$. The lobes of the temperature pattern agree with the lobes of the volumetric strain shown earlier as a consequence of (53). (bottom) Same view of asperity showing the temperature field in the case that $\kappa \neq 0$. Although the lobes of the temperature pattern agree with the volumetric strain as in Figure 75, the temperature is found to diffuse across the surface and through the thickness of the shell due to non-zero κ.

addition, it is found that there is agreement of the volumetric strain with the orientation of the principal strain axes, as was demonstrated previously for the μHSR in Figure 75. Figure 76 shows a quarter section of the asperity on the thin plate. This figure shows clearly that the maximum of the volumetric strain build-up occurs almost exactly at the base of the

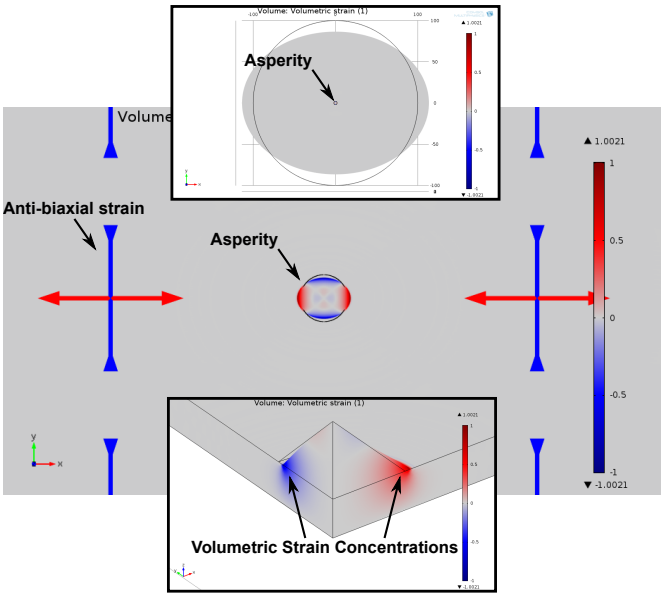

Figure 76: Top view of conical asperity on circular plate in anti-biaxial strain. The principal strain axes are indicated by blue and red arrows. The color scale indicates volumetric strain, showing that the four lobes of maximum and minimum volumetric strain are oriented along the principal strain axes. (top inset) Zoomed-out top view of a conical asperity (small circle) located at the center of a thin circular plate in anti-biaxial strain. The principal strain axes are along the global x and y axes. (bottom inset) Quarter-section cut of the conical asperity showing that the location of maximum volumetric strain occurs precisely at the base of the asperity.

conical asperity, in the direction of the principal strain axes. Hence, the asperity appears locally on the shell as if it were sitting on a plate in anti-biaxial strain.

5.5.3 Limitations of the Numerical Model

In Figure 75, errors in the temperature field due to the finite element mesh are visible as a grid of edges corresponding to the mapped mesh surface. As the asperity size is brought smaller and smaller, it will eventually approach the size of an element without resorting to complicated meshing approaches. To overcome the limitations of the finite element mesh, an alternative is to develop an analytical model which is not limited by the absolute size of the asperity.

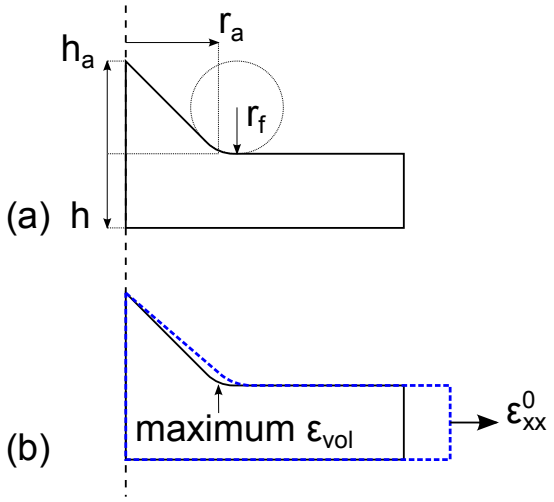

Figure 77: Schematic views of a conical asperity on a thin plate or shell. (a) The parameters of the asperity are its height h_a, radius $r_a = d_a/2$, and its radius of curvature at its base r_f. The scale is set by the plate or shell thickness h. (b) In the case of anti-biaxial principal strain, the plate deforms in the x direction with a strain equal to ϵ^0_{xx}. The asperity is forced to deform accordingly, resulting in a volumetric strain concentration approximately located at $x = r_a$. The deformation is shown with a dashed blue outline, while the original geometry is shown with a solid black line.

5.5.4 Analytical Model of Surface TED due to Asperities

Figure 77 shows the parameterized geometry of the single conical asperity model. In addition to the thickness of the shell, h, the height and radius of the asperity (h_a and r_a, respectively) define the dimensions of a single asperity. Since a sharp corner will develop into a singularity in the strain, it is also necessary to assume a fillet radius r_f (i.e., the radius of curvature) of the asperity to shell transition. Under application of an external anti-biaxial strain $\epsilon^0_{xx} = -\epsilon^0_{yy}$, the maximum volumetric strain will be found at position $r_a = d_a/2$ but is no longer determined by (65). To account for this change of volumetric strain in (53), the relaxation strength of the Young's modulus needs to be modified. In this case, (27) becomes

$$\Delta_E = \frac{E\alpha^2 T_0}{\rho C_p}\left(2\frac{h_a}{d_a}\right)\left(\frac{r_{f0}}{r_f}\right), \tag{77}$$

where r_{f0} is the fillet radius for which $\epsilon_{\text{vol}} = 1$ in the case that $h_a = d_a/2$. The thermal path

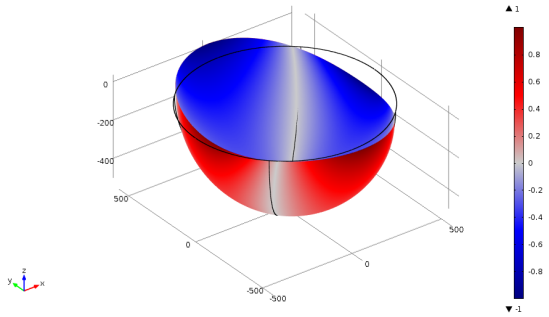

Figure 78: Normalized strain $\epsilon^z_{\varphi\varphi}$ for $m = 2$ mode of a μHSR derived analytically according to (55). A stronger color indicates a higher participation factor P for an asperity centered at that location on the shell, where red indicates positive (dilational) volumetric strain and blue indicates negative (compressional) volumetric strain. The white nodal lines are areas with the least participation (smallest P). Similar results are obtained for $\epsilon^z_{\theta\theta}$ with an exchange of the sign.

becomes

$$d = \frac{\pi}{4} d_a. \tag{78}$$

Combining the above with (29) yields (for a single asperity)

$$Q_{\text{TED}}^{\text{asp.}} = \sqrt{\frac{3}{2}} \frac{8}{m\left(m^2-1\right) P \sqrt{K_m}} \cdot \frac{\sqrt{\rho\left(1+\nu\right)}\kappa}{s E^{\frac{3}{2}} \alpha^2 T_0} \frac{R^2}{h} \frac{1}{h_a d_a} \frac{r_f}{r_{f0}} \tag{79}$$

where P is the participation factor of the asperity and can be found from normalizing $\epsilon^z_{\varphi\varphi}$ or $\epsilon^z_{\theta\theta}$ in Figure 60. $\epsilon^z_{\varphi\varphi}$ is normalized and plotted in Figure 78, where the strength of the coloring indicates the magnitude of P for an asperity centered on the corresponding location. Based on finite element models similar to Figure 76, r_{f0} is estimated to be approximately $0.1 h_a$ for $h_a = d_a/2$.

5.5.5 Estimation of $Q_{\text{TED}}^{\text{asp.}}$ for a Single Asperity

Figs. 79 and 80 show the prediction of (79) for the $m = 2$ inextensional mode of a 1 mm diameter oxide shell of varying thicknesses using the material properties given earlier

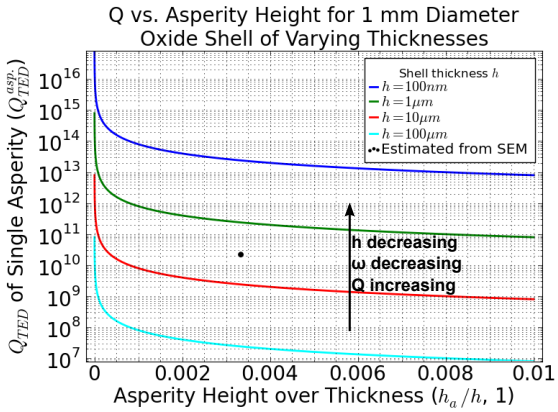

Figure 79: Q_{TED} of a single asperity plotted vs. the asperity height for varying shell thicknesses on a 1 mm diameter oxide μHSR predicted by (79). The nominal asperity diameter and height were 200 nm and 10 nm, respectively. The black dot shows the result for a 910 μm diameter, 3 μm thick oxide μHSR corresponding to the SEM image of Figure 82 with the same nominal asperity dimensions. As the thickness is decreased, the μHSR's resonance frequency also decreases, resulting in higher $Q_{\text{TED}}^{\text{asp.}}$ as the resonator operates deeper in the isothermal regime. However, for a fixed shell thickness, as the asperity height is increased, surface dissipation correspondingly increases, reducing $Q_{\text{TED}}^{\text{asp.}}$, which agrees with the expected trend for surface losses.

varying asperity height and diameter, respectively. Increasing either the height or diameter of the asperity is found to decrease the Q. Although increasing d_a decreases the amount of volumetric strain generated at the base of the asperity, and therefore the strength of the thermal gradient, the thermal relaxation is increased by the square of d_a. This longer thermal path is the cause of increased dissipation in the isothermal regime of operation. In this case, r_f was taken to be equal to r_{f0}, and P and s were set equal to 1. For a 1 μm thick shell with asperity height of 10 nm and diameter of 200 nm in these conditions, $Q_{\text{TED}}^{\text{asp.}}$ of a single asperity is estimated to be 7.9E10 by (79). In addition, the thinner shells are determined to have higher surface Q_{TED} as a consequence of shifting the resonance frequency to lower frequency, even though for a fixed thickness, the greater the height of the asperity, the worse is the dissipation, which agrees with the expected trend for surface losses.

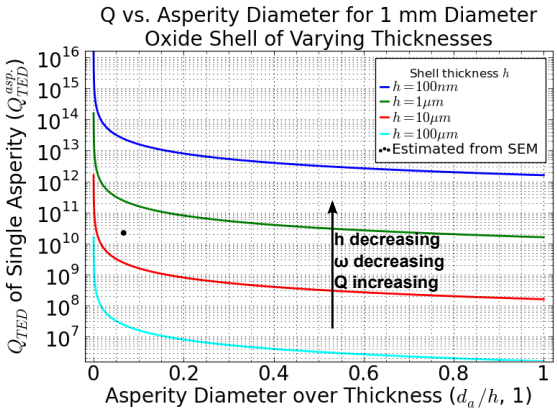

Figure 80: Q_{TED} of a single asperity plotted vs. the asperity diameter for varying shell thicknesses on a 1 mm diameter oxide μHSR predicted by (79). The nominal asperity diameter and height were 200 nm and 10 nm, respectively. The black dot shows the result for a 910 μm diameter, 3 μm thick oxide μHSR corresponding to the SEM image of Figure 82. Similar trends are observed as in Figure 79.

5.5.6 Estimation of Number of Asperities

Although the $Q_{\text{TED}}^{\text{asp.}}$ of a single asperity is very high (above the bulk TED limit), there can be a large number of asperities on the shell's surface. Thus, the overall Q due to surface TED can be found from

$$Q_{\text{TED}}^{\text{surf.}} = Q_{\text{TED}}^{\text{asp.}}/N_a, \tag{80}$$

where N_a is the effective number of asperities (accounting for P). To find N_a, assuming that the asperities are close-packed over the shell's surface results in

$$N_a \approx 0.906\frac{2\pi R^2}{\pi(d_a/2)^2} = 7.25\left(\frac{R}{d_a}\right)^2. \tag{81}$$

Using the parameters as the above single asperity example, for close-packed asperities across the surface of the hemisphere, there would be just over 45 million asperities, resulting in a $Q_{\text{TED}}^{\text{surf.}}$ of only 1750. Although there can be a large variability in the surface asperity parameters and distribution, as well as the relaxation strength factor s and participation factor P, this example shows that it is plausible that surface TED due to asperities can be a

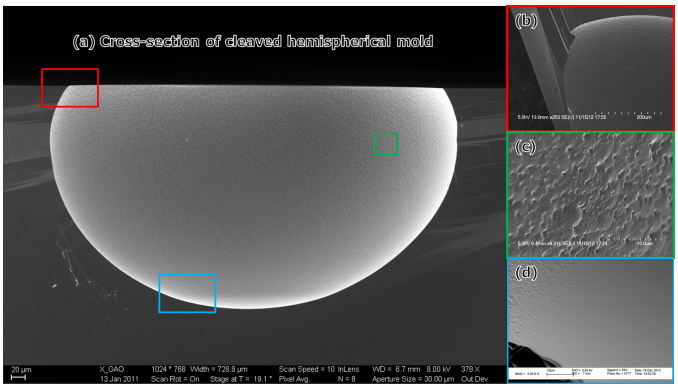

Figure 81: SEM views of typical features of hemispherical molds etched in single-crystal silicon (SCS) wafers similar to that demonstrated in [84]. (a) Cross-section view of hemispherical mold obtained by cleaving wafer approximately through center of mold; (b) tilted view of cleaved mold near the rim showing concentration of surface asperities; (c) close-in view of sharply-pointed asperities on the mold surface; (d) transition to smooth surface free of asperities near the bottom of the mold. The surface asperities in the SCS mold were found to have the highest concentration near the mold rim, while the asperity concentration decreases near its bottom. This is presumed to be due to direct bombardment with SF_6 plasma in high density at the bottom, while the sidewalls are indirectly exposed to scattered SF_6 etchant.

dominant dissipation mechanism in thin μHSRs and are significantly more influential than bulk TED for these devices.

5.6 Experimental Results

5.6.1 Fabrication-based Origins of Surface Asperities

These surface asperities originate in the case of micromolded μHSRs by transfer from the micromold surface to the surface of the shell itself. Figure 81 shows typical surface asperities found in single-crystal silicon (SCS) molds created by an SF_6 isotropic etching process [77, 84]. The distribution of asperities is naturally determined by the fabrication processes. While some efforts may be made to smooth the molds and surfaces to remove asperities (e.g., oxidation), there may be a practical limit to the achievable surface roughness.

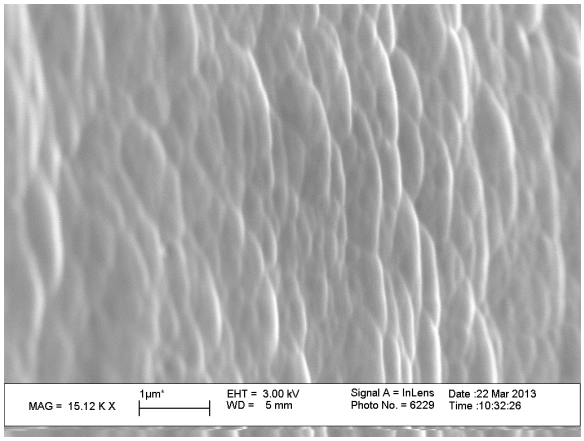

Figure 82: SEM view of surface of 910 μm diameter, 3 μm thick oxide shell grown according to [77], where a single iteration of growth and stripping of oxide was performed to smooth the shell. The surface was coated with a conductive Pt layer by atomic layer deposition (ALD). Based on the SEM scale, the nominal asperity diameter are estimated to be 200 nm and 10 nm, respectively.

5.6.2 Surface of Oxide Shell

Figure 82 shows the final oxide shell surface after growing oxide in the mold of Figure 81. The oxide was grown and stripped and then regrown to smooth the original surface of the mold, but residual asperities remain. These are roughly estimated to be in good agreement with the earlier assumption of 10 nm height and 200 nm diameter. The predicted nominal $Q_{\mathrm{TED}}^{\mathrm{asp.}}$ for this case was shown with black dots in Figs. 79 and 80.

5.6.3 Measurement of Quality Factor

Figure 83 shows the measurement of a 910 μm diameter, 3 μm thick Pt-coated oxide shell with approximately the same residual surface roughness shown in Figure 82. An Agilent 4395a network analyzer was used in the measurement, and electrical loading of the Q was ruled out due to the high motional impedance of the device (originating with large capacitive transduction gaps) as well as by conducting the test with both close to 0 Ω (by use of a transimpedance amplifier) and 1 MΩ terminations. The measured Q is 19,100 at 19.2 kHz. This is within an order of magnitude of the close-packed asperity estimation, showing good agreement with the model. The discrepancies can arise due to difference in

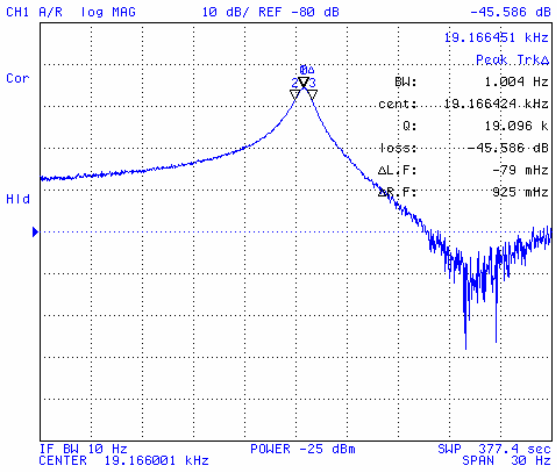

Figure 83: Network analyzer measurement of a 910 μm diameter, 3 μm thick Pt-coated oxide μHSR similar to Figure 57. A Q of 19,100 was measured at 19.2 kHz.

the actual distribution of large diameter asperities, which may be less-than-close-packed and can explain the order of magnitude difference. The measured value of Q is well away from the bulk TED lower bound, meaning bulk TED does not play a significant role in this particular device.

Figure 84 shows measurements on the same μHSR with varying vacuum chamber pressures. Using a two component model for Q consisting of a constant value at the lowest pressure point plus the inverse pressure dependency ($Q^{-1} = Q^{-1}_{\text{const.}} + Q^{-1}_{\text{air}}(P)$), a theoretical trend line can be extracted for Q [13]. This shows that below a certain pressure level, the Q becomes independent of the loss to the surrounding air. Hence, a dissipation mechanism other than air loss is dominant at low chamber pressures, and surface TED still plays a plausible role in explaining the final Q.

Figure 85 shows further results from the same μHSR measured by holding the vacuum chamber pressure constant at 1 μTorr and varying the ambient temperature of the chamber. A linear TCf of +61.9 ppm/°C was observed, which is mainly attributed to the shear modulus of the device. Interestingly, an inverse trend of the Q was observed with temperature above +40°C, which is in agreement with (79). Below +40°C, the Q began to saturate and drop slightly toward lower temperatures, suggesting an effect that is not related to TED

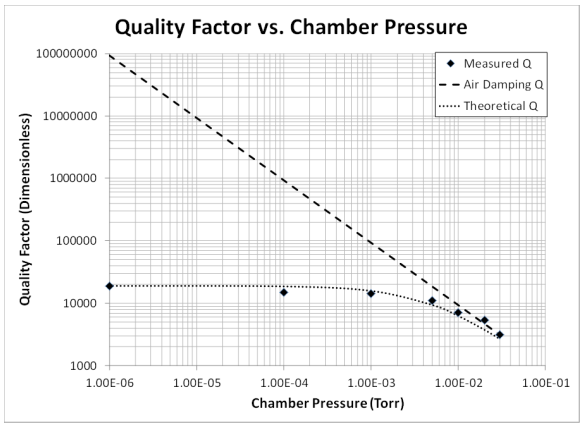

Figure 84: Quality factor measurements similar to Figure 83 measured vs. vacuum chamber pressure level. The diamonds represent measured data points, while the dashed line indicates the expected inverse dependency of Q on chamber pressure, extrapolated from the highest pressure point. When combined with a dissipation mechanism constant over pressure, the theoretical air damping trend produces the theoretical Q trend, which explains well the saturation behavior of measured Q vs. pressure. Therefore, another dissipation mechanism besides air damping is expected to dominant the Q at low pressures, and surface TED plausibly explains this trend.

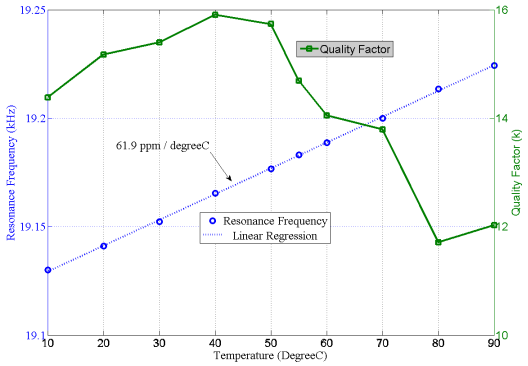

Figure 85: Quality factor measurements similar to Figure 83 measured vs. vacuum chamber temperature at highest vacuum level (1 μTorr). The measurements were taken several days after those of Figure 84 and the maximum measured Q was reduced to 16,000, presumably due to exposure to humidity in the ambient air. Between 40°C and 90°C, an inverse trend vs. temperature was observed, which suggests a TED origin in accordance with (79). Below 40°C, a slight downward trend in Q toward lower temperatures is observed, which may indicate other sources of dissipation (such as water saturation) begin to dominant over the surface TED. Interestingly, the f vs. T behavior of the device is highly linear with a TCf of +61.9 ppm/°C, suggesting that μHSRs may be useful structures for characterizing temperature behavior of shear modulus in thin films.

began to dominate the measured Q.

5.7 *Support Loss in μHSRs*

The same methods applied previously to determine Q_{Support} in SiBARs can be used for the μHSRs. As an example, consider a 1250 μm diameter, 700 nm thick polysilicon μHSR with an oxide stem (defined by the release process). For this design, Q_{Support} was at least 2 million over varying support dimensions, as plotted in Figure 86. From this figure, the dependency of Q_{Support} appears to be inversely proportional to the square of the support radius. In addition, Q_{Support} is improved proportional to the square of the support length. Table 16 gives the results of holding the support dimensions in the worst case (50 μm radius, 2 μm long). From this table, the trend is for the support to greatly increase with increasing m, suggesting that the m^{th} mode interacts with the support much less than the $(m-1)^{\text{th}}$ mode below it.

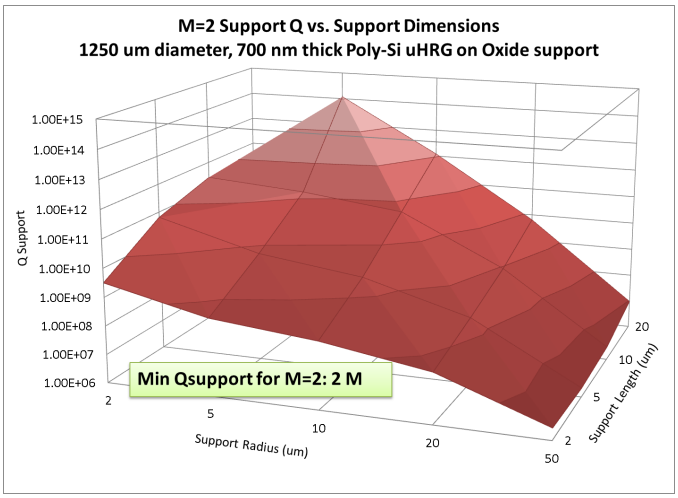

Figure 86: Support loss vs. support radius and height for a 1250 μm diameter, 700 nm thick polysilicon μHSR support on an oxide stem.

Table 16: Q_{Support} vs. Circumferential Mode Index

Mode m	Q_{Support}	$m/(m-1)$
2	2.6 million	-
3	5666 million	2196
4	8,551,378 million	1509

Table 17: Comparison of PML method with acoustic S-parameter method for calculating the Q_{Support} of the polysilicon μHSR of Figure 86.

Support Length (μm)	Support Radius (μm)	PML Length (μm)	Q_{Support} PML Method	Q_{Support} S-parameter Method
2	50	100	1,046,243	1,946,425
2	50	150	146,186	1,947,757
2	50	200	317,632	1,947,589
2	50	250	185,238	1,948,047

Following an approach similar to [85], the Young's modulus can be modulated with a 4$^{\text{th}}$ harmonic around the circumferential direction of the shell (Figure 87). In this extreme example, the 4$^{\text{th}}$ harmonic amplitude was set to 200% of the nominal Young's modulus. This results in a change of Q_{Support} from 55.9 million for each of the degenerate pairs of modes to 32.6 million and 12 million, respectively. These results suggest that structural imperfections can greatly affect both the frequency split and the Qs of the device.

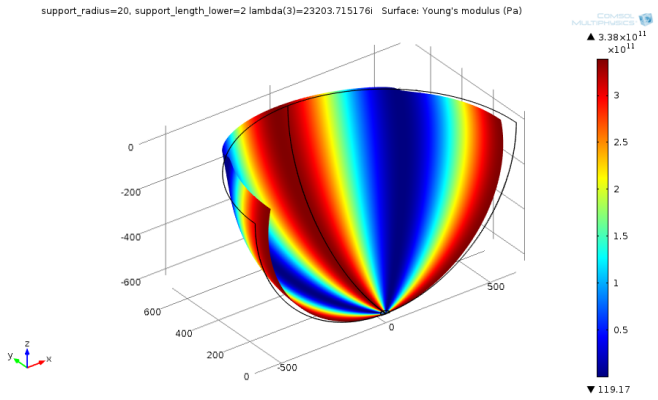

Figure 87: Modulated Young's modulus around the circumferential direction of the shell. The resulting frequency and Q split can be found from the acoustic S-parameter support loss method.

5.8 Overall Q for μHSRs

To choose the final material for the μHSR, a number of factors need to be considered. Surface TED, anchor loss, and air dissipation are the primary loss mechanisms uncovered so far for μHSRs. Table 18 summarizes the results of applying the Q analysis platform to

polysilicon and oxide μHSRs. Surface losses are seen to be the most concerning dissipation for the current design of the devices.

Table 18: Comparison of Q components for a 1250 μm diameter polysilicon and oxide μHSRs with 700 nm and 1 μm shell thicknesses, respectively, to target a frequency of 3.2 kHz.

Dissipation Mechanism	Polysilicon Q	Oxide Q
Q_{PhPh}	Very high (low frequency)	Very high (low frequency)
Q_{PhEl}	High, doping-dependent	High, in coating
Q_{BulkTED}	13.4 million	163.4 million
Q_{Support} $(m = 2)$	2.6-207 million (depends mostly on support radius)	> 1.75 million
$Q_{\text{Surface TED}}$	> 1000 (lower bound)	> 10,000 (lower bound)
Q_{Coating}	No coating needed	Contributes to TED; quality is a concern.
Q_{Surface}	Polysilicon shows rough surfaces	Sensitive to water absorption
$Q_{\text{Polycrystalline TED}}$	8.99E9	No polycrystallites
$Q_{\text{PolycrystalScattering}}$	1.73E20	No polycrystallites
Q_{Air}	> 1 million below 100 μTorr	> 1 million below 100 μTorr

5.9 Discussion of Dissipation in μHSRs

In (48), the resonance frequency of the μHSR was found to be proportional to h/R^2, from which the effective stiffness can be determined to be proportional to h^3/R^2. In fact, multiplying (79) by h^2/h^2, one may see that $Q_{\text{TED}}^{\text{asp.}}$ is inversely proportional to the stiffness and the ratios of asperity diameter and height to the shell's thickness, respectively. Comparing with macroscale HRGs which operate in the adiabatic regime of TED [52, 67], the effective stiffness of a μHSR must be orders of magnitude lower to maintain approximately the same frequency. Meanwhile, the surface to volume ratio of a μHSR scales as $3/h$, significantly increasing the influence of dissipation forces arising at the surfaces of the shell. Indeed, despite achieving $Q > 10$ million, macroscale HRGs are still believed to be limited by their surface loss due to metallization coating [67]. It is also interesting to note that one would be intuitively tempted to assume that $d \propto R$ in (71). In that case, instead of R/h^2 geometric

dependency, the Q_{TED} would simply depend on $1/h$. However, we have shown that this is not the case due to the oscillations of the shell's neutral surface in the φ direction selected by the dispersion of acoustic waves according to the shell's thickness.

The presented model for surface TED relies on several experimentally-derived quantities for accuracy, for which only best estimates are available at the current time. Nevertheless, there is strong semi-quantitative agreement between the model predictions and the measured quality factors of fabricated prototype μHSRs. Although the developed model employs conically-shaped asperities, the results are expected to be quite similar for other shapes since the volumetric strain concentrates at the location of mechanical discontinuity, which is at the asperity's base. Also, with slight modifications, the model can account for radial deviations of the shells since these can be modeled as two asperities located at the same position on the inner and outer surfaces with positive and negative heights. A further modification of the model could account for the surface roughness associated with the grains of polycrystalline materials. The bulk TED model could also be extended to predict the effect of TED due to a thin-film coating on the shell's surface. Therefore, the final Qs of μHSRs can be expected to be bounded by the surface TED on the low end and the bulk TED on the high end (in the absence of other dissipation effects). It is believed that the presented models will prove extremely useful in optimizing the fabrication processes to produce the highest performance μHSRs, especially as their shell thicknesses are reduced to meet size and frequency requirements.

5.10 Conclusions on Dissipation in μHSRs

Bulk TED was investigated in μHSRs analytically and numerically. Linearized shell theory in Rayleigh's inextensional approximation was shown to be insufficient in predicting TED for the quasi-inextensional modes of the μHSRs. Instead, by relaxing the inextensional assumption, a closed-form expression for the thermal path could be derived. The thermal path was found to be dictated by oscillatory deviations of the neutral surface away from

the shell's mid-surface. Using these results, the geometrical scaling law of bulk TED was found to be proportional to R/h^2. A surface model was developed and presented to explain thermoelastic dissipation arising from surface asperities and the resulting volumetric strain concentrations. The geometrical scaling law of surface TED is determined as $R^2/(h \cdot h_a \cdot d_a)$, which reflects two effects: the lowering of the resonance frequency toward the zero-dissipation isothermal limit as well as the effect of increased surface losses when h_a or d_a are increased relative to h. Finite element simulations verify predictions of the analytical bulk and surface TED models. The surface TED model was found to plausibly explain the measured Q in an oxide μHSR with residual asperities, while the bulk TED model limits the ultimately achievable Q. These models are expected to provide insight into the requirements of high-performance μHSRs. Further, slight extensions to these models can be applied to other situations, such as thin NEMS cantilevers, the contributions of thin-film coatings to TED, or exploring the effects of DRIE scalloping to high frequency bulk acoustic wave resonators. The support loss and other dissipation mechanisms were also studied and it was found that the surface losses are likely the dominant loss in current designs. Mitigation of the surface loss requires bringing the surface polish to less than 1 nm roughness. Structural anisotropy was shown to have an impact on Q_{Support}.

CHAPTER VI

CONCLUSIONS AND FUTURE DIRECTIONS

This dissertation was the result of the need to quantify the impact of energy dissipation on MEMS resonators and generate *a priori* estimates of Q, a task which at the beginning of this work was not possible except for specialized circumstances. Indeed, the framework developed here is not without its own shortcomings and further work is needed to account for all possible sources of dissipation. This work is only the launching point into a river of understanding that will rapidly grow deep as the unknown becomes known and the missing pieces of knowledge are filled in to complete the picture of where the energy which was dissipated ends up and how it got there. Toward this end, first, the contributions of this work are outlayed, and then suggestions for future directions are made.

6.1 Contributions

This work has contributed to a number of areas of importance for developing high-performance MEMS resonators. In no particular order, the highlights of this work are:

- Investigation into the energy dissipation mechanisms present in MEMS resonators.
- Application of the above knowledge to quantifying the impact of loss mechanisms on resonator figures of merit, including quality factor and insertion loss.
- Development of a general fully-coupled fully-anisotropic thermoelastic dissipation (TED) model based on the finite element method.
- Development of a novel approach for calculating support loss based on acoustic S-parameters, which is independent of adjustable parameters and will augment and complement the typical PML approach.

- Development of linear acoustic bandgap (LAB) structures for support loss and spurious mode suppression in BAW MEMS resonators.
- Demonstration of scalability of the bandgap of LAB structures across a wide range of frequency from high tens of MHz to nearly 2 GHz.
- Demonstration of performance enhancement of Aluminum Nitride on Silicon (AlN-on-Si) TPoS resonators equipped with LAB supports.
- Enablement of additional tuning ports by use of LAB supports without harming the Q of the device.
- Design of 3D hemispherical structures, which promise low internal dissipation and low support loss, is detailed.
- Development of detailed TED models for 3D μHSRs accounting for TED originating both in the bulk of the device and at its surfaces due to inhomogeneity of stresses resulting from the roughness of the surface.
- Extraction of closed-form scaling laws for the above for easier prediction of TED without resorting to full FE models.
- Investigation into the anchor loss of 3D μHSRs, demonstrating that structural imperfections can result in split of the quality factor in addition to the frequencies.

6.2 Future Directions

The number of directions from which this work may progress are quite numerous. In addition to the obvious future work of refining and improving the models and applying them to other MEMS resonators, this work opens an opportunity to use MEMS resonators to study phonon-phonon and phonon-electron interactions under a variety of conditions by monitoring the Q; in other words, Q is a window into the microscale interactions of fundamental physical phenomena. It it anticipated that pursuing this path can lead to many exciting

and unexpected results. Some areas of pursuit more rooted in engineering are optimizing and designing the LAB structures to suit a particular desired application; for example, by modifying the geometrical parameters or even changing the shape of the entire unit cell. Still to be demonstrated is changing the width of the bandgap without changing its center frequency, although initial results contained herein alluded to one possibility to achieve this. Further, the LAB-enhanced resonators with tuning ports can be optimized to achieve greater tuning if that would be so desired to compensate for drifts or temperature. Finally, a pure capacitive SiBAR with LABs is still experimentally lacking; it is expected that these should show much greater relative Q improvements, bringing the Q to the Akhieser limit.

On the 3D μHSR side, once fabrication has progressed such that devices are repeatable and reliable in operation, there are many opportunities to collect data about these thin-film structures that do not exist in their planar counterparts. For example, the shear modulus is expected to control the frequency of the device, and hence the TCf is a measure of the TCG, where G is the shear modulus. This result was close to positive 60 ppm/°C, which is less than the positive 80 ppm/°C found for the Young's modulus of oxide through other thin-film measurement techniques. Hence, 3D μHSRs can serve as vehicles for characterization of shear characteristics of thin-films and coatings, especially since thermally-grown oxide is one of the most controlled materials available. In addition, the state of anti-biaxial principal strain and its effect on surface TED is very illuminating to the dissipation encountered in these devices; this strain state should be considered in its effect on other surface dissipation mechanisms as well as internal defects in the shell material.

APPENDIX A

IMPORTANT MATERIAL PROPERTIES AND VALUES

A.1 Silicon (Si)

Silicon is perhaps the most important material for MEMS. Borrowing from the success in Silicon CMOS technology, many processes have been developed for working with silicon and it is considered to be very mature. Silicon is an anisotropic crystalline material with different wave propagation speeds along different crystal axes. It exhibits cubic symmetry, which reduces the number of independent elastic constants to three.

Table A.1: Intrinsic Single-Crystal Silicon Material Properties. Data from [24] obtained at 25°C with a pure Si sample with dislocation density < 500/cm^2.

Property	Symbol	Value	Unit	Reference
Acoustic Velocity [100] prop. [100] pol.	$v_{a[100][100]}$	8432.8+/-0.01%	m/s	[24]
Acoustic Velocity [100] prop. [011] pol.	$v_{a[100][011]}$	5842.7+/-0.01%	m/s	[24]
Acoustic Velocity [011] prop. [011] pol.	$v_{a[011][011]}$	9134.2+/-0.01%	m/s	[24]
Acoustic Velocity [011] prop. [100] pol.	$v_{a[011][100]}$	5842.9+/-0.01%	m/s	[24]
Acoustic Velocity [011] prop. [01$\bar{1}$] pol.	$v_{a[011][01\bar{1}]}$	4672.8+/-0.01%	m/s	[24]
Stiffness Coefficient 11	c_{11}	165.64+/-0.02%	GPa	[24]
Temperature Coefficient of c_{11}	TC(c_{11})	-94	ppm/K	[Hull 1999]
Stiffness Coefficient 12	c_{12}	63.94+/-0.02%	GPa	[24]
Temperature Coefficient of c_{12}	TC(c_{12})	-98	ppm/K	[Hull 1999]
Stiffness Coefficient 44	c_{44}	79.51+/-0.02%	GPa	[24]
Temperature Coefficient of c_{44}	TC(c_{44})	-83	ppm/K	[Hull 1999]
Mass Density	ρ	2329.0+/-0.2	kg/m^3	[24]
Coefficient of Thermal Expansion (CTE)	α	2.616	ppm/K	[Hull 1999]
Electrical Resistivity	ρ_e	150	$\Omega \cdot$ cm	[24]

Table A.2: Doped Single-Crystal Silicon Material Properties. Data from [24] obtained at 25°C with a Phosphorous-doped n-type Si sample with N_D=(1.98+/-0.06)E19 cm^{-3} donor concentration measured by the Hall effect.

Property	Symbol	Value	Unit	Reference
Acoustic Velocity [100] prop. [100] pol.	$v_{a[100][100]}$	8432.8+/-0.01%	m/s	[24]
Acoustic Velocity [100] prop. [011] pol.	$v_{a[100][011]}$	5830.6+/-0.01%	m/s	[24]
Acoustic Velocity [011] prop. [011] pol.	$v_{a[011][011]}$	9115.0+/-0.01%	m/s	[24]
Acoustic Velocity [011] prop. [100] pol.	$v_{a[011][100]}$	5829.7+/-0.01%	m/s	[24]
Acoustic Velocity [011] prop. [01$\bar{1}$] pol.	$v_{a[011][01\bar{1}]}$	4613.5+/-0.01%	m/s	[24]
Stiffness Coefficient 11	c_{11}	163.94+/-0.02%	GPa	[24]
Stiffness Coefficient 12	c_{12}	64.77+/-0.02%	GPa	[24]
Stiffness Coefficient 44	c_{44}	79.19+/-0.02%	GPa	[24]
Mass Density	ρ	2329.7+/-0.2	kg/m^3	[24]
Electrical Resistivity	ρ_e	(3.26+/-0.05)E-3	$\Omega \cdot cm$	[24]

A.2 Polysilicon

Table A.3: Poly-Crystalline Silicon Material Properties.

Property	Symbol	Value	Unit	Reference
Young's Modulus	E	169	GPa	COMSOL
Poisson's Ratio	ν	0.22	1	COMSOL
Mass Density	ρ	2320	kg/m^3	COMSOL
Acoustic Impedance (long.)	Z_{polyl}	21.16	$N \cdot s/m^3$	From above
Acoustic Impedance (trans.)	Z_{polyt}	12.87	$N \cdot s/m^3$	From above

A.3 Silicon Dioxide (SiO_2)

Silicon dioxide in its amorphous forms is typically considered to be an isotropic acoustic material. Electrically, it is an insulator. It can be grown by the thermal oxidation process, which may be done in dry or wet atmospheric conditions. Wet oxidation is faster, but dry

oxidation produces higher quality films which are free of water content.

Table A.4: Silicon Dioxide Material Properties

Property	Symbol	Value	Unit	Reference
Young's Modulus	E	70	GPa	
Poisson's Ratio	ν	0.17	1	
Lamé's First Parameter	λ	15.41	GPa	
Lamé's Second Parameter (Shear Mod.)	μ	29.91	GPa	
Mass Density	ρ	2200	kg/m^3	
Thermal Conductivity	κ	1.4	W/m^3K	
Coefficient of Thermal Expansion (CTE)	α	0.5	ppm/K	
Specific Heat Capacity	C_P	730	$J/kg \cdot K$	

REFERENCES

[1] *NIST Digital Library of Mathematical Functions*.

[2] "Vibration displacement on substrate due to time-harmonic stress sources from a micromechanical resonator," *J. Sound Vib.*

[3] Abdolvand, R. and Ayazi, F., "Enhanced power handling and quality factor in thin-film piezoelectric-on-substrate resonators," in *Ultrasonics Symposium, 2007. IEEE*, pp. 608–611, 2007.

[4] Abdolvand, R., Johari, H., Ho, G., Erbil, A., and Ayazi, F., "Quality factor in trench-refilled polysilicon beam resonators," *J. Microelectromech. Syst.*, vol. 15, no. 3, pp. 471–478, 2006.

[5] Abdolvand, R., Lavasani, H., Ho, G., and Ayazi, F., "Thin-film piezoelectric-on-silicon resonators for high-frequency reference oscillator applications," *IEEE Transactions on Ultrasonics, Ferroelectrics and Frequency Control*, vol. 55, no. 12, pp. 2596–2606, 2008.

[6] Akhieser, A., "On the absorption of sound in solids," *J. Phys. (Moscow)*, vol. 1, no. 4, pp. 277–287, 1939.

[7] Auld, B. A., "Application of microwave concepts to the theory of acoustic fields and waves in solids," *IEEE Trans. Micro. Theory Tech.*, vol. 17, pp. 800– 811, Nov. 1969.

[8] Ayazi, F. and Najafi, K., "High aspect-ratio combined poly and single-crystal silicon (HARPSS) MEMS technology," *Journal of Microelectromechanical Systems*, vol. 9, no. 3, pp. 288–294, 2000.

[9] Ayazi, F., Sorenson, L., and Tabrizian, R., "Energy dissipation in micromechanical resonators," in *SPIE Micro- and Nanotechnology Sensors, Systems, and Applications III*, vol. 8031, (Orlando, Florida, USA), pp. 803119–13, May 2011.

[10] Bao, M. and Yang, H., "Squeeze film air damping in MEMS," *Sensors and Actuators A: Physical*, vol. 136, pp. 3–27, May 2007.

[11] Bindel, D. S. and Govindjee, S., "Elastic PMLs for resonator anchor loss simulation," *Int. J. Num. Meth. Eng.*, vol. 64, pp. 789–818, Oct. 2005.

[12] Braginsky, V. B., *Systems with Small Dissipation*. The University of Chicago Press, 1985.

[13] Candler, R., Li, H., Lutz, M., Park, W.-T., Partridge, A., Yama, G., and Kenny, T., "Investigation of energy loss mechanisms in micromechanical resonators," in *TRANSDUCERS 2003, 12th International Conference on Solid-State Sensors, Actuators and Microsystems*, vol. 1, pp. 332–335 vol.1, 2003.

[14] Chan, M., Xie, J., Fonda, P., Najar, H., Yamazaki, K., Lin, L., and Horsley, D., "Micromachined polycrystalline diamond hemispherical shell resonators," in *Solid-State Sensors, Actuators, and Microsystems Workshop 2012*, (Hilton Head Island, South Carolina), pp. 355–358, Transducer Research Foundation, June 2012.

[15] Chew, W. and Liu, Q., "Perfectly matched layers for elastodynamics: a new absorbing boundary condition," *J. Comp. Acoust.*, vol. 51, p. 61801, 1996.

[16] Cho, J., Yan, J., Gregory, J., Eberhart, H., Peterson, R., and Najafi, K., "High-Q fused silica birdbath and hemispherical 3-D resonators made by blow torch molding," in *2013 IEEE 26th International Conference on Micro Electro Mechanical Systems (MEMS)*, pp. 177–180, Jan. 2013.

[17] Choi, S. Y., Na, Y. H., and Kim, J. H., "Thermoelastic damping of inextensional hemispherical shell," in *Proc. World Academy of Science, Engineering and Technology*, vol. 56, p. 198–203, 2009.

[18] Cowley, R. A., "Anharmonic crystals," *Rep. Prog. Phys.*, vol. 31, pp. 123–166, Jan. 1968.

[19] de Klerk, J., Bolef, D., and Klemens, P., ""Bottleneck" in the attenuation of hypersonic waves in quartz at low temperatures," *Phys. Rev. Lett.*, vol. 10, pp. 127–128, Feb. 1963.

[20] Doremus, R. H., "Diffusion of water in silica glass," *J. Mater. Res.*, vol. 10, no. 9, pp. 2379–2389, 1995.

[21] Fan, S.-C., Lui, G.-Y., and Wang, Z.-J., "On flexural vibration of hemispherical shell," *Applied Mathematics and Mechanics*, vol. 12, no. 10, pp. 1023–1030, 1991.

[22] Flügge, W., *Stresses in shells*. Berlin: Springer-Verlag, 2nd ed. ed., 1973.

[23] Gretarsson, A. M. and Harry, G. M., "Dissipation of mechanical energy in fused silica fibers," *Rev. Sci. Instrum.*, vol. 70, pp. 4081–4087, Oct. 1999.

[24] Hall, J. J., "Electronic effects in the elastic constants of n-type silicon," *Phys. Rev.*, vol. 161, no. 3, p. 756, 1967.

[25] Hao, Z. and Ayazi, F., "Support loss in micromechanical disk resonators," in *Micro Electro Mechanical Systems, 2005. MEMS 2005. 18th IEEE International Conference on*, pp. 137–141, 2005.

[26] Hao, Z. and Ayazi, F., "Thermoelastic damping in flexural-mode ring gyroscopes," *ASME Conf. Proc.*, vol. 2005, pp. 335–343, Jan. 2005.

[27] Hao, Z. and Ayazi, F., "Support loss in the radial bulk-mode vibrations of center-supported micromechanical disk resonators," *Sensors and Actuators A*, vol. 134, pp. 582–593, Mar. 2007.

[28] Hao, Z., Erbil, A., and Ayazi, F., "An analytical model for support loss in micromachined beam resonators with in-plane flexural vibrations," *Sensors and Actuators A*, vol. 109, pp. 156–164, Dec. 2003.

[29] Hao, Z. and Liao, B., "An analytical study on interfacial dissipation in piezoelectric rectangular block resonators with in-plane longitudinal-mode vibrations," *Sensors and Actuators A*, vol. 163, pp. 401–409, Sept. 2010.

[30] Harrington, B., Shahmohammadi, M., and Abdolvand, R., "Toward ultimate performance in GHZ MEMS resonators: Low impedance and high Q," in *Micro Electro Mechanical Systems (MEMS), 2010 IEEE 23rd International Conference on*, p. 707–710, 2010.

[31] Ho, G., Abdolvand, R., and Ayazi, F., "High-order composite bulk acoustic resonators," in *Micro Electro Mechanical Systems, 2007. MEMS. IEEE 20th International Conference on*, pp. 791–794, 2007.

[32] Ho, G., Abdolvand, R., Sivapurapu, A., Humad, S., and Ayazi, F., "Piezoelectric-on-silicon lateral bulk acoustic wave micromechanical resonators," *Journal of Microelectromechanical Systems*, vol. 17, no. 2, pp. 512–520, 2008.

[33] Hsiao, F.-L., Khelif, A., Moubchir, H., Choujaa, A., Chen, C.-C., and Laude, V., "Complete band gaps and deaf bands of triangular and honeycomb water-steel phononic crystals," *J. Appl. Phys.*, vol. 101, pp. 044903–5, Feb. 2007.

[34] Hsu, F.-C., Lee, C.-I., Hsu, J.-C., Huang, T.-C., Wang, C.-H., and Chang, P., "Acoustic band gaps in phononic crystal strip waveguides," *App. Phys. Lett*, vol. 96, no. 5, p. 051902, 2010.

[35] Humad, S., Abdolvand, R., Ho, G., Piazza, G., and Ayazi, F., "High frequency micromechanical piezo-on-silicon block resonators," in *Electron Devices Meeting, 2003. IEDM '03 Technical Digest. IEEE International*, pp. 39.3.1–39.3.4, 2003.

[36] Hutson, A., McFee, J., and White, D., "Ultrasonic amplification in CdS," *Phys. Rev. Lett.*, vol. 7, pp. 237–239, Sept. 1961.

[37] Kittel, C., "Ultrasonics research and the properties of matter," *Rep. Prog. Phys.*, vol. 11, pp. 205–247, Jan. 1947.

[38] Kuo, N. K., Zuo, C., and Piazza, G., "Demonstration of inverse acoustic band gap structures in AlN and integration with piezoelectric contour mode wideband transducers," *App. Phys. Lett.*, vol. 95, p. 093501, 2009.

[39] Lakin, K., Kline, G., and McCarron, K., "Development of miniature filters for wireless applications," *IEEE Trans. Micro. Theory and Tech.*, vol. 43, no. 12, p. 2933–2939, 1995.

[40] Lamb, H., "On waves in an elastic plate," *Proc. R. Soc. London Ser. A*, vol. 93, no. 648, p. 114–128, 1917.

[41] Lamb, J. and Richter, J., "New type of cavity resonator for piezoelectric surface excitation of acoustic waves at microwave frequencies," *Electronics Lett.*, vol. 2, pp. 73–74, Feb. 1966.

[42] Landau, L. D., *Theory of Elasticity*. Oxford: Pergamon Press, 3rd english ed. ed., 1986. Revised and enlarged by E.M. Lifshitz, A.M. Kosevich, and L.P. Pitaevskii.

[43] Landau, L. D. and Rumer, G., "On the absorption of sound in solids," *Phys. Z. Sowjetunion*, vol. 11, pp. 18–25, 1937.

[44] Lavasani, H. M., Pan, W., Harrington, B., Abdolvand, R., and Ayazi, F., "A 76 dbΩ 1.7 GHz 0.18 μm CMOS tunable TIA using broadband current pre-amplifier for high frequency lateral MEMS oscillators," vol. 46, pp. 224–235, Jan. 2011.

[45] Lee, B. J. and To, A. C., "Enhanced absorption in one-dimensional phononic crystals with interfacial acoustic waves," *Appl. Phys. Lett.*, vol. 95, pp. 031911–3, July 2009.

[46] Lerman, M. and Elata, D., "On the quality-factor of micro-resonators," *Proc. Eurosensors XXIV*, vol. 5, pp. 95–98, 2010.

[47] Lifshitz, R. and Roukes, M. L., "Thermoelastic damping in micro- and nanomechanical systems," *Phys. Rev. B*, vol. 61, p. 5600, Feb. 2000.

[48] Lord, H. and Shulman, Y., "A generalized dynamical theory of thermoelasticity," *Journal of the Mechanics and Physics of Solids*, vol. 15, pp. 299–309, Sept. 1967.

[49] Love, A. E. H., *A treatise on the mathematical theory of elasticity*. New York: Dover, 4th ed. ed., 1944.

[50] McSkimin, H. J., "Measurement of elastic constants at low temperatures by means of ultrasonic waves–data for silicon and germanium single crystals, and for fused silica," *J. Appl. Phys.*, vol. 24, no. 8, pp. 988–997, 1953.

[51] McSkimin, H. J. and Andreatch, J., "Elastic moduli of silicon vs hydrostatic pressure at 25.0°C and -195.8°C," *J. Appl. Phys.*, vol. 35, pp. 2161–2165, July 1964.

[52] Meyer, A. and Rozelle, D., "Milli-HRG inertial navigation system," in *2012 IEEE/ION Position Location and Navigation Symposium (PLANS)*, pp. 24–29, Apr. 2012.

[53] Mohammadi, S., Eftekhar, A., Khelif, A., Moubchir, H., Westafer, R., Hunt, W., and Adibi, A., "Complete phononic bandgaps and bandgap maps in two-dimensional silicon phononic crystal plates," *Electron. Lett.*, vol. 43, no. 16, p. 898, 2007.

[54] Mohammadi, S., Eftekhar, A. A., Khelif, A., and Adibi, A., "Support loss suppression in micromechanical resonators by the use of phononic band gap structures," in *Proc. SPIE: Photonic and Phononic Crystal Materials and Devices X*, vol. 7609, (San Francisco, California, USA), pp. 76090W–1, 2010.

[55] Mohammadi, S., Eftekhar, A. A., Khelif, A., Hunt, W. D., and Adibi, A., "Evidence of large high frequency complete phononic band gaps in silicon phononic crystal plates," *App. Phys. Lett.*, vol. 92, pp. 221905–221905–3, June 2008.

[56] Monajemi, P., Joseph, P. J., Kohl, P. A., and Ayazi, F., "Wafer-level MEMS packaging via thermally released metal-organic membranes," *J. Micromech. Microeng.*, vol. 16, pp. 742–750, Apr. 2006.

[57] Niklasson, G. and Sjolander, A., "Theory of thermal motions in anharmonic crystals," *Annals of Physics*, vol. 49, pp. 249–296, Sept. 1968.

[58] Nowick, A. S. and Berry, B. S., *Anelastic relaxation in crystalline solids*. Academic Press, 1972.

[59] Olsson III, R. H., El-Kady, I. F., Su, M. F., Tuck, M. R., and Fleming, J. G., "Microfabricated VHF acoustic crystals and waveguides," *Sensors and Actuators A*, vol. 145–146, pp. 87–93, July 2008.

[60] Pan, W., Abdolvand, R., and Ayazi, F., "A low-loss 1.8GHz monolithic thin-film piezoelectric-on-substrate filter," in *Micro Electro Mechanical Systems, 2008. MEMS 2008. IEEE 21st International Conference on*, pp. 176–179, 2008.

[61] Picard, A., Barat, P., Borys, M., Firlus, M., and Mizushima, S., "State-of-the-art mass determination of ^{28}Si spheres for the Avogadro project," *Metrologia*, vol. 48, pp. S112–S119, Apr. 2011.

[62] Pomerantz, M., "Ultrasonic loss and gain mechanisms in semiconductors," *Proceedings of the IEEE*, vol. 53, no. 10, pp. 1438–1451, 1965.

[63] Pourkamali, S. and Ayazi, F., "High frequency capacitive micromechanical resonators with reduced motional resistance using the HARPSS technology," in *Silicon Monolithic Integrated Circuits in RF Systems, 2004. Digest of Papers. 2004 Topical Meeting on*, pp. 147–150, 2004.

[64] Pourkamali, S., Ho, G., and Ayazi, F., "Low-impedance VHF and UHF capacitive silicon bulk acoustic-wave Resonators—Part II: measurement and characterization," *IEEE Transactions on Electron Devices*, vol. 54, no. 8, pp. 2024–2030, 2007.

[65] Prikhodko, I. P., Zotov, S. A., Trusov, A. A., and Shkel, A. M., "Microscale glass-blown three-dimensional spherical shell resonators," *J. Microelectromech. Syst.*, vol. 20, pp. 691–701, June 2011.

[66] Rayleigh, "On the infinitesimal bending of surfaces of revolution," *Proc. London Math. Soc.*, vol. s1-13, pp. 4–16, Nov. 1881.

[67] Rozelle, D. M., "The hemispherical resonator gyro: from wineglass to the planets," in *Proc. 19th AAS/AIAA Space Flight Mechanics Meeting*, AAS 09-176, p. 1157–1178, Feb. 2009.

[68] Ruby, R., Bradley, P., Oshmyansky, Y., Chien, A., and Larson III, J., "Thin film bulk wave acoustic resonators (FBAR) for wireless applications," in *Ultrasonics Symposium, 2001 IEEE*, vol. 1, p. 813–821, 2001.

[69] Samarao, A. K. and Ayazi, F., "Quality factor sensitivity to crystallographic axis misalignment in silicon micromechanical resonators," in *2010 Solid State Sensor, Actuator and Microsystems Workshop (Hilton Head 2010)*, (Hilton Head Island, South Carolina), pp. 479–482, TRF, June 2010.

[70] Samarao, A. and Ayazi, F., "Temperature compensation of silicon micromechanical resonators via degenerate doping," in *Electron Devices Meeting (IEDM), 2009 IEEE International*, pp. 1–4, 2009.

[71] Samarao, A. and Ayazi, F., "Self-polarized capacitive silicon micromechanical resonators via charge trapping," in *Electron Devices Meeting (IEDM), 2010 IEEE International*, pp. 7.4.1–7.4.4, 2010.

[72] Samarao, A., Casinovi, G., and Ayazi, F., "Passive TCF compensation in high q silicon micromechanical resonators," in *Micro Electro Mechanical Systems (MEMS), 2010 IEEE 23rd International Conference on*, pp. 116–119, 2010.

[73] Sarac, B., Kumar, G., Hodges, T., Ding, S., Desai, A., and Schroers, J., "Three-dimensional shell fabrication using blow molding of bulk metallic glass," *J. Microelectromech. Syst.*, vol. 20, pp. 28–36, Feb. 2011.

[74] Senkal, D., Ahamed, M., Trusov, A., and Shkel, A., "Adaptable test-bed for characterization of micro-wineglass resonators," in *2013 IEEE 26th International Conference on Micro Electro Mechanical Systems (MEMS)*, pp. 469–472, Jan. 2013.

[75] Senkal, D., Raum, C. R., Trusov, A. A., and Shkel, A. M., "Titania silicate/fused quartz glassblowing for 3-D fabrication of low internal loss wineglass microstructures," in *Solid-State Sensors, Actuators, and Microsystems Workshop 2012*, (Hilton Head Island, South Carolina), pp. 267–270, Transducer Research Foundation, June 2012.

[76] Shahmohammadi, M., Harrington, B., and Abdolvand, R., "Concurrent enhancement of q and power handling in multi-tether high-order extensional resonators," in *Microwave Symposium Digest (MTT), 2010 IEEE MTT-S International*, pp. 1452–1455, 2010.

[77] Shao, P., Sorenson, L. D., Gao, X., and Ayazi, F., "Wineglass-on-a-chip," in *Solid-State Sensors, Actuators, and Microsystems Workshop 2012*, (Hilton Head Island, South Carolina), pp. 275–278, Transducer Research Foundation, June 2012.

[78] Shiren, N. S., "Effect of anisotropic anharmonicity on acoustic attenuation," *Phys. Lett.*, vol. 20, pp. 10–11, Jan. 1966.

[79] Shkel, A., Howe, R. T., and Horowitz, R., "Modeling and simulation of micromachined gyroscopes in the presence of imperfections," in *Technical Proceedings of the 1999 International Conference on Modeling and Simulation of Microsystems*, pp. 605–608, NSTI, 1999.

[80] Sigmund, O. and Jensen, J. S., "Systematic design of phononic band-gap materials and structures by topology optimization," vol. 361, pp. 1001–1019, May 2003.

[81] Soedel, W., *Vibrations of shells and plates*. New York: Marcel Dekker, 3rd ed. ed., 2004.

[82] Sorenson, L., Fu, J., and Ayazi, F., "Linear acoustic bandgap arrays for spurious mode suppression in piezoelectric MEMS resonators," in *Frequency Control and the European Frequency and Time Forum (FCS), 2011 Joint Conference of the IEEE International*, pp. 1–5, IEEE, May 2011.

[83] Sorenson, L., Fu, J. L., and Ayazi, F., "One-dimensional linear acoustic bandgap structures for performance enhancement of AlN-on-Silicon micromechanical resonators," in *Solid-State Sensors, Actuators and Microsystems Conference (TRANSDUCERS), 2011 16th International*, pp. 918–921, IEEE, June 2011.

[84] Sorenson, L., Gao, X., and Ayazi, F., "3-D micromachined hemispherical shell resonators with integrated capacitive transducers," in *2012 IEEE 25th International Conference on Micro Electro Mechanical Systems (MEMS)*, p. 168–171, Jan. 2012.

[85] Sorenson, L., Shao, P., and Ayazi, F., "Effect of thickness anisotropy on degenerate modes in oxide micro-hemispherical shell resonators," in *2013 IEEE 26th International Conference on Micro Electro Mechanical Systems (MEMS)*, pp. 169–172, Jan. 2013.

[86] Srikar, V. and Senturia, S., "Thermoelastic damping in fine-grained polysilicon flexural beam resonators," *J. Microelectromech. Syst.*, vol. 11, no. 5, pp. 499–504, 2002.

[87] Tabrizian, R., Rais-Zadeh, M., and Ayazi, F., "Effect of phonon interactions on limiting the f.Q product of micromechanical resonators," in *Solid-State Sensors, Actuators and Microsystems Conference, 2009. TRANSDUCERS 2009. International*, pp. 2131–2134, 2009.

[88] Thurston, R. N., McSkimin, H. J., and Andreatch, J., "Third-order elastic coefficients of quartz," *J. Appl. Phys.*, vol. 37, pp. 267–275, Jan. 1966.

[89] Timoshenko, S. and Woinowsky-Krieger, S., *Theory of plates and shells*. New York: McGraw-Hill, 2d ed. ed., 1959.

[90] Tobar, M., "Effects of spurious modes in resonant cavities," *J. Phys. D: Appl. Phys.*, vol. 26, pp. 2022–2027, 1993.

[91] Veijola, T., Kuisma, H., Lahdenperä, J., and Ryhänen, T., "Equivalent-circuit model of the squeezed gas film in a silicon accelerometer," *Sensors and Actuators A: Physical*, vol. 48, pp. 239–248, May 1995.

[92] Wang, J., Butler, J., Feygelson, T., and Nguyen, C., "1.51-GHz nanocrystalline diamond micromechanical disk resonator with material-mismatched isolating support," in *17th IEEE International Conference on Micro Electro Mechanical Systems. Maastricht MEMS 2004 Technical Digest*, (Maastricht, Netherlands), pp. 641–644, Jan. 2004.

[93] Weinberg, M., Candler, R., Chandorkar, S., Varsanik, J., Kenny, T., and Duwel, A., "Energy loss in MEMS resonators and the impact on inertial and RF devices," in *Solid-State Sensors, Actuators and Microsystems Conference, 2009. TRANSDUCERS 2009. International*, pp. 688–695, 2009.

[94] White, R. M., "Surface elastic-wave propagation and amplification," *IEEE Transactions on Electron Devices*, vol. 14, pp. 181–189, Apr. 1967.

[95] Xu, Y. and Hao, Z., "Modeling support loss in SOI-Based micromechanical resonators," *ASME Conf. Proc.*, vol. 2007, pp. 85–89, Jan. 2007.

[96] Xu, Y., Wang, R., Durgam, S. K., Hao, Z., and Vahala, L., "Numerical models and experimental investigation of energy loss mechanisms in SOI-based tuning-fork gyroscopes," vol. 152, pp. 63–74, May 2009.

[97] Zener, C., "Internal friction in solids. I. Theory of internal friction in reeds," *Phys. Rev.*, vol. 52, no. 3, p. 230, 1937.

[98] Zener, C., "Internal friction in solids II. General theory of thermoelastic internal friction," *Phys. Rev.*, vol. 53, p. 90, Jan. 1938.

[99] Zener, C., "Theory of the elasticity of polycrystals with viscous grain boundaries," *Phys. Rev.*, vol. 60, p. 906, Dec. 1941.

[100] Zhu, X.-F., "Investigation of a silicon-based one-dimensional phononic crystal plate via the super-cell plane wave expansion method," *Chin. Phys. B*, vol. 19, no. 4, p. 044301, 2010.

[101] Ziman, J. M., *Electrons and phonons; the theory of transport phenomena in solids*. Oxford: Clarendon Press, 1960.

[102] Zotov, S., Trusov, A., and Shkel, A., "Three-dimensional spherical shell resonator gyroscope fabricated using wafer-scale glassblowing," *J. Microelectromech. Syst.*, vol. 21, no. 3, pp. 509–510, 2012.

VITA

Logan grew up in the Pacific Northwest in Washington State. At 18, he moved to Chicago where he would later receive his B.S. in Electrical Engineering from the Illinois Institute of Technology in December 2004. For 11 months of his junior year, he participated in an exchange program with KTH, the Royal Institute of Technology, in Stockholm, Sweden. Upon graduation, Logan moved to Minneapolis, MN where he worked on large server development as an intern at Unisys. He returned to Chicago in August 2005 to pursue his M.S. in E.E., with a research focus on embedded system design and architecture for digital signal processing. Looking toward the future and realizing the potential of micro- and nanoscale devices, he moved to Atlanta in August 2007 to pursue Ph.D. studies at Georgia Tech, and subsequently joined Dr. Ayazi's IMEMS group in January 2008 to work on MEMS/NEMS devices. During this time, he took on an internship at Integrated Device Technology, Inc. in San Jose, CA. He is the recipient of the Outstanding Oral Paper Award at the 2013 IEEE MEMS conference in Taipei, Taiwan.

In his spare time, Logan enjoys listening to and creating music (amateur cellist and guitarist), learning languages such as Vietnamese, Spanish, Japanese, Swedish, Chinese, and German, working on various things in Linux, traveling, and outdoor activities such as camping, hiking, kayaking, skiing, snowboarding, and mountain biking. He married his wife, Phuong Bui, in May 2008.

Design and Analysis of Microelectromechanical Resonators with Ultra-Low Dissipation

Logan D. Sorenson

120 Pages

Directed by Farrokh Ayazi

This dissertation investigates dissipation in microelectromechanical (MEMS) resonators via detailed analysis and modeling of the energy loss mechanisms and provides a framework toward creating resonant devices with ultra-low dissipation. Fundamental mechanisms underlying acoustic energy loss are explored, the results of which are applied to understanding the losses in resonant MEMS devices. Losses in the materials, which set the ultimate limits of the achievable quality factor of the devices, are examined. Other sources of loss, which are determined by the design of the resonator, are investigated and applied to example resonant MEMS structures. The most critical of these designable loss mechanisms are thermoelastic dissipation (TED) and support (or anchor) loss of acoustic energy through the attachment of the MEMS device to its external environment. The dissipation estimation framework enables prediction of the quality factor of a MEMS resonator, which were accurate within a factor of close to 2 for high-frequency bulk acoustic wave MEMS resonators, and represents a signficant step forward by closing one of the largest outstanding problems in MEMS devices: how to predict the quality factor for a given device.

Dissipation mitigation approaches developed herein address the most critical dominant loss mechanisms identified using the framework outlined above. These approaches include design of 1D phononic crystals (PCs) and novel 3D MEMS structures to trap and isolate vibration energy away from the resonator anchors, optimization of resonator geometry to suppress thermoelastic dissipation, and analysis of required levels of surface polish to reduce surface dissipation. Phononic crystals can be used to manipulate the properties of materials. In the case of the 1D PC linear acoustic bandgap (LAB) structures developed here, this manipulation arises from the formation of frequency stop bands, or bandgaps,

which convert silicon from a material capable of supporting acoustic waves to a material which rejects acoustic propagation at frequencies in the bandgap. The careful design of these LAB structures is demonstrated to be able to enhance the quality factor and insertion loss of MEMS resonators without significant detrimental effects on the overall device performance.